Transport Phenomena of Entangled Polymer Melts: A Multi-Scale Simulation Study

Takeshi Sato

2020

Contents

1 General Introduction

1.1 Introductory Remarks

Polymeric materials are widely used in our daily life, from daily necessities to automobiles and aircraft. Therefore, producing high-performance polymer products is an essential issue in the polymer industry. To obtain desirable physical properties in polymer products, a variety of techniques are employed, such as incorporating low molecular additives or blending different types of polymers. Due to the high frequency of use and usefulness of polymers, the twentieth century is referred to as the "*Polymer Age*" by Rubinstein and Colby [1].

The manufacturing process of polymer products typically consists of the following procedures: flow, shaping, cooling and solidification. Therefore, when manufacturing polymer products, it is necessary to address polymeric liquids, which are complex fluids. Thus, predicting and controlling the flow behavior of polymeric liquids is important for the polymer industry. However, the gap between basic polymer science and the polymer industry is still quite large, mainly for the following reasons: First, polymeric liquids themselves are complex fluids, and it is generally difficult to predict their flow properties. Second, many types of polymeric materials, such as polymer blends, are employed, and the interactions between different components have not been fully elucidated.

Addressing the flow properties of polymeric liquids can be regarded as a transport phenomenon problem in chemical engineering [2]. The study of transport phenomena involves the transport of mass, momentum, and energy in the system under consideration. These three phenomena frequently occur simultaneously in industrial problems. An important aspect is the fact that the basic equations that describe the three phenomena are very similar, which means that the three problems can be solved using similar mathematical tools. As shown in Fig. 1.1, the fundamental equations can be derived from conservation laws (in other words, balance equations). For example, from the mass balance equation, the equation of

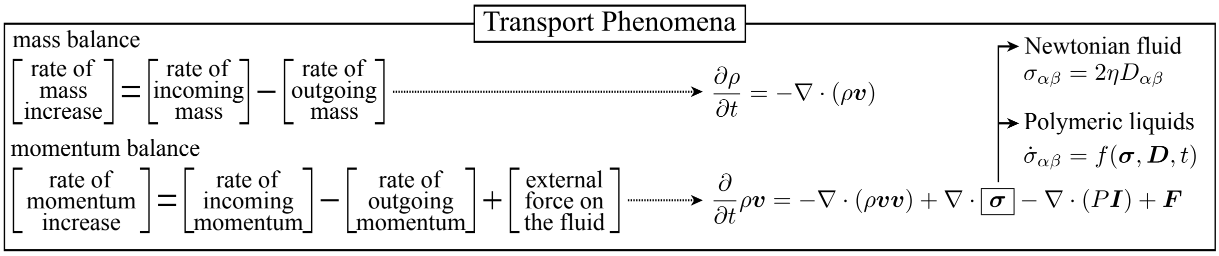

Fig. 1.1: Schematic illustration of background of transport phenomena.

continuity can be obtained as

$$\frac{\partial \rho}{\partial t} = -\nabla \cdot (\rho \boldsymbol{v}), \tag{1.1}$$

where ρ is the density, t is time, and $\boldsymbol{v}$ is the velocity. In particular, for a fluid with a constant density, a so-called incompressible fluid, Eq. (1.1) can be rewritten as

$$\nabla \cdot \boldsymbol{v} = 0. \tag{1.2}$$

Furthermore, from the momentum balance equation, the equation of motion can be obtained as

$$\frac{\partial}{\partial t}\rho \boldsymbol{v} = -\nabla \cdot (\rho \boldsymbol{v}\boldsymbol{v}) + \nabla \cdot \boldsymbol{\sigma} - \nabla \cdot (P\boldsymbol{I}) + \boldsymbol{F}, \tag{1.3}$$

where $\boldsymbol{\sigma}$ is the stress tensor, P is the pressure, and $\boldsymbol{F}$ is an external force. If we combine Eq. (1.1) with Eq. (1.3), then the equation of motion can be rewritten as

$$\rho \left(\frac{\partial \boldsymbol{v}}{\partial t} + \boldsymbol{v} \cdot \nabla \boldsymbol{v} \right) = \nabla \cdot \boldsymbol{\sigma} - \nabla \cdot (P\boldsymbol{I}) + \boldsymbol{F}. \tag{1.4}$$

This equation of motion is used to solve transport problems. The remaining problem is to obtain an expression for the stress tensor $\boldsymbol{\sigma}$. Any equation that relates deformation and stress is called a constitutive equation. In the simplest case, the constitutive equation can be expressed as

$$\boldsymbol{\sigma} = 2\eta \boldsymbol{D}, \tag{1.5}$$

where η is the viscosity, and $\boldsymbol{D}$ is the deformation rate tensor, defined as $\boldsymbol{D} \equiv \left(\nabla \boldsymbol{v} + \nabla \boldsymbol{v}^{\mathrm{T}}\right)/2$. Eq. (1.5) is referred to as Newton's law of viscosity, and a fluid that follows Eq. (1.5) is a Newtonian fluid. Here, Eq. (1.5) can be regarded as a simple constitutive equation. By combining Eqs. (1.2), (1.4), and (1.5) with material constants and appropriate boundary conditions, we can solve any isothermal flow problem for a Newtonian fluid.

When dealing with flow problems of polymeric liquids, which are a type of viscoelastic fluid, viscoelastic constitutive equations should be employed. A viscoelastic constitutive equation is generally written as

$$\dot{\sigma}_{\alpha\beta} = f(\boldsymbol{\sigma}, \boldsymbol{D}, t) \quad \alpha, \beta \in \{x, y, z\}\,, \tag{1.6}$$

where $\dot{\sigma}_{\alpha\beta}$ is the time derivative of the stress tensor. As shown in Eq. (1.6), a viscoelastic constitutive equation may depend on the deformation history. To solve flow problems involving polymeric liquids, we have to know the viscoelastic constitutive relation. Studies on viscoelastic constitutive equations have actively been performed in the field of "rheology", a discipline that relates flow and deformation. In principle, with the help of rheology, we can solve the transport problems of polymeric liquids.

Since the stress tensor of polymeric liquids is tightly related to the microscopic states of the polymer chains, in principle, the viscoelastic constitutive equations of polymeric liquids should be derived from microscopic scale dynamics, with the assistance of statistical theories. However, it is generally very difficult to derive constitutive equations for polymeric liquids, such as Eq. (1.6), because the stress caused by the polymer chains depends on their deformation history [3]. While considerable efforts have been made in developing molecular-based constitutive equations, phenomenological constitutive equations are often employed for most polymer industry simulations. Here, "phenomenological" constitutive equations refer to equations that lack a solid molecular basis. Phenomenological constitutive equations, such as the Kaye-BKZ constitutive equation (for more details, please see Sec. 1.2.5), can give reasonably accurate linear and nonlinear viscoelastic predictions for practical flow problems in the polymer industry. However, as mentioned above, phenomenological constitutive equations do not allow us to obtain molecular insights into the configuration of the polymer chains. These microscopic molecular insights are necessary to design polymer products with specific physical properties.

It is important for transport problems of polymeric liquids to obtain the polymeric stress without losing microscopic molecular insights. From a simulation point of view, a molecular dynamics (MD) simulation is the promising technique to obtain the polymeric stress, as well as microscopic molecular insights. However, MD simulations do not allow us to probe the large length- and time-scale phenomena of polymeric liquids, which are important for polymer processing, mainly due to the large computational cost. Thus, designing polymer products with specific physical properties based on the microscopic states of polymer chains is still one of the great challenges, not only in chemical engineering but also in the field of materials science.

1.2 Entangled Polymer Dynamics

Polymeric liquids in an entangled state are important for the polymer industry because many polymeric liquids are used in the entangled state. In this study, we limit ourselves mainly to entangled polymer dynamics. The "entangled state" in a polymeric liquid is universal, which means that the polymer dynamics in the entangled state does not depend on the polymer species. Here, we explain the entangled state by the molecular weight dependence of the zero shear viscosity. Experimentally, the zero shear viscosity η_0 depends on the molecular weight M as

$$\eta_0 \propto M \ (M < M_\mathrm{c}); \quad \eta_0 \propto M^{3.4} \ (M > M_\mathrm{c}), \tag{1.7}$$

where M_c is the critical molecular weight. The dynamics of polymeric liquids qualitatively changes when M is larger or smaller than M_c, and the region that corresponds to $M > M_\mathrm{c}$ is called the "entangled state" [4]. Moreover, the dependences of other physical quantities

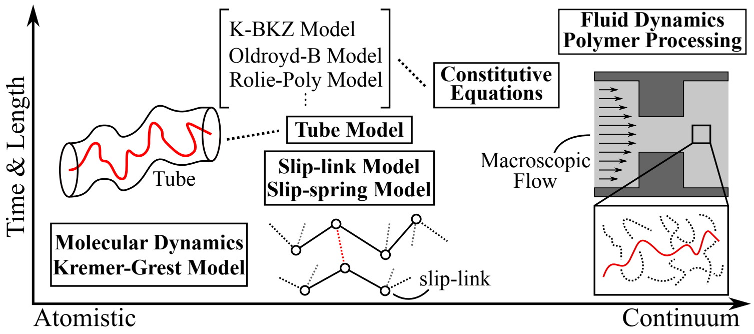

Fig. 1.2: Schematic illustration of simulation methods and theories of entangled polymers under flow from the microscopic level to the macroscopic level.

are experimentally observed to be

$$\langle \tau \rangle \propto M^2 \ (M < M_\mathrm{c}); \quad \langle \tau \rangle \propto M^{3.4} \ (M > M_\mathrm{c}), \tag{1.8}$$

$$D \propto M^{-1} \ (M < M_\mathrm{c}); \quad D \propto M^{-2.3} \ (M > M_\mathrm{c}), \tag{1.9}$$

$$J_\mathrm{e} \propto M \ (M < M'_\mathrm{c}); \quad J_\mathrm{e} \propto M^0 \ (M > M'_\mathrm{c}), \tag{1.10}$$

where $\langle \tau \rangle$ is the average relaxation time, D is the diffusion constant, J_e is the steady-state shear compliance, and M'_c is the critical molecular weight for the steady-state shear compliance.

There are several different theoretical and numerical methods for each characteristic scale because entangled polymer melts have a spatiotemporal hierarchical structure. A schematic representation of the theoretical and numerical methods for each time and length scale is shown in Fig. 1.2. In the following, I briefly review previous studies on entangled polymers, mainly from the theoretical and simulation points of view, from the microscopic level to the macroscopic level.

1.2.1 Molecular Dynamics Simulations

The most microscopic and detailed method shown in Fig. 1.2 is coarse-grained molecular dynamics (CGMD) simulation. Here, the term "coarse-grained" means that several monomers are represented by one bead in the CGMD simulations. In a pioneering study on CGMD simulations of entangled polymer melts, Kremer and Grest developed the Kremer-Grest (KG) model [5]. In the KG model, a polymer chain is expressed by a number of beads connected by springs, and each bead moves according to an equation of motion. To address the effect of entanglements, the repulsive Lennard-Jones (LJ) potential is employed. Using the KG model, static and dynamic properties for unentangled to entangled polymer melts in the equilibrium state were extensively studied [5].

Linear viscoelastic properties, such as the relaxation modulus $G(t)$, were examined by Likhtman and coworkers using the KG model [6]. Likhtman and coworkers enabled the calculation of $G(t)$ from stress-stress autocorrelation functions by using an efficient on-the-fly calculation method called the multiple tau correlator [7]. The nonlinear rheological properties of the KG model have also been studied by many researchers [8–13]. One of the important problems for nonlinear flow predictions using the KG model is how to set an appropriate boundary condition. When considering shear flows, the Leeds-Edwards boundary condition can provide a solution to this problem [14]. By employing the Leeds-Edwards boundary condition, shear rheological properties, including the steady shear viscosity [8], transient shear viscosity [9], and shear banding [10], for mildly entangled polymer melts were studied. For the case of uniaxial elongational flows, the uniform extensional flow (UEF) algorithm was recently developed [15]. The UEF algorithm enables one to investigate the uniaxial elongational properties of entangled polymer melts until a steady state is reached [11–13]. Since investigations of the uniaxial elongational properties of entangled polymer melts using the KG model have only been possible recently, further studies are expected. For now, the nonlinear rheological properties of the KG model have been examined for specific flow types for which appropriate boundary conditions can be set. However, flows in polymer processing are generally combinations of the abovementioned flow types. It is still technically difficult to investigate the rheological properties of general flows using the KG model.

In addition to studies focusing on the rheological properties, there are also various studies that have examined the microscopic structure obtained from KG simulations, such as topological constraints in entangled polymer melts [16–19]. The method that extracts topological constraints from the entangled network formed by KG polymer chains is referred to as primitive path analysis (PPA). Although there are some variations of the PPA method [16–18], the aims of these methods are almost the same. PPA is important not only as a technique for examining the microscopic structure of entangled polymers but also as a foundation of the mesoscale theories mentioned in the next section. Using PPA methods, the statistical properties of entangled polymer melts in the equilibrium state have been extensively examined [16–18]. More recently, statistical properties in the nonequilibrium state were examined using PPA, and further developments are expected [19].

1.2.2 Tube Theory

The most successful mesoscale theory for entangled polymer melts is the tube model, which was first introduced by de Gennes [20]. The basic idea of the tube model is that a polymer chain in an entangled polymer melt can be considered to be confined in a tube-like region formed by other polymer chains. While the lateral motion of the chain confined to the tube is highly suppressed by other chains, the confined chain can move along the tube. This curvilinear diffusion along the tube was called "reptation motion" by de Gennes. After this pioneering work performed by de Gennes, Doi and Edwards developed the famous Doi-Edwards (DE) model based on the reptation picture [21]. In the DE model, a polymer chain is confined to a tube of constant length fixed in space. By analyzing the diffusion along the tube, the longest relaxation time $\tau_{\mathrm{d}}^{(\mathrm{DE})}$, which is called the reptation time, can be evaluated as $\tau_{\mathrm{d}}^{(\mathrm{DE})} \propto M^3$. This prediction is close to the experimentally observed relaxation time shown in Eq. (1.8).

In addition to reptation motion, it is important to consider the following two relaxation mechanisms when predicting the rheological properties of entangled polymer melts in the linear region. One mechanism is the contour length fluctuation (CLF), which is the fluctuation of the polymer chain confined in the tube [22, 23]. By combining the CLF with the DE model, the rheological properties of entangled polymer melts can be better explained. For example, the molecular weight dependence of the zero shear viscosity is correctly predicted ($\eta_0 \propto M^{3.4}$). The other mechanism is the constraint release (CR), which is caused by the motion of other chains forming the tube [24, 25]. Most of the current variations of the tube model include these three relaxation mechanisms (reptation, CLF, and CR).

For linear rheological properties, there are many types of tube models, such as the Milner-McLeish (MM) model [26], the Likhtman-McLeish (LM) model [27], the time-marching algorithm (TMA) [28], the hierarchical model [29], and the branch-on-branch (BoB) model [30]. Although these models have a common theoretical background, these models differ in some assumptions, such as the method of introducing the CLF and CR. Specifically, there are several different methods to introduce the CR. In the LM model, which describes the linear rheology of entangled linear polymer melts, the CR is modeled as a Rouse-like motion of the chain with different mobilities [25, 27]. For entangled polymers that have broad relaxation time distribution, such as entangled star polymer melts, the dynamic tube dilation (DTD) is effective to model the CR [26, 28–30]. In the DTD picture, a tube diameter is dilated with time by the CR. Therefore, the DTD can be considered as a spatiotemporal coarse-graining process of the tube. The difference between these tube models has been examined for entangled linear polymer melts [31], symmetric star polymer melts [32], and branched polymer melts [33].

To predict nonlinear rheological properties, two mechanisms not addressed in the linear region need to be considered. One mechanism is the convective constraint release (CCR) [34], which is important mainly for $\dot{\gamma}, \dot{\epsilon} > \tau_{\mathrm{d}}^{-1}$, where $\dot{\gamma}$ is the shear rate, $\dot{\epsilon}$ is the elongation rate, and τ_{d} is the reptation time. In the CCR picture, entangled polymer chains are transiently stretched under flows, and subsequent retraction of polymer chains induces the CR in the strain rate region $\dot{\gamma}, \dot{\epsilon} > \tau_{\mathrm{d}}^{-1}$. The other mechanism is the chain stretch [35, 36], which becomes significant when $\dot{\gamma}, \dot{\epsilon} > \tau_{\mathrm{R}}^{-1}$, where τ_{R} is the Rouse relaxation time. There are various tube-model-based constitutive models, and these models are explained in the next section.

1.2.3 Tube-model-based Constitutive Models

One of the tube-based molecular theories for nonlinear rheological properties is the Mead-Larson-Doi (MLD) model [37]. The MLD model, which includes the reptation, chain stretch, and the CCR mechanisms, can explain the nonlinear rheological responses of entangled linear polymer melts not only for the steady state, but also for transient phenomena at strain rates $\dot{\gamma} > \tau_{\mathrm{d}}^{-1}$ [37]. The Graham, Likhtman and Milner, McLeish (GLaMM) model was developed by Graham and coworkers [38]. In the GLaMM model, the CCR mechanism is considered local Rouse-like tube motion, and the chain stretch is modeled based on the Rouse motion of a chain confined in the tube. Using the GLaMM model, nonlinear rheological properties of monodisperse entangled linear polymer melts can be predicted even under strong flow, including in the strain rate region $\dot{\gamma}, \dot{\epsilon} > \tau_{\mathrm{R}}^{-1}$. Based on the GLaMM model, Likhtman and Graham derived a simple constitutive equation for fast flows of entangled linear polymer melts, which is called the Rouse linear entangled polymers (Rolie-Poly) constitutive equation [39]. The Rolie-Poly constitutive equation can capture nonlinear rheological properties of entangled linear polymer melts with a lower computational cost than that of the GLaMM model.

The abovementioned nonlinear constitutive models are limited to monodisperse linear polymer melts. Industrially, sourced polymers generally have a molecular weight distribution or a branched structure to ensure rheological properties suitable for processing. In the Rolie-Double-Poly (RDP) model, the double reptation theory [40] is combined with the Rolie-Poly model [41]. The RDP model can capture nonlinear shear and elongational rheology for bidisperse and polydisperse entangled linear polymers. However, it should be noted that the linear viscoelasticity predicted by the RDP model is not perfectly in agreement with experimental data [41].

For the polymer melts having two branch points and long-chain side branches, McLeish and Larson developed a molecular-based constitutive equation called the pom-pom constitutive equation [42]. The key idea of the pom-pom constitutive equation is to include branch point withdrawal, which allows free arms to move into the tube originally occupied by the backbone. This motion is induced by the backbone stretch relaxation. The pom-pom model can qualitatively predict nonlinear rheology under both shear and elongational flows of branched polymer melts. Moreover, the multimode pom-pom model can quantitatively predict nonlinear rheological properties for commercial polymer melts, such as low density polyethylene (LDPE) melts [43, 44].

Despite considerable efforts, it is still difficult to develop nonlinear constitutive models for polymer melts that have a molecular weight distribution or a branched structure from a molecular point of view. Alternatively, the following molecular-based coarse-grained simulation models are useful for predicting the linear and nonlinear rheology of entangled polymer melts.

1.2.4 Mesoscale Simulation Models

One of the successful mesoscale simulation models that can describe polymer dynamics in the entangled state is the slip-link (SL) model, in which entanglements are considered as "slip links". A short review on the SL models can be found in Ref. [45]. Here, a more extensive review on mesoscale simulation models is given. The concept of the SL model was first introduced by Doi and Edwards [46]. This original SL model only considered a single chain confined by slip links, and the effect of the motion of other chains, such as the CR, was not addressed.

Since then, many types of SL models have been developed based on the pioneering work of Doi and Edwards. Hua and Schieber proposed an SL model that considers the effect of the CR [47]. In the Hua-Schieber SL model, 1D Rouse chains that can slide along slip links are considered, and the slip links can be renewed and destroyed by the CR. After that, Schieber and coworkers developed a more mathematically rigorous SL model called the discrete SL model (DSM) [48, 49]. In addition to quantitative predictions of the linear rheology of monodisperse linear melts, the DSM can successfully predict the linear rheology of bidisperse blends [50], and linear and star blends [51]. Nonlinear rheological properties under both shear and elongational flows have also been examined using the DSM [52]. For shear viscosities, predictions obtained by the DSM are in good agreement with experimental results. However, the DSM shows strain-softening behavior in transient elongational viscosities. This behavior is not seen in experiments of entangled polystyrene melts [53]. Furthermore, the DSM was investigated from a thermodynamic point of view. For example, the DSM is consistent with the nonequilibrium thermodynamics formalism [54] known as the GENERIC framework [55, 56]. More recently, a more coarse-grained version of the DSM, called the clustered fixed SL model (CFSM), was developed by clustering several Kuhn steps of the DSM into a blob [57]. The CFSM can give rheological predictions equivalent to those of the DSM with a lower computational cost.

Masubuchi and coworkers developed the primitive chain network (PCN) model [58]. The PCN model can be considered as a real space model since a 3D entangled network of coarse grained polymer chains is described. Using the PCN model, various properties of entangled polymer melts and solutions have been examined, such as the linear rheology of monodisperse entangled polymer melts [59] and bidisperse blends [60], the linear and nonlinear rheology of branched polymer melts [61, 62], and the nonlinear properties of entangled linear polymers under strong uniaxial elongational flows including chain stretch [63, 64]. In addition to rheological properties, fundamental aspects of the PCN model, such as the detailed balance condition [65] and entanglement structure [66], have also been examined.

A more coarse-grained SL model than the above SL models was developed by Doi and

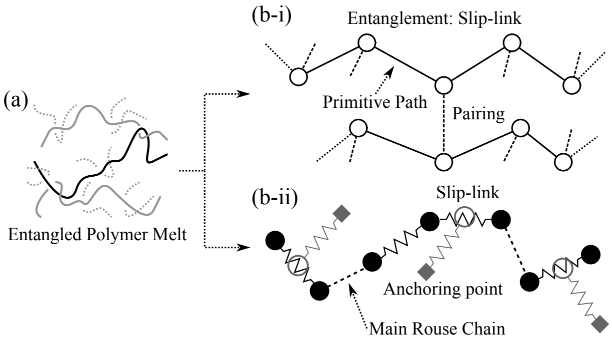

Fig. 1.3: Schematic illustration of modeling entanglements as slip-links. (a) An entangled polymer melt, and (b-i) the Doi-Takimoto slip-link model and (b-ii) Likhtman's slip-spring model.

Takimoto, which is schematically shown in Fig. 1.3 (b-i) [67]. The original Doi-Takimoto (DT) model can give good predictions for the linear rheology of monodisperse linear, polydisperse linear, and symmetric star polymer melt systems and for the nonlinear viscoelastic properties in the strain rate region $\tau_{\mathrm{d}}^{-1} < \dot{\gamma}, \dot{\epsilon} < \tau_{\mathrm{R}}^{-1}$. Furthermore, nonlinear rheological properties, including chain stretch ($\dot{\gamma}, \dot{\epsilon} > \tau_{\mathrm{R}}^{-1}$), were recently examined [45].

A simple SL model based on the SL model for branched polymers [68, 69] was proposed by Shanbhag, which is called ecoSLM [70]. Using ecoSLM, the linear rheological properties of monodisperse and bidisperse linear polymer melts were examined, and the results were in good agreement with the experimental data. However, the nonlinear viscoelastic properties under flows have not been investigated using ecoSLM.

Another type of coarse-grained model in which entanglements are modeled a priori is called the slip-spring (SS) model. Likhtman developed the single-chain SS model [71, 72], in which a polymer chain is described by a Rouse chain, and entanglements are modeled as additional springs that impose constraints on the main Rouse chain (Fig. 1.3 (b-ii)). Likhtman's SS model can predict experimental neutron scattering, linear rheology and diffusion data of unentangled and entangled monodisperse linear polymer melts. Furthermore, Likhtman's SS model is well defined from a thermodynamic point of view since this model satisfies the Gaussian statistics on all length scales of main Rouse chains and slip springs. The nonlinear rheological responses under steady shear flows were also investigated by the single-chain SS models similar to Likhtman's SS model [73, 74].

A multichain SS model was developed by Uneyama and Masubuchi [75]. This multichain SS model employs the total free energy of polymer chains and slip-springs [49] and satisfies the detailed balance condition. Using the multichain SS model, Masubuchi examined the nonlinear rheological properties of entangled linear polymer melts [76] and the linear rheological properties of branched polymer melts [77]. Furthermore, the PCN model, the multichain SS model, and the KG model were compared to develop a multi-scale approach that connects different length and time scales [78]. Another type of multichain SS model was developed by Theodorou and coworkers [79, 80]. In Theodorou's multichain SS model, a free energy is also defined, and the topology of the entanglement network is renewed using a kinetic Monte Carlo method. Theodorou's multichain SS model can successfully predict the linear and nonlinear rheology of monodisperse entangled linear polymer melts.

Recently, a more coarse-grained model than the SL and SS models was developed for strong elongational flows by Moghadam and coworkers, which is called entangled kink dynamics (EKD) [81, 82]. EKD utilizes the notion that entangled polymers become kinked or folded under strong uniaxial extensional flows. Using EKD, the nonlinear rheological properties under uniaxial elongational flows for high molecular weight polymers can be successfully captured, which fail to be captured by the conventional nonlinear tube theory.

1.2.5 Phenomenological Constitutive Equations

Despite the considerable success of the SL and SS models, phenomenological constitutive equations are frequently employed for industrial simulations mainly for the following two reasons [3]: First, phenomenological constitutive equations usually have a lower computational cost than more rigorous molecular-based models. Second, technically, there is less room for complexity in constitutive equations because industrial processing flow geometries are too complex.

Industrially, if the shear-rate-dependence of the viscosity is the most important aspect, and normal stress or elastic effects are negligible, the generalized Newtonian viscosity models, such as the power low model and the Carreau-Yasuda model, are employed to calculate the polymeric stress [83]. When the shear-rate-dependence of the viscosity, as well as normal stress or elastic effects play an important role in industrial flow problems, viscoelastic constitutive equations should be employed.

In this section, a brief review of viscoelastic phenomenological constitutive equations is given. Phenomenological constitutive equations can be roughly divided into the following two types: integral equations and differential equations. In practical simulations, phenomenological constitutive equations that can well describe experimental results are employed. Moreover, to give accurate predictions of nonlinear rheological properties using phenomenological constitutive equations, there are many parameters that should be determined by comparing with experiments.

One of the important integral constitutive equations was developed independently by Kaye [84] and Bernstein, Kearsley, and Zapas [85], which is called the Kaye-BKZ model. The Kaye-BKZ model is based on rubber elasticity theory, and the stress tensor can be derived from a free energy that depends on the invariants of the strain tensor. Since the elastic energy and the stress are allowed to relax in viscoelastic liquids, the elastic energy (and therefore the stress) can be expressed as a history integral. By comparing the model with step shear experiments, a specific functional form of the elastic energy for shear flows can be determined. After determining the elastic energy, the Kaye-BKZ model can be used to predict the nonlinear rheological properties under shear flows. However, it should be noted that step uniaxial elongation experiments are needed to determine the elastic energy for predicting the rheological properties under uniaxial elongational flows [3]. This means that it is difficult to accurately predict polymer processing flows, which are mixtures of flow types, using the Kaye-BKZ model.

There are various differential constitutive equations. One of the simplest differential constitutive equations for polymeric liquids is the Maxwell equation. The Maxwell equation is expressed as

$$\lambda \frac{\delta}{\delta t}\boldsymbol{\sigma} + \boldsymbol{\sigma} = 2\eta \boldsymbol{D}, \tag{1.11}$$

where $\delta/\delta t$ is the time derivative, λ is the relaxation time, and η is the viscosity. If we simply employ Eq. (1.11), then the stress tensor depends on rotation, which means that rotations induce stresses [3]. There is a basic principle that states constitutive equations should not depend on rotation, which is called the principle of "frame invariance". To recover frame invariance, the time derivative on the left-hand side of Eq. (1.11) should be modified. The upper convected derivative is one of the candidates for this modification. The model that the upper convected derivative is incorporated into the Maxwell model is called the upper convected Maxwell (UCM) model. In addition to the polymeric stress evaluated by the UCM model, if we consider the solvent stress, then the model is referred to as the Oldroyd-B model, which is frequently employed in simulations of polymer processing. Although the Oldroyd-B model is frequently employed as a model for expressing the viscoelasticity of polymeric liquids, the Oldroyd-B model cannot reproduce some important rheological properties of polymeric liquids. For example, linear differential equations, such as those in the UCM and Oldroyd-B models, cannot reproduce the thinning behavior in shear flows.

There are mainly two ways to solve the above problem. One is to consider nonaffine motion, and the other is to include higher order terms in constitutive equations. A more realistic rheological constitutive model can be obtained by removing the assumption of affine deformation, which is used in the UCM and Oldroyd-B models. One of the constitutive equations that allows nonaffine motion is the Larson model [86]. To address nonaffine motion, Larson proposed the partially extending convected derivative by introducing a parameter that represents the extent of strand retraction. The Larson model can capture the nonlinear rheological properties under shear and elongational flows better than the UCM and Oldroyd-B models. The Giesekus [87] and Leonov [88] models have a quadratic term in the stress, which can be interpreted as an accelerated relaxation. Including the quadratic term allows one to

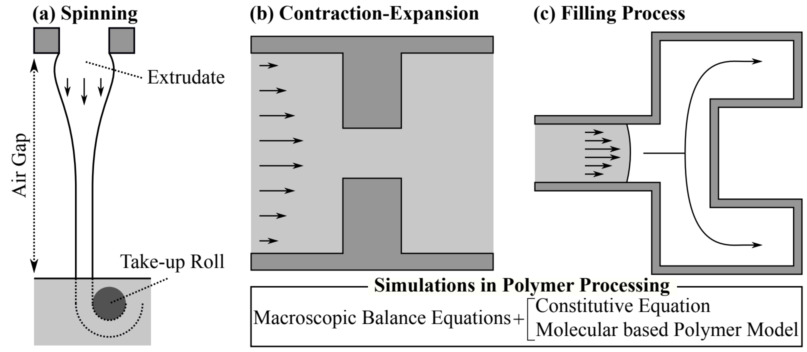

Fig. 1.4: Schematic illustration of simulation studies in polymer industries. (a) Polymer melt spinning process, (b) flows in a contraction-expansion channel, and (c) filling process.

obtain good rheological predictions under shear flows. However, the Giesekus and Leonov models give less accurate predictions under elongational flows than temporary network models [3], such as the PTT model mentioned below.

To present the PTT model, we explain temporary network models. Green and Tobolsky proposed a constitutive equation based on rubber elasticity theory, which is called the Green-Tobolsky (GT) model [89]. The GT model can be regarded as a type of temporary network model, since polymer chains in the GT model are considered to form a transient network that can break and reform. It should be noted that the GT model is equivalent to the UCM model. Therefore, the same problems as for the UCM model arise when employing the GT model. Generalized models based on the GT approach have been proposed. One of these generalized models is the Phan-Thien/Tanner (PTT) model [90], which allows non-Gaussian chains and a dependence of the breakage probability on polymer chain extension. The PTT model can give better predictions under elongational flows than the Giesekus and Leonov models.

1.2.6 Computer Simulations in Polymer Industry

For industrial purposes, macroscopic flow simulations are performed to predict the flow properties of polymeric liquids in complex flow geometries. In this section, a review of a polymer melt spinning process and an injection molding process, which are typical processes in the polymer industry, is given.

The polymer melt spinning process schematically shown in Fig. 1.4 (a) is a common process for manufacturing polymeric fibers. One of the pioneering studies on this process was performed by Kase and Matsuo [91, 92]. They developed a mathematical model for this process using a Newtonian fluid. After these pioneering studies were performed by Kase and Matsuo for a Newtonian fluid, constitutive equations, such as those in the Maxwell model [93] and the PTT model [94], were employed to address viscoelastic properties. Furthermore, microscopic structures, such as the molecular orientation and crystallization induced by uniaxial elongational flows, were examined by many researchers. Mathematical models for the spinning process, including thermally and flow-induced crystallization, were developed using the Giesekus model [95–97], or the multimode PTT model [98].

Since the injection molding process is one of the major production techniques in the polymer industry, there are many related studies from both experimental and numerical aspects. Injection molding is composed of many different process elements such as mixing, flow, filling, and shaping [99]. For the mixing process, Nakayama and coworkers analyzed this process using a shear thinning fluid [100, 101]. For flow properties, since the contraction-expansion channel (schematically shown in Fig. 1.4 (b)) can be considered one of the model geometries in the injection molding process, flows in this geometry have been extensively examined using phenomenological or molecular-based constitutive equations, including the Oldroyd-B model [102], the pom-pom model [103–105], and the Rolie-Poly model [106–110]. For the filling process schematically shown in Fig. 1.4 (c), free surface flows should be addressed. Numerically, using mesh-based methods, such as the finite element method (FEM), to address free surface flows is generally difficult due to the meshing problem. Lagrangian fluid particle methods are some of the effective methods for addressing flows including a free surface [111, 112].

The macroscopic flow properties (and the subsequent physical properties of polymer products) are determined by the microscopic states of polymer chains, including the molecular orientation and entanglements. Therefore, it is important to investigate the microscopic states of polymer chains in processing flows. Using tube-model-based constitutive models, such as the Rolie-Poly model or the pom-pom model, the molecular orientation and stretch can be obtained. However, when comparing with scattering experiments under flows, information on the molecular orientation and stretch is not sufficient to calculate structure factors, and a more detailed model such as the GLaMM model is required [106,108,110]. On the other hand, using the phenomenological constitutive equations, molecular information cannot be directly obtained. To obtain both macroscopic flow properties and microscopic molecular insights, other simulation techniques are needed.

1.3 Multi-Scale Simulation Method

Conventional fluid dynamics approaches with phenomenological viscoelastic constitutive equations can access length and time scales suitable for polymer processing. However, it is generally difficult to uniquely choose a proper constitutive equation that can fit experimental rheological data on a targeting polymer melt. Moreover, phenomenological constitutive equations are too coarse grained to directly obtain molecular insights that would be useful for designing polymer products. For these problems, the Multi-Scale Simulation (MSS) approach, in which a microscopic (or mesoscopic) model is connected to macroscopic balance equations, is one promising method. Using the MSS technique, both macroscopic flow properties and microscopic polymer dynamics can be evaluated. A short review on the MSS approaches can be found in Ref. [113]. Here, a more detailed review on transport problems using the MSS approaches is given.

A pioneering work on an MSS technique was performed by Laso and Öttinger, which was known as the Calculation of Non-Newtonian Flow: Finite Element and Stochastic Simulation Technique (CONNFFESSIT) [114]. In the original CONNFFESSIT approach, instead of employing phenomenological constitutive equations, the Hookean dumbbell model is employed

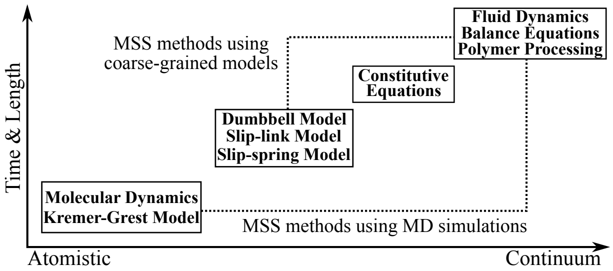

Fig. 1.5: Schematic illustration of MSS methods for transport phenomena of polymeric liquids.

to calculate the polymeric stress. Microscopic systems described by the Hookean dumbbell model are connected to macroscopic balance equations. These balance equations are solved by the FEM. The CONNFFESSIT technique was applied to the start-up Couette flow problem, and validated by comparing with solutions obtained from constitutive equations [114]. After that, various flow problems have been investigated using the CONNFFESSIT approach, such as flows in an abrupt contraction [115], start-up Couette flows for liquid crystals and polymer melts [116], time-dependent flows [117], and free surface flows [118]. Although the CONNFFESSIT is successful as a pioneering work, it has the following two main problems: the convection of microscopic components and the subsequent remeshing process in the FEM are calculation heavy, and microscopic information is limited since the simple Hookean dumbbell model is employed (except for the work of Hua and Schieber [116]). Based on the CONNFFESSIT approach, many variations of the MSS method have been developed. As shown in Fig. 1.5, we can roughly classify MSS methods into the following two categories: (1) MSS methods that combine macroscopic balance equations with an MD simulation, and (2) MSS methods that employ more coarse-grained models than MD and address the convection of microscopic systems.

1.3.1 MSS Methods using MD Simulations

As an MSS method using the MD simulation, the heterogeneous multi-scale method (HMM) proposed by E and coworkers is one of the successful methods [119, 120]. In the HMM, macroscopic balance equations are combined with MD simulations for Lennard-Jones (LJ) and dumbbell fluids. Macroscopic equations are solved using the finite volume method, and boundary conditions for MD simulations are obtained from macroscopic simulation. Using the HMM, typical flow problems such as a Poiseuille flow and a cavity flow were examined [120]. De and coworkers developed a scale-bridging method that combines macroscopic balance equations with the KG model [121, 122]. In this MSS method, the memory effect of a weakly entangled linear polymer melt for flows between parallel plates [121] and flows within a cylinder [122] can be accurately evaluated. Yasuda and Yamamoto proposed a hybrid simulation method of the macroscopic balance equation and MD simulations for LJ liquids based on the HMM [123]. In their hybrid simulation method, to properly employ the Lees-Edwards periodic boundary condition for MD simulations, the strain rate tensor calculated at the macroscopic level is transformed using a rotation matrix. Using their hybrid simulation method, the pressure-driven channel flow and the cavity flow of the LJ fluid were examined. Subsequently, the hybrid simulation method was extended to a polymer melt using the KG model, and various flow problems were examined [124–126]. More recently, Yasuda and Yamamoto developed the synchronized molecular dynamics (SMD) method that can address flow problems of complex fluids with temperature changes [127–129]. In the SMD, the KG simulations of local fluid elements are synchronized to satisfy the macroscopic momentum and energy equations at a macroscopic time interval. Using the SMD method, lubrication problems of unentangled [127,128] and weakly entangled [129] polymer melts were investigated.

In all MSS methods using MD simulations mentioned above, although detailed microscopic information can be obtained, there are mainly two limitations. First, the flow channel geometries are restricted to simple ones, such as flow between parallel plates, since it is impossible to set appropriate boundary conditions in MD simulations for general processing flows in which various types of flows are mixed, as mentioned in Sec. 1.2.1. Second, the polymer chains used in these MSS methods are relatively short or have few entanglements due to the large computational cost, which are not sufficient for most polymer processing flows.

1.3.2 MSS Methods using Coarse-grained Models

As an MSS method using a more coarse-grained model than MD, Hulsen and coworkers developed the Brownian configuration field (BCF) method, which can easily take the convection of microscopic systems into account [130]. In the BCF method, a time evolution equation of a configuration field of dumbbells is employed instead of individual polymer molecules, and the configuration field description is incorporated into the FEM. After confirming the validity of the BCF method by investigating flows around a cylinder using this method [130], various problems have been considered, including fibre suspension flows in contraction and expansion channels [131], free surface flows [132], 3D contraction flows [133], and nonequilibrium phase transitions of polymer solutions under shear flows [134]. Another variation of this type of the MSS method was developed by Halin and coworkers, which is called the Lagrangian particle method (LPM) [135,136]. In the LPM, the FEM for solving macroscopic balance equations is combined with the dumbbell model through a number of Lagrangian fluid particles on which the polymeric stress is calculated. Therefore, the deformation history of the polymers can be correctly addressed in the LPM. Using the LPM, the start-up flow between slightly eccentric rotating cylinders was examined. In all the MSS methods using coarse-grained models mentioned above, since the dumbbell model is employed to calculate the polymeric stress, the effect of entanglements is not addressed.

One of the MSS methods that addresses the effect of entanglements is the deformation field method [138, 139]. In the deformation field method, the deformation gradient fields are introduced to calculate the polymeric stress. Another approach was proposed by Masubuchi and coworkers. They developed a parameter-based bridging MSS method using the PCN model [140]. In their parameter-based bridging MSS method, the parameters of the viscoelastic constitutive equation (the multimode Leonov equation) were obtained from the

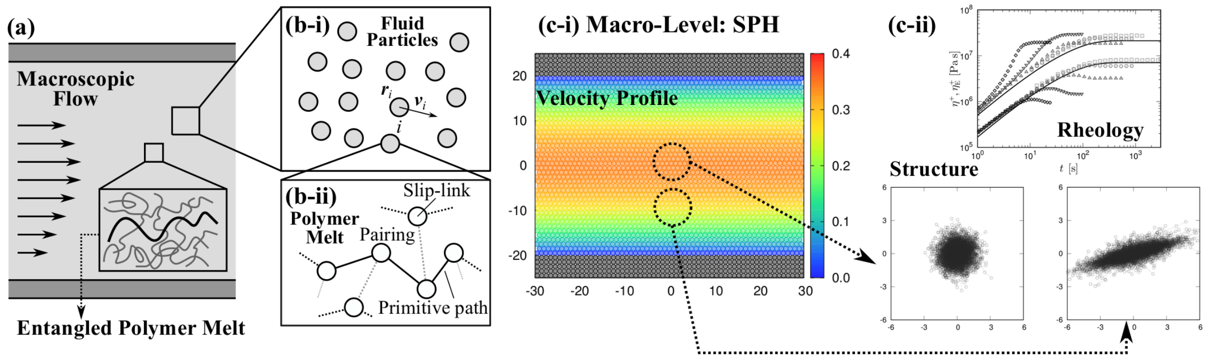

Fig. 1.6: (a) Schematic illustration of the system considered in the MSS of well-entangled polymer melts. (b) Schematic illustration of the MSS method proposed by Murashima and Taniguchi [137]. (c) Results of the MSS for (i) the macroscopic velocity field and (ii) microscopic rheological model predictions.

PCN model, and simulations of the filling process were performed. An MSS method that employs the smoothed particle hydrodynamics (SPH) method [141] as a macroscopic model and the dumbbell model was developed by Murashima and Taniguchi [142]. After that, they extended their MSS method to flows of an entangled linear polymer melt using the DT model, as schematically shown in Fig. 1.6 (a) and (b) [137,143,144]. Using this MSS method, both macroscopic (Fig. 1.6 (c-i)) and microscopic (Fig. 1.6 (c-ii)) information of the entangled polymer melt can be obtained without using phenomenological constitutive equations. Using an approach similar to the LPM, the author developed an MSS method that can calculate flows of a polymer melt spinning process using the dumbbell model [145] and the DT model [146]. More recently, flows of an entangled polymer melt in a contraction-expansion channel were examined using the MSS method by the author [113]. Moreover, it is fair to note that a similar MSS method was developed by Schieber and coworkers by employing the DSM as a microscopic level model [147].

In the MSS methods using more coarse-grained models than MD, microscopic details are limited because of coarse-graining. However, this type of MSS methods can access various processing flow problems of well-entangled polymer melts.

1.4 Thesis Objectives

Based on the abovementioned background, in this dissertation, the transport phenomena of entangled polymer melts are computationally investigated at both the macroscopic and microscopic levels. In particular, we focus on developing a Multi-Scale Simulation (MSS) method for transport problems of entangled polymer melts. To develop a sophisticated MSS method that can address polymer processing flow problems, we will focus on the following two problems:

(1) Microscopic coarse-grained models that describe the entangled polymer dynamics have not been fully developed. For example, under nonlinear flows frequently seen in polymer processing, rheological predictions of existing coarse-grained microscopic models, such as the Doi-Takimoto slip-link model [67], are not in reasonable agreement with the experimental data.

(2) Macroscopic flows in the polymer industry are quite diverse. There are various processing flows to manufacture polymer products. For example, some industrial polymer processes use complex flow channel geometries. That is, various flow types, such as shear flows and elongational flows, are mixed. As briefly discussed in Sec. 1.3.1, MD based MSS approaches cannot address complex flow problems. On the other hand, MSS approaches using coarse-grained models are effective to tackle complex flow problems. However, the aims of most of the studies on such MSS methods are to develop the computational methods themselves, and there are few studies that attempt to connect basic science and engineering.

Based on these problems, this dissertation is composed of five chapters, which are described bellow.

In **Chapter 2**, we focus on the Doi-Takimoto slip-link (DT) model [67] that is employed in the MSS as a microscopic coarse-grained model. The issue in this chapter is related to problem (1). First, the viscoelastic and statistical properties of the DT model are extensively examined. For the viscoelastic properties, we have confirmed that the original DT model can give good rheological predictions for the linear viscoelasticity of monodisperse linear, and symmetric star polymer melt systems, and the nonlinear rheological properties in a moderate strain rate region, where polymer chains are oriented without significant stretching. These results are consistent with the findings in the literature [67]. Furthermore, the nonlinear rheological properties under strong flows, with significant polymer chain stretching, which are important in polymer processing flows, are examined. For the statistical properties, we have investigated the validity of the entanglement structure obtained from the DT model by comparing with other coarse-grained models. This chapter describes the same results as those in Ref. [45].

The issues in **Chapter 3** and **Chapter 4** are related to problem (2). In these chapters, two typical flow problems in polymer processing are examined using the MSS method; one is a flow problem in an entangled polymer melt spinning process (**Chapter 3**), and the other is a flow problem in a contraction-expansion channel (**Chapter 4**). At the microscopic level of the MSS, we employ the DT model to address the entangled polymer dynamics. At the macroscopic level of the MSS, a Lagrangian fluid particle method appropriate for each process is employed, in order to address the effect of the flow history coming from the slow relaxation of entangled polymer chains.

In **Chapter 3**, the focus is on the entangled polymer melt spinning process. As described in Sec. 1.2.6, this is a common process for manufacturing polymeric fibers. At the macroscopic level, an Eulerian grid-based method and a Lagrangian fluid particle method are combined. The Eulerian grid-based method is employed to calculate macroscopic variables, such as the velocity. The polymeric stress is calculated on Lagrangian fluid particles that convect with the macroscopically obtained velocity. Using the developed MSS technique, both macroscopic and microscopic aspects of the entangled polymer melt spinning process are examined. To the best of our knowledge, the MSS approach for the entangled polymer melt spinning process is presented for the first time in our work. This chapter describes the same results as those in Ref. [146].

In **Chapter 4**, the focus is on flows in the contraction-expansion channel, which can be considered to be one of the model geometries of the injection molding process (as reviewed in Sec. 1.2.6). Unlike the polymer melt spinning process, flows in the contraction-expansion channel are mixtures of several flow types. Therefore, to correctly address the flow properties in the contraction-expansion channel, the smoothed particle hydrodynamics (SPH) method is employed as a macroscopic simulation model. At the microscopic level, the DT model is employed to calculate the polymeric stress. Using the developed MSS technique, both macroscopic and microscopic aspects of the flows in the contraction-expansion channel are examined. This chapter describes the same results as those in Ref. [113].

In **Chapter 5**, general conclusions are stated. The contents of this dissertation are summarized and the future perspectives are presented.

2 Rheology and Entanglement Structure of Well-Entangled Polymer Melts

2.1 Introduction

In this chapter, we focus specifically on the Doi-Takimoto slip-link model (DT model) [67], which describes entangled polymer dynamics. This coarse-grained model has a low computational cost compared with other molecular-based models. Therefore, the DT model can be employed as a microscopic model of MSSs for entangled polymer melt flows [113,137,142,146]. To realize a more sophisticated MSS using the DT model, we investigate the following two aspects of this model: (i) nonlinear rheological properties at a high strain rate region where polymer chains are stretched, and (ii) the statistical properties of the microscopic entanglement structure. First, to perform MSSs under polymer processing conditions, the rheological properties of fast flows should be correctly predicted by the DT model. Second, to utilize the microscopic structure obtained using MSSs for the molecular design of entangled polymer melts, the validity of the microscopic structure obtained from the DT model should be investigated through comparison with other (less coarse-grained) models.

In the DT model, because of the degree of coarse graining, relaxation mechanisms that are faster than the Rouse relaxation time τ_{R} are ignored. Therefore, the rheological properties for the high strain rate region $\dot{\gamma}, \dot{\epsilon} > \tau_{\mathrm{R}}^{-1}$ should be carefully examined. In fact, steady-state elongational viscosities obtained from the DT model show thinning behavior for $\dot{\epsilon} < \tau_{\mathrm{R}}^{-1}$ and hardening behavior for $\dot{\epsilon} > \tau_{\mathrm{R}}^{-1}$, as shown in the literature [67]. This behavior is not for typical entangled polymer melts but rather for typical entangled polymer solutions. To correctly predict steady-state elongational viscosities of entangled polymer melts, the concept of the stretch/orientation-induced reduction of molecular friction (SORF) was originally proposed by Ianniruberto *et al.* [148]. Yaoita *et al.* incorporated SORF into the Primitive Chain Network (PCN) model and found that SORF can improve the predictions of the rheological properties of entangled polystyrene (PS) melts under fast uniaxial elongational flows [64].

The effect of SORF has also been verified by incorporating SORF into the tube model-based constitutive equation [149, 150]. Masubuchi *et al.* have investigated the universality of SORF by comparing PCN simulations with experiments of polyisoprene (PI) and poly(*n*-butyl acrylate) (PnBA) [151]. More recently, Matsumiya *et al.* have examined the nonlinear elongational rheology of unentangled polymer melts and confirmed that the Rouse model with SORF can reproduce the steady elongational viscosity [152]. Based on the above background, in this chapter, we have investigated the effect of SORF on the DT model to achieve the above-stated purpose (i) and have clarified (ii) the statistical properties of the polymer chains described by the DT model with SORF.

2.2 Model and Simulation

2.2.1 Original Doi-Takimoto Slip-link Model

In this subsection, we briefly explain the DT model [67], which is schematically illustrated in Fig. 2.1. In the DT model shown in Fig. 2.1, a polymer chain is expressed by a primitive path and by slip links on the primitive path. A slip link represents an entanglement point between two different polymer chains.

In the DT model, the states of polymer chains are updated as follows. The position of a slip link $\boldsymbol{r}_j^{(i)}$ $(1 \leq j \leq Z_i(t))$ of a polymer chain i $(1 \leq i \leq N_\mathrm{p})$ is evolved affinely according

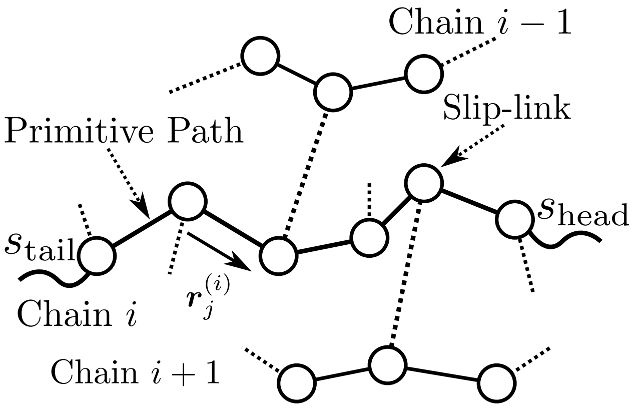

Fig. 2.1: Schematic illustration of the slip-link model developed by Doi and Takimoto [67].

to an applied velocity gradient tensor $\boldsymbol{\kappa}$ as

$$\Delta \boldsymbol{r}_j^{(i)} = \boldsymbol{r}_j^{(i)}(t+\Delta t) - \boldsymbol{r}_j^{(i)}(t) = \boldsymbol{\kappa} \cdot \boldsymbol{r}_j^{(i)} \tag{2.1}$$

where $Z_i(t)$ is the number of entanglements on the primitive path of the polymer chain i at time t and N_p is the number of polymer chains. In the DT model, relaxation mechanisms faster than the Rouse time τ_R (e.g., force balance and fluctuation at entanglements) are assumed to be ignored. In fact, Masubuchi *et al.* [153] have reported that the multichain slip-link model without force balance can qualitatively capture the entangled polymer dynamics in the linear region because the important relaxation mechanism is the reptation. However, the effect of this assumption on the rheological properties, especially in the nonlinear region, should be carefully examined by comparing with other models. Subsequently, the contour length of a primitive path L_i is updated as

$$\begin{aligned} \Delta L_i &= L_i(t+\Delta t) - L_i(t) \\ &= -\frac{1}{\tau_\mathrm{R}}\left(L_i(t) - L_0\right)\Delta t + \Delta L_{\mathrm{affine},i} + \sqrt{\frac{2a^2\Delta t}{3Z_0\tau_\mathrm{e}}}w_{\mathrm{L},i}, \end{aligned} \tag{2.2}$$

where $L_i = \sum_{j=1}^{Z-1} |\boldsymbol{r}_j^{(i)}| + s_{\mathrm{head},i} + s_{\mathrm{tail},i}$ is the length of the primitive path of the polymer chain i, and $s_{\mathrm{head},i}$ and $s_{\mathrm{tail},i}$ are the contour lengths of the two ends, head and tail, respectively. Note that the primitive path is composed of $(Z_i(t) - 1)$ entangled strands and two ends. $L_0 = Z_0 a$ is the equilibrium length of the primitive path, Z_0 is the equilibrium number of strands per chain, a is the equilibrium length between adjacent slip links, $\tau_\mathrm{R} = Z_0^2\tau_\mathrm{e}$ is the Rouse relaxation time, τ_e is the unit time of the DT model, $\Delta L_{\mathrm{affine},i}$ is the change in length caused by the affine deformation, and $w_{\mathrm{L},i}$ is a Gaussian random number with zero mean and unit variance. The reptation motion can be described as the motion of the two free ends by the following two equations:

$$\Delta s_{\mathrm{head},i} = s_{\mathrm{head},i}(t+\Delta t) - s_{\mathrm{head},i}(t) = \frac{1}{2}\left[\Delta L_i - \Delta L_{\mathrm{affine},i}\right] + \sqrt{2D_{\mathrm{c}}\Delta t}\; w_{\mathrm{s},i}, \tag{2.3}$$

$$\Delta s_{\mathrm{tail},i} = s_{\mathrm{tail},i}(t+\Delta t) - s_{\mathrm{tail},i}(t) = \frac{1}{2}\left[\Delta L_i - \Delta L_{\mathrm{affine},i}\right] - \sqrt{2D_{\mathrm{c}}\Delta t}\; w_{\mathrm{s},i}, \tag{2.4}$$

where $D_{\mathrm{c}} = L_0^2/(\pi^2\tau_{\mathrm{d}}^{\mathrm{DE}})$ is the diffusion constant, $\tau_{\mathrm{d}}^{\mathrm{DE}} = 3Z_0^3\tau_{\mathrm{e}}$ is the reptation time calculated from the Doi-Edwards model [21], and $w_{\mathrm{s},i}$ is a Gaussian random number with zero mean and unit variance.

The number of entanglements $Z_i(t)$ is changed by the motions of its chain ends and the motions of other chains entangled with this chain (constraint release; CR). When $s_{\mathrm{head},i}$ ($s_{\mathrm{tail},i}$) becomes less than zero, the slip link on the chain end of the polymer chain i is removed. At the same time, the slip link coupled to the removed one is also removed in a way that mimics the CR. Conversely, when $s_{\mathrm{head},i}$ ($s_{\mathrm{tail},i}$) becomes larger than a, a new slip link is created at the head (tail). Simultaneously, a partner polymer chain entangled with the new slip link is randomly selected from other polymer chains. A new slip link is created on a strand that is randomly selected from strands of the partner polymer chain with a probability that is proportional to strand lengths.

The stress tensor is calculated as

$$\sigma_{\alpha\beta} = \sigma_{\mathrm{e}} \left\langle f \frac{r_{i\alpha} r_{i\beta}}{a\,|\boldsymbol{r}_i|} \right\rangle, \quad \alpha, \beta \in \{x, y, z\} \tag{2.5}$$

where f is the FENE factor defined as $f \equiv (1-\lambda_{\mathrm{eq}}^2)/(1-\lambda^2)$, $\lambda \equiv L/L_{\max}$ is the stretch ratio, $L_{\max}$ is the maximum length of primitive paths, and $\langle\cdots\rangle$ is the statistical average over N_{p} polymer chains. The unit stress σ_{e} is expressed as

$$\sigma_{\mathrm{e}} = \frac{3k_{\mathrm{B}}TZ_{\mathrm{total}}}{V} = \frac{3\rho RT}{M_{\mathrm{e}}} = \frac{15}{4}G_{\mathrm{N}}, \tag{2.6}$$

where M_{e} is the entanglement molecular weight and G_{N} is the plateau modulus. In general, the relation between G_{N} and M_{e} is expressed as $M_{\mathrm{e}} = A\rho RT/G_{\mathrm{N}}$, where A is the model-dependent prefactor. For the DT model, A is the same as in the Doi-Edwards model [21], $A = 0.8$, as shown in Eq. (2.6). The unit time τ_{e} and the unit stress σ_{e} can be determined using linear viscoelasticity data obtained from an experiment.

2.2.2 Improvement of the DT Model

The DT model explained in Sec. 2.2.1 can successfully predict linear and nonlinear rheologies of entangled linear or symmetric star polymer melts for strain rates less than τ_{R}^{-1}. However, in the DT model, the dynamics of an entangled polymer chain in a time scale shorter than the Rouse relaxation time τ_{R} is ignored to enhance the computational efficiency. Thus, the results obtained from the DT model simulations under fast flows ($\dot{\gamma}, \dot{\epsilon} \gtrsim \tau_{\mathrm{R}}^{-1}$) may not be reliable. For example, the original DT model shows that steady-state elongational viscosity increases when the elongational strain rate is larger than τ_{R}^{-1}, as shown later. Experimentally, this behavior is not observed for entangled polymer melts. Computationally, by use of the PCN model, the viscosity behavior under fast flows was discussed by Yaoita *et al.* [63, 64]. They argued that the important mechanism for suppressing the increase in elongational viscosity under fast elongational flows is the stretch/orientation-induced reduction of friction (SORF) originally proposed by Ianniruberto *et al.* [148]. Yaoita *et al.* [64] reported that SORF can improve the prediction of steady elongational viscosities, especially under fast elongational flows ($\dot{\epsilon} > \tau_{\mathrm{R}}^{-1}$). To investigate the effect of SORF on the DT model, we have incorporated SORF with the DT model as follows (for more information on SORF, see Ref. [64]). To incorporate SORF with the DT model, we have assumed that the change in the friction coefficient can be mapped to the change in the unit time τ_{e} in the DT model and that τ_{e} can be expressed as a function of the stretch/orientation factor $F_{\mathrm{s/o}} \equiv \lambda^2 \bar{S}$ as

$$\frac{\tau_{\mathrm{e}}(F_{\mathrm{s/o}})}{\tau_{\mathrm{e}}(0)} = \frac{\zeta(F_{\mathrm{s/o}})}{\zeta(0)} \frac{1}{f_{\mathrm{FENE}}} = \frac{1}{(1+\beta)^{\gamma}} \left[\beta + \frac{1 - \tanh\left[\alpha\left(F'_{\mathrm{s/o}} - F'^{*}_{\mathrm{s/o}}\right)\right]}{2} \right]^{\gamma} \tag{2.7}$$

Table 2.1: Parameters of samples examined by the DT model.

sample	M [kg/mol]	Z_0	T [°C]	$\tau_\mathrm{e}(0)^a$ [s]	$\sigma_\mathrm{e}{}^a$ [Pa]	λ_max
PS145K [154]	145	14	120	3.6	7.3×10^5	4.4
PS200K [53,155]	200	19	130	0.15	6.7×10^5	4.4
PS200K-Shear [156]	200	19	175	1.9×10^{-4}	7.7×10^5	4.4
PS390K [53,155]	390	37	130	0.15	6.7×10^5	4.4
PS90K-Star [157]	92.4	9	130	0.23	8.4×10^5	4.4
PI145K [158]	145	29	21.5			5.9

^{a} From the linear viscoelasticity data.

where $F'_\mathrm{s/o}$ is a parameter defined as $F'_\mathrm{s/o} \equiv F_\mathrm{s/o} f_\mathrm{FENE}$, $\bar{S}$ is the averaged orientation parameter, and α, β, γ and $F'^{*}_\mathrm{s/o}$ are parameters. Eq. (2.7) is an empirical equation that is determined from the experimental data [64]. The parameters in Eq. (2.7) for PS are determined to fit the experimental data as $\alpha = 20$, $\beta = 5.0 \times 10^{-9}$, $\gamma = 0.15$ and $F'^{*}_\mathrm{s/o} = 0.14$ in the literature [64]. Note that it is still uncertain whether the assumption that $\tau_\mathrm{e}(F_\mathrm{s/o})$ can be described using Eq. (2.7) with the original parameters is valid for the DT model where the dynamics faster than τ_R^{-1} is ignored. However, the determination of appropriate parameters for the DT model is deferred to a future work because one of the purposes in this chapter is to investigate the effect of SORF on the DT model. $\bar{S}$ is defined as

$$\bar{S} \equiv \sqrt{|\lambda_1 - \lambda_2|^2} = \sqrt{\{\mathrm{Tr}(\boldsymbol{S})\}^2 - 4\mathrm{det}(\boldsymbol{S})} = \sqrt{\left(\langle u_x^2 - u_y^2 \rangle\right)^2 + 4\langle u_x u_y \rangle^2}, \tag{2.8}$$

where $\boldsymbol{u}$ is the unit vector defined as $\boldsymbol{u} \equiv \boldsymbol{r}/|\boldsymbol{r}|$, $S_{\alpha\beta} \equiv \langle u_\alpha u_\beta \rangle$ $(\alpha, \beta \in x, y)$, and λ_1 and λ_2 are the eigenvalues of $\boldsymbol{S}$. Under shear flows, x is the flow direction, and y is the velocity gradient direction. Meanwhile, under elongational flows, x is the elongation direction, and y is orthogonal to the elongation direction. Moreover, f_FENE is the FENE-P factor defined as

$$f_\mathrm{FENE} \equiv \frac{1}{1 - \left(\langle L \rangle / L_\mathrm{max}\right)^2}. \tag{2.9}$$

In Eqs. (2.8) and (2.9), $\langle \cdots \rangle$ is the ensemble average of $(\cdots)$.

In the simulations, the equilibrium length between adjacent slip links a is used as the

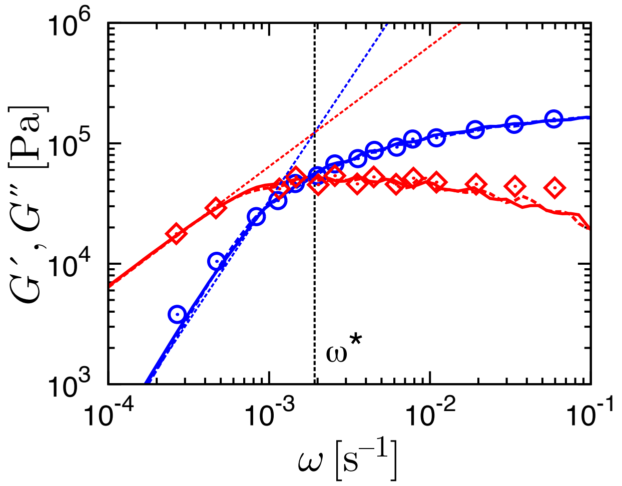

Fig. 2.2: Linear viscoelasticity of the monodisperse linear polystyrene melt. Circles and diamonds, respectively, indicate G' and G'' extracted from Ref. [53]. The simulation results with and without SORF are shown by dashed and solid lines, respectively.

unit length, $\tau_e(0)$ is the unit time, and σ_e is the unit stress. We focus on the rheological properties of entangled linear PS melts, an entangled star PS melt, and an entangled linear PI melt. The maximum length is set to $L_{\max} = 4.4L_0$ for PS and $L_{\max} = 5.9L_0$ for PI in the following simulations. The parameters used in this study are summarized in Table 2.1.

2.3 Results and Discussion

2.3.1 Linear Regime

Fig. 2.2 shows the linear viscoelasticity of a linear monodisperse PS polymer melt with a molecular weight $M_w = 200$ K ($Z_0 = 19$) (henceforth, it is referred to as PS200K). Before applying a strain or a strain rate, the system is fully equilibrated under $\boldsymbol{\kappa} = \mathbf{0}$; namely, we equilibrate the system for a time duration that is longer than the theoretically estimated longest relaxation time τ_d^{DE}. After the equilibration, the average number of entanglements $\langle Z \rangle_{\mathrm{eq}}$ is found to be $\langle Z \rangle_{\mathrm{eq}} \simeq 20$. The storage modulus $G'(\omega)$ and loss modulus $G''(\omega)$ are calculated by Eqs. (2.11) and (2.12) using the stress relaxation modulus $G(t)$ in Eq. (2.10) after applying step shear strain $\gamma_0 = 0.4$. As shown in Fig. 2.3, the system remains in the linear region after applying step shear strain $\gamma_0 = 0.4$ because the damping function $h(\gamma)$ is

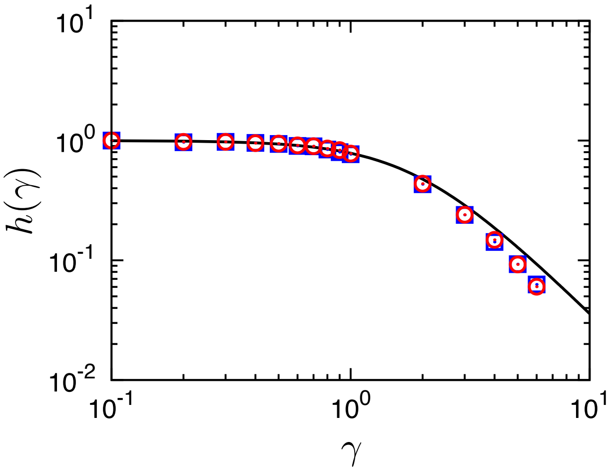

Fig. 2.3: Damping function $h(\gamma)$ of PS200K with (red circles) and without SORF (blue squares). The solid black line is the prediction by the Doi-Edwards model [21].

almost equal to unity.

$$G(t) = \frac{\sigma_{xy}(t)}{\gamma_0} \tag{2.10}$$

$$G'(\omega) = \omega \int_0^\infty G(t)\mathrm{sin}\omega t dt \tag{2.11}$$

$$G''(\omega) = \omega \int_0^\infty G(t)\mathrm{cos}\omega t dt \tag{2.12}$$

The unit time $\tau_\mathrm{e}(0)$ and the unit stress σ_e can be determined through comparison with the experimental data [53] as $\tau_\mathrm{e}(0) = 0.15$ s and $\sigma_\mathrm{e} = 0.67$ MPa for PS at 130 °C. In addition, since $G'(\omega)$ is proportional to ω and $G''(\omega)$ is proportional to ω^2 in the terminal relaxation region, the longest relaxation time τ_d can be determined using the intersection of two lines ω^* as $\tau_\mathrm{d} \simeq (2\pi/\omega^*)\tau_\mathrm{e}(0)$. From Fig. 2.2, the longest relaxation time is determined to be $\tau_\mathrm{d} \simeq 2.1 \times 10^4\tau_\mathrm{e}(0)$. As shown in Fig. 2.2, the simulation results with and without SORF are almost identical, which means that the inclusion of SORF does not alter the rheological behavior in the linear regime of the DT model and the effect of SORF would appear in a nonlinear regime where polymer chains are highly oriented and stretched.

We turn to analysis of the statistical properties of the microscopic structure obtained from the SL simulation at equilibrium. The following results are useful for examining the

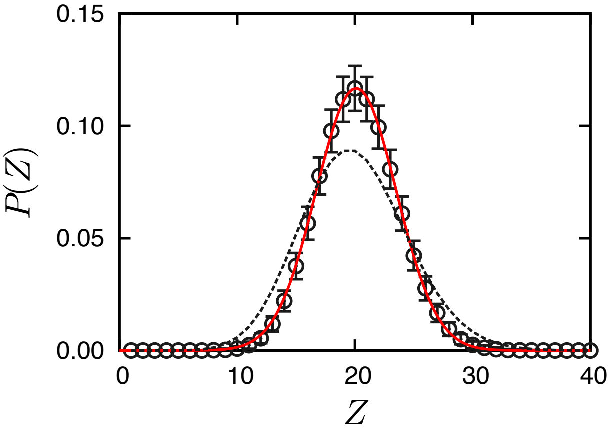

Fig. 2.4: The probability distribution of the number of slip links per chain $P(Z)$ at equilibrium. Here, $P(Z)$ is calculated by taking ensemble averages of $N_\mathrm{p} = 1000$ chains. The black dashed line and the red solid line indicate the Poisson distribution with the same mean as the data and the fitted Gaussian distribution, respectively.

microscopic structure of entangled polymer melts by using our MSS technique [113]. Fig. 2.4 shows the probability distribution of the number of slip links per chain $P(Z)$ at equilibrium. As clearly shown in Fig. 2.4, the $P(Z)$ obtained from our SL simulation is narrower than that of the theoretically expected Poisson distribution [48]. This result is consistent with the findings in Ref. [66], as discussed in our previous work [113].

2.3.2 Nonlinear Regime

Fig. 2.5 shows viscosity growth and relaxation on start-up and cessation of uniaxial elongational flows for the PS145K melt obtained by the DT model with (red dashed lines) and without (solid lines) SORF. The symbols in Fig. 2.5 are the experimental data extracted from the literature [154]. From Fig. 2.5, we can clearly observe the effect of SORF on the DT model. That is, although the simulations without SORF overpredict the experimental data, the simulations with SORF provide considerably better predictions and are in reasonable agreement with the experimental data.

Fig. 2.6 shows (a) the transient uniaxial elongational viscosities $\eta_\mathrm{E}^+(t)$ plotted against time t for various elongational strain rates and (b) the steady-state uniaxial elongational viscosities η_E against Weissenberg numbers defined as $\mathrm{Wi}_\mathrm{R}^{(\mathrm{e})} \equiv \dot{\epsilon}\tau_\mathrm{R}$. Dashed and solid lines indicate the

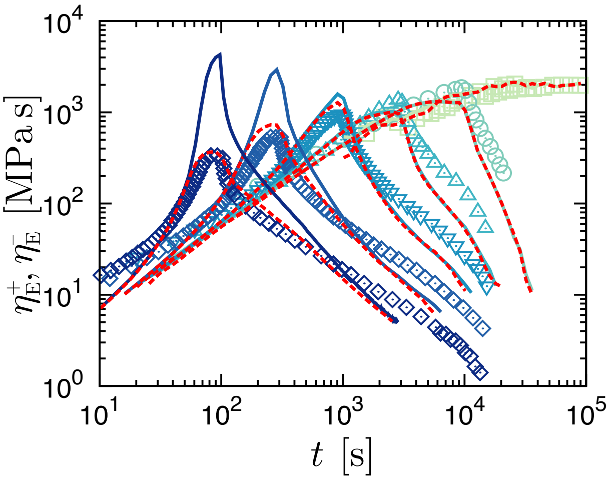

Fig. 2.5: Viscosity growth and relaxation on start-up and cessation of uniaxial elongational flow for PS145K melt at 120 °C. Dashed and solid lines indicate the SL simulation results with and without the stretch/orientation-induced reduction of friction, respectively. Strain rates are 0.03, 0.01, 0.003, 0.001, 0.0003, and 0.00001 s^{-1} from left to right, and the strain at the flow cessation is $\epsilon_0 = 3.0$. The experimental data from Ref. [154] are shown with symbols.

SL simulation results with and without SORF, respectively. From Fig. 2.6 (a), at the lowest strain rate ($\dot{\epsilon} = 0.001$ s^{-1}, $\text{Wi}_\text{R}^{(\text{e})} \simeq 0.05$), the transient uniaxial elongational viscosity shows almost identical behavior as the linear viscoelasticity growth function $3\eta_0^+(t)$. As briefly noted in Sec. 2.2.2, we can observe that the simulation results with and without SORF are almost identical for the relatively small strain rate region ($\dot{\epsilon} \lesssim 0.01\text{s}^{-1}$, $\text{Wi}_\text{R}^{(\text{e})} \lesssim 0.5$). We can clearly observe the effect of SORF in the high strain rate region ($\dot{\epsilon} \gtrsim 0.03\text{s}^{-1}$, $\text{Wi}_\text{R}^{(\text{e})} \gtrsim 1.5$). In the high strain rate region ($\dot{\epsilon} \gtrsim 0.03\text{s}^{-1}$, $\text{Wi}_\text{R}^{(\text{e})} \gtrsim 1.5$), the SL simulations without SORF clearly overpredict the steady-state values of uniaxial elongational viscosities, as shown by the solid lines in Fig. 2.6 (a). Meanwhile, the SL simulations with SORF can improve the predictions of steady-state uniaxial elongational viscosities, and the results are in good agreement with the experimental data [53], as shown by the red dashed lines in Fig. 2.6 (a). From Fig. 2.6 (b), the steady-state uniaxial elongational viscosities obtained from the SL simulations without SORF exhibit thinning behavior for $\dot{\epsilon} \lesssim \tau_\text{R}^{-1}$ and hardening behavior for $\dot{\epsilon} \gtrsim \tau_\text{R}^{-1}$, which are typically observed in entangled polymer solutions [159]. In contrast, steady-state uniaxial elongational viscosities obtained from the SL simulation with SORF exhibit thinning behavior followed by

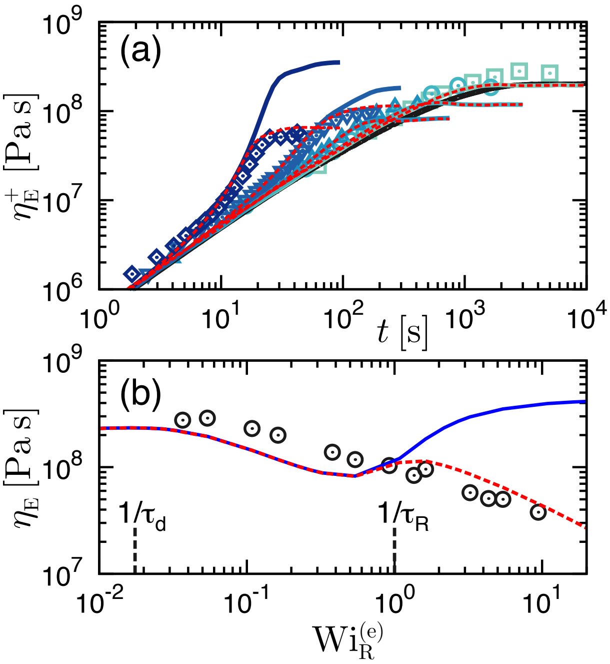

Fig. 2.6: (a) Transient uniaxial viscosities and (b) steady-state uniaxial elongational viscosities for a PS200K melt at 130°C. Dashed and solid lines indicate the SL simulation results with and without the stretch/orientation-induced reduction of friction, respectively. In (a), the strain rates are 0.1 (diamonds), 0.03 (reverse triangles), 0.01 (triangles), 0.003 (circles) and 0.001 (squares) s^{-1} from left to right, and the bold solid line is the linear viscosity growth function $3\eta_0^+(t)$ calculated from the linear viscoelasticity data. The experimental data for (a) and (b) from Refs. [53] and [155] are shown with symbols, respectively.

a slight increase at approximately $\dot{\epsilon} \simeq \tau_R^{-1}$. The increase in steady-state elongational viscosity at approximately $\dot{\epsilon} \simeq \tau_R^{-1}$ occurs presumably because there is no relaxation mechanism for time scales shorter than τ_R in the DT model. Nevertheless, we can conclude that SORF can significantly improve the agreement with the rheological data of PS200K [155] in the DT model. For entangled PS that has a different molecular weight (PS390K), the tendency in viscosities is almost the same as that of PS200K (for more details, see Appendix 2.A). Fig. 2.7 shows (a) the reduced chain stretch squared λ^2, (b) the average orientation $\bar{S}$ calculated from Eq. (2.8), and (c) the number of slip links per chain normalized using the equilibrium value $Z/\langle Z\rangle_{\mathrm{eq}}$ at steady states under uniaxial elongational flows as functions of $\mathrm{Wi}_R^{(e)}$. The dashed and solid lines indicate the SL simulation results with and without SORF, respectively. As shown in Fig. 2.7 (a), the reduced chain stretch squared λ^2 with SORF is reduced in the high

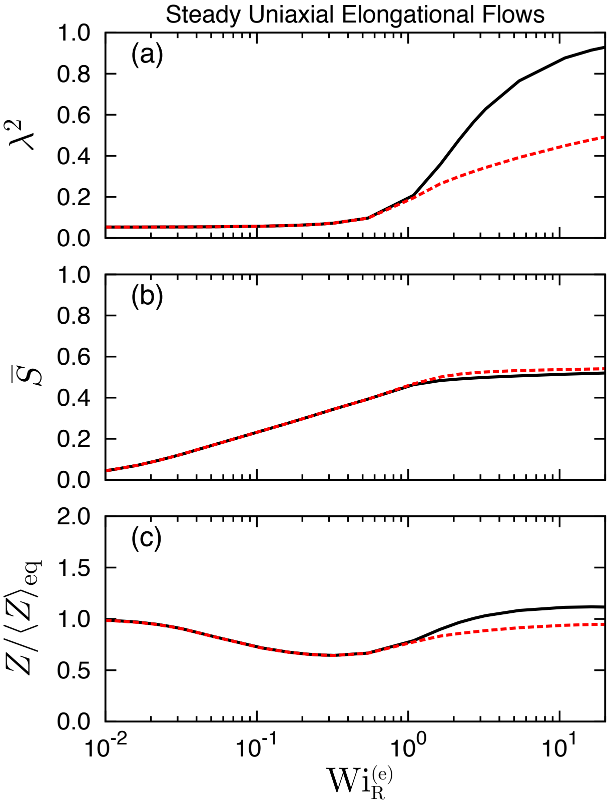

Fig. 2.7: (a) The reduced chain stretch squared λ^2, (b) the average orientation $\bar{S}$ and (c) the number of slip links per chain normalized using the equilibrium value $Z/\langle Z\rangle_{\rm eq}$ under uniaxial elongational flows. These values are plotted against the Rouse-relaxation-time-based Weissenberg number $\mathrm{Wi}_{\mathrm{R}}^{(\mathrm{e})} \equiv \dot{\epsilon}\tau_{\mathrm{R}}$. The simulation results with and without SORF are indicated with dashed and solid lines, respectively.

strain rate region $\mathrm{Wi}_{\mathrm{R}}^{(\mathrm{e})} \gtrsim 1$. For the average orientation $\bar{S}$ shown in Fig. 2.7 (b), there is little difference between the cases with and without SORF. These behaviors can also be observed in the literature [64]. However, for the number of slip links per chain normalized using the equilibrium value $Z/\langle Z\rangle_{\rm eq}$, nonmonotonic behavior can be observed, particularly for the case without SORF (black solid line); that is, as $\mathrm{Wi}_{\mathrm{R}}^{(\mathrm{e})}$ increases, $Z/\langle Z\rangle_{\rm eq}$ first decreases and then increases. This behavior in the high strain rate region $\mathrm{Wi}_{\mathrm{R}}^{(\mathrm{e})} > 1$ cannot be found in the literature [64, 80]. Although the result becomes close to the result in the literature [64] if we consider the SORF, the qualitative behavior remains unchanged (comparison with the PCN model for PS390K is shown in Fig. 2.21 (c)). This result indicates that the validity of the microscopic structure obtained from the DT model even with SORF in the strain rate

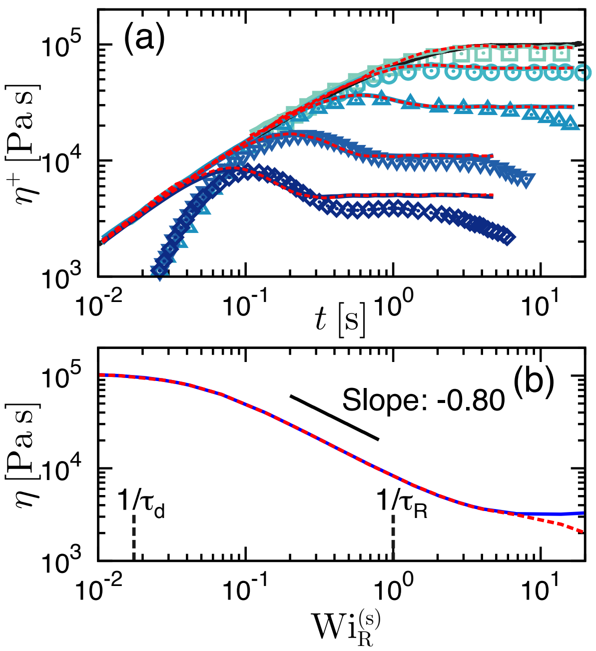

Fig. 2.8: (a) Transient shear viscosities and (b) steady shear viscosities for a PS200K melt at 175°C. Dashed and solid lines indicate the SL simulation results with and without the stretch/orientation-induced reduction of friction, respectively. In (a), the strain rates are 30 (diamonds), 10 (reverse triangles), 3 (triangles), 1 (circles) and 0.3 (squares) s^{-1} from left to right, and the bold solid line is the linear viscosity growth function $\eta_0^+(t)$ calculated from the linear viscoelasticity data. In (a), the experimental data from Ref. [156] are shown with symbols.

region $\mathrm{Wi}_\mathrm{R}^{(\mathrm{e})} > 1$ is questionable and should be examined in detail by comparison with other less-coarse-grained models. However, detailed examination of the microscopic structure in the strain rate region $\mathrm{Wi}_\mathrm{R}^{(\mathrm{e})} > 1$ is beyond the scope of this work and is deferred to future work.

Fig. 2.8 shows (a) the transient shear viscosities $\eta^+(t)$ plotted against time t for various shear strain rates and (b) the steady shear viscosities η plotted against Weissenberg numbers defined as $\mathrm{Wi}_\mathrm{R}^{(\mathrm{s})} \equiv \dot{\gamma}\tau_\mathrm{R}$. The dashed and solid lines indicate the SL simulation results with and without SORF, respectively. In Fig. 2.8 (a), for the examined strain rate region $\dot{\gamma} \lesssim 30\mathrm{s}^{-1}$ that corresponds to $\mathrm{Wi}_\mathrm{R}^{(\mathrm{s})} \lesssim 2$, there is no significant difference in the transient shear viscosities $\eta^+(t)$ between the cases with and without SORF, and the simulation results are in good agreement with the experimental data [156]. This result is consistent with the discussion in

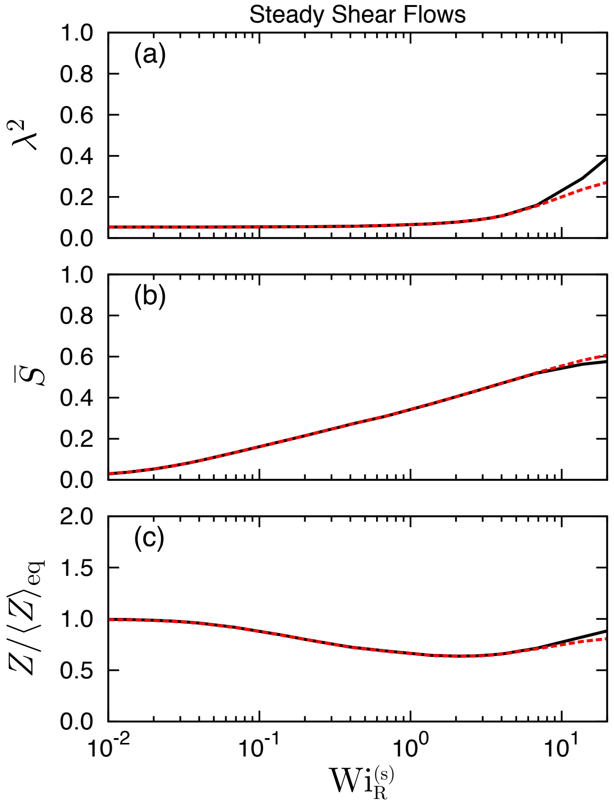

Fig. 2.9: (a) The reduced chain stretch squared λ^2, (b) the average orientation $\bar{S}$ and (c) the number of slip links per chain normalized using the equilibrium value $Z/\langle Z\rangle_{\mathrm{eq}}$ under shear flows. These values are plotted against the Rouse-relaxation-time-based Weissenberg number $\mathrm{Wi}_{\mathrm{R}}^{(\mathrm{s})} \equiv \dot{\gamma}\tau_{\mathrm{R}}$. The simulation results with and without SORF are indicated with dashed and solid lines, respectively.

the literature [64]. As shown in Fig. 2.8 (b), shear thinning behavior starts at a shear rate of approximately $\mathrm{Wi}_{\mathrm{d}}^{(\mathrm{s})} \simeq 1$. For $\tau_{\mathrm{d}}^{-1} < \dot{\gamma} < \tau_{\mathrm{R}}^{-1}$, the shear viscosity can be described by a power law of $\eta \propto \left\{\mathrm{Wi}_{\mathrm{R}}^{(\mathrm{s})}\right\}^{-0.8}$, and this exponent is in good agreement with the experimentally obtained value [4]. From Fig. 2.8 (b), the effect of SORF can be observed in $\mathrm{Wi}_{\mathrm{R}}^{(\mathrm{s})} \gtrsim 10$. Although the system without SORF exhibits plateau values of shear viscosities in $\mathrm{Wi}_{\mathrm{R}}^{(\mathrm{s})} \gtrsim 10$, the system with SORF exhibits monotonic thinning. A difference exists between uniaxial elongational and shear flows in $\mathrm{Wi}_{\mathrm{R}}^{(\mathrm{e/s})}$, where the effect of SORF begins to work, namely, $\mathrm{Wi}_{\mathrm{R}}^{(\mathrm{e})} \simeq 1.5$ and $\mathrm{Wi}_{\mathrm{R}}^{(\mathrm{s})} \simeq 10$. This difference originates mainly from the difference in $\mathrm{Wi}_{\mathrm{R}}^{(\mathrm{e/s})}$, where polymer chains start to stretch, as discussed in the next paragraph. In Fig. 2.9, we also show (a) the reduced chain stretch squared λ^2, (b) the average orientation $\bar{S}$ calculated

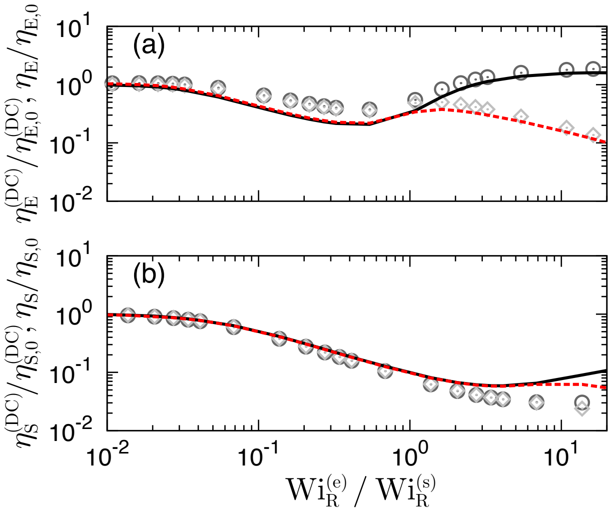

Fig. 2.10: (a) The normalized decoupled elongational viscosity $\eta_E^{(DC)}/\eta_{E,0}^{(DC)}$ and (b) the normalized decoupled shear viscosity $\eta_S^{(DC)}/\eta_{S,0}^{(DC)}$. The results of the decoupling approximation with and without SORF are indicated with dashed and solid lines, respectively. Furthermore, (a) the normalized elongational viscosity $\eta_E/\eta_{E,0}$ and (b) the normalized shear viscosity $\eta_S/\eta_{S,0}$ are shown as references. The simulation results with and without SORF are indicated with diamonds and circles, respectively.

from Eq. (2.8), and (c) the number of slip links per chain normalized using the equilibrium value $Z/\langle Z\rangle_{\mathrm{eq}}$ at steady states under shear flows. We can observe only a slight difference between the cases with and without SORF in the high $\mathrm{Wi}_R^{(s)}$ region. This result is consistent with the discussion of the result in Fig. 2.8.

If we adopt a decoupling approximation, the stresses under elongational and shear flows, $\sigma_{E/S}$, can be expressed as $\sigma_{E/S} \sim f_{\mathrm{FENE}}\lambda^2\bar{S}(Z/\langle Z\rangle_{\mathrm{eq}})$. By use of the stresses $\sigma_{E/S}$, we define the elongational and shear viscosities as $\eta_E^{(DC)} \equiv \sigma_E/\dot{\epsilon}$ and $\eta_S^{(DC)} \equiv \sigma_S/\dot{\gamma}$, respectively. Fig. 2.10 shows (a) elongational and (b) shear viscosities using the stresses $\sigma_{E/S}$. From the comparison of Fig. 2.10 with Fig. 2.6 (b) and Fig. 2.8 (b), we find that the decoupling approximation can quantitatively reproduce the behavior of steady-state viscosities. Moreover, we can conclude that the difference in steady-state viscosities between the cases with and without SORF mainly arises from the reduction of the chain stretch λ^2 shown in Figs. 2.7 (a) and 2.9 (a).

In addition to the entangled linear PS melts mentioned above, we have investigated

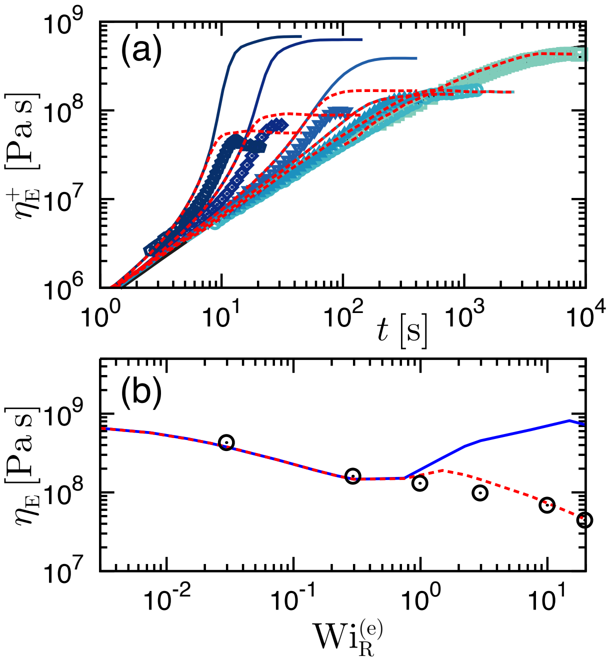

Fig. 2.11: (a) Transient uniaxial elongational viscosities and (b) steady-state uniaxial elongational viscosities for a star polymer melt (PS90K-Star) at 130°C. Dashed (red) and solid (blue) lines indicate the SL simulation results with and without the stretch/orientation-induced reduction of friction, respectively. In (a), the strain rates are 0.2, 0.1, 0.03, 0.01, 0.003, and 0.0003 s^{-1} from left to right, and the bold solid line is the linear viscosity growth function $3\eta_0^+(t)$ calculated from the linear viscoelasticity data. The experimental data for (a) and (b) from Ref. [157] are shown with symbols.

the uniaxial elongational viscosity of an entangled symmetric star PS melt (corresponding to PS90K-Star) [157] and an entangled linear PI melt (corresponding to PI145K) [158] to examine the universality of the effect of SORF on the DT model. For the symmetric star melt, the reptation motion (Eqs. (2.3) and (2.4)) can be considered to be highly suppressed and is therefore not taken into account. Here, we assume that the simulation is independent of the number of arms per star polymer. Moreover, we set the Rouse time as $\tau_\mathrm{R}^{(\mathrm{star})} = 4Z_0^2\tau_\mathrm{e}$. Fig. 2.11 shows (a) the transient uniaxial elongational viscosities $\eta_\mathrm{E}^+(t)$ plotted against time t for various elongational strain rates and (b) the steady-state uniaxial elongational viscosities η_E against Weissenberg numbers defined as $\mathrm{Wi}_\mathrm{R}^{(e)} \equiv \dot{\epsilon}\tau_\mathrm{R}^{(\mathrm{star})}$ for the symmetric star PS melt with three arms (for the linear viscoelasticity of the star PS melt, see Appendix 2.B). Dashed (red) and solid (blue) lines represent the SL simulation results with and without SORF,

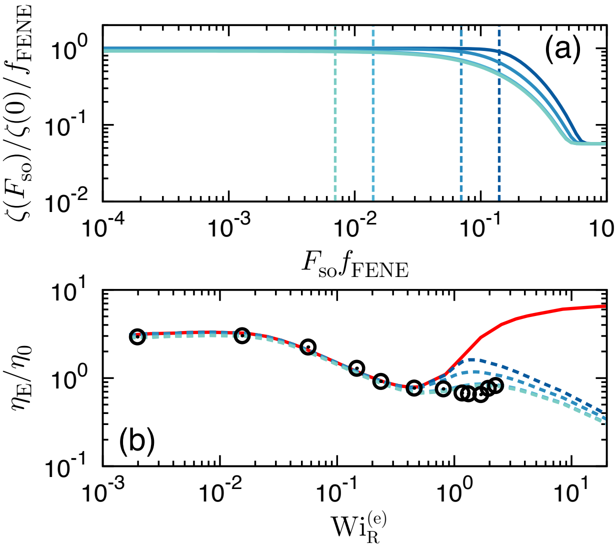

Fig. 2.12: Effect of the parameter $F'^{*}_{\mathrm{s/o}}$ in Eq. (2.7) on (a) $\zeta(F_{\mathrm{so}})$ and (b) Trouton ratio, η_{E}/η_0, for a PI145K melt. In (a), vertical lines show $F'^{*}_{\mathrm{s/o}} = 0.007$, 0.014, 0.07, and 0.14 from left to right. In (b), steady uniaxial elongational viscosities without SORF are shown by the red solid line and those with SORF are shown by bluish dashed lines for $F'^{*}_{\mathrm{s/o}} = 0.14$, 0.07, 0.014, and 0.007, from top to bottom. The experimental data for (b) from Ref. [158] are shown with symbols.

respectively. The parameters of SORF are the same as those used for entangled linear PS melts. From Fig. 2.11, SORF can also improve the agreement with the rheological data of the symmetric star PS melt [157] in the DT model. For the PI melt, we set the maximum stretch ratio as $\lambda_{\mathrm{max}} = 5.9$ [158]. As shown in Fig. 2.12, the SL simulation results with SORF having the same parameters as those of PS melts are close to the experimental data compared with the results without SORF. For the PI melt, because the SL simulation result with SORF having the same parameters as the PS melts still deviates from the experimental data, we have tested for the effect of a change in $F'^{*}_{\mathrm{s/o}}$, which determines the onset of the SORF effect. As shown in Fig. 2.12 (b), the SL simulation results with SORF having smaller $F'^{*}_{\mathrm{s/o}}$ are in good agreement with experimental data. However, to examine the effect of the parameters in detail, further experiments for various molecular weights are needed. From Figs. 2.11 and 2.12, we can draw the following two conclusions. First, SORF is effective for star PS melts, linear PS and PI melts. Second, the parameters are not universal in terms

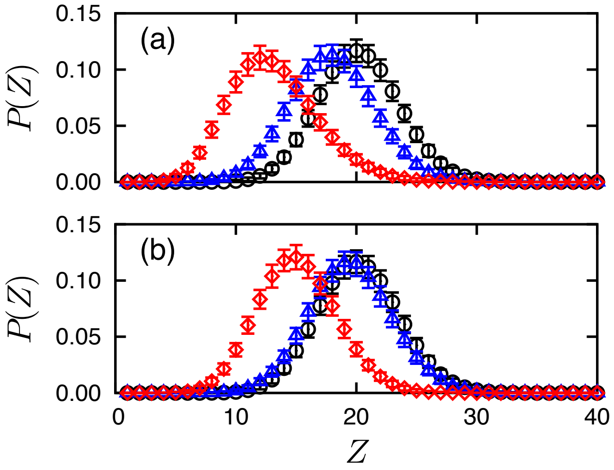

Fig. 2.13: The probability distribution of the number of slip links per chain $P(Z)$ for (a) steady elongational flows and (b) steady shear flows. The blue triangles indicate $P(Z)$ for $\mathrm{Wi}_{\mathrm{d}}^{(\mathrm{e/s})} \simeq 2.1$ ($\mathrm{Wi}_{\mathrm{R}}^{(\mathrm{e/s})} \simeq 3.6 \times 10^{-2}$), the red diamonds indicate $P(Z)$ for $\mathrm{Wi}_{\mathrm{d}}^{(\mathrm{e/s})} \simeq 21$ ($\mathrm{Wi}_{\mathrm{R}}^{(\mathrm{e/s})} \simeq 0.36$), and the black circles indicate $P(Z)$ at equilibrium.

of the chemical structure. In addition, for a poly(n-butyl acrylate) melt with flexible side chains, the SL simulation without SORF achieves better agreement with the experimental data, as discussed in the literature [151]. Further tests to clarify the universality and origin of SORF are needed from both experiments and less-corse-grained simulations.

Next, we would like to discuss the statistical properties of the microscopic structure obtained from the SL simulation under flows. Note that all of the results shown below are the results with SORF. As discussed in a previous paragraph, because the validity of the microscopic structure obtained from the DT model at the strain rate region $\mathrm{Wi}_{\mathrm{R}}^{(\mathrm{e/s})} \gtrsim 1$ has not yet been confirmed, we focus on the statistical properties of the microscopic structure mainly for the strain rate region $\tau_{\mathrm{d}}^{-1} < \dot{\gamma} < \tau_{\mathrm{R}}^{-1}$. Fig. 2.13 shows the probability distribution of the number of slip links per chain under flows for (a) steady elongational flows and (b) steady shear flows. The blue triangles indicate $P(Z)$ for $\mathrm{Wi}_{\mathrm{d}}^{(\mathrm{e/s})} \simeq 2.1$, and the red diamonds indicate $P(Z)$ for $\mathrm{Wi}_{\mathrm{d}}^{(\mathrm{e/s})} \simeq 21$. As shown in Figs. 2.13 (a) and (b), the shapes of $P(Z)$ under flows are almost identical to that at equilibrium. The average values of the distributions in this strain rate region decrease as the strain rates increase, as shown in Fig. 2.7 (c) and Fig. 2.9 (c).

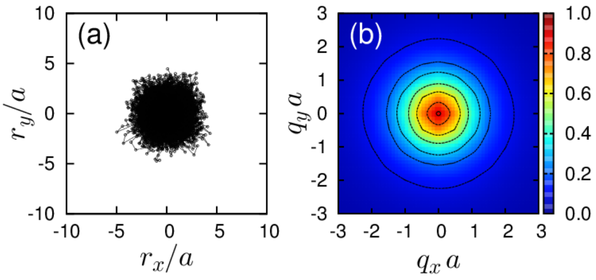

Fig. 2.14: (a) Snapshot of the superimposed conformation of all the polymer chains and (b) static structure factor $S(\boldsymbol{q})$ for a polymer chain at equilibrium obtained from the DT model. The contour lines correspond to values of 0.1, 0.2, 0.3, 0.45, 0.6, 0.75 and 0.9.

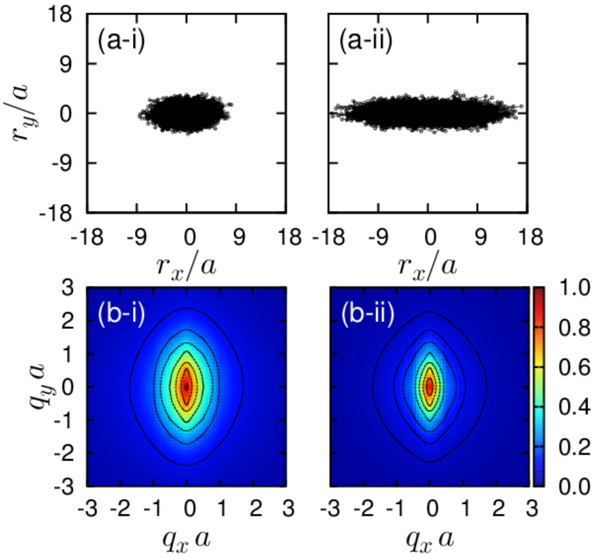

Fig. 2.15: (a) Snapshots of the superimposed conformation of all the polymer chains and (b) static structure factor obtained from the DT model under steady elongational flows for (i) $\mathrm{Wi}_{\mathrm{d}}^{(\mathrm{e})} \simeq 2.1$ ($\mathrm{Wi}_{\mathrm{R}}^{(\mathrm{e})} \simeq 3.6 \times 10^{-2}$) and (ii) $\mathrm{Wi}_{\mathrm{d}}^{(\mathrm{e})} \simeq 21$ ($\mathrm{Wi}_{\mathrm{R}}^{(\mathrm{e})} \simeq 0.36$). The contour lines correspond to values of 0.1, 0.2, 0.3, 0.45, 0.6, 0.75 and 0.9 in (b-i) and 0.05, 0.1, 0.15, 0.3, 0.45, 0.6 and 0.75 in (b-ii).

Figs. 2.14, 2.15 and 2.16 show (a) snapshots of the superimposed conformation of all the polymer chains by fixing the center of mass of each polymer chain to be the origin and (b) the static structure factor $S(\boldsymbol{q})/N$ at equilibrium $\boldsymbol{\kappa} = \boldsymbol{0}$, under uniaxial elongational flows with $\kappa_{xx} > 0$ and $\kappa_{yy} = \kappa_{zz} = -\kappa_{xx}/2$ and shear flows $\kappa_{xy} > 0$, respectively (we show $S(\boldsymbol{q})/N$ because the maximum value of $S(\boldsymbol{q})/N$ is unity). Here, $S(\boldsymbol{q})$ is calculated from the following

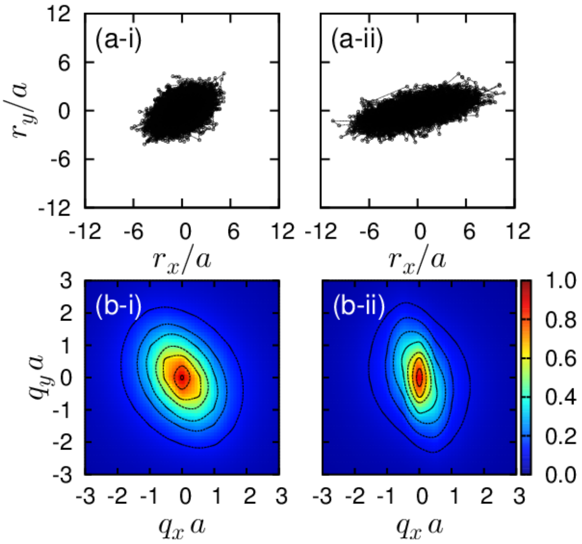

Fig. 2.16: (a) Snapshots of the superimposed conformation of all the polymer chains and (b) static structure factor obtained from the DT model under steady shear flows for (i) $\mathrm{Wi}_{\mathrm{d}}^{(\mathrm{s})} \simeq 2.1$ ($\mathrm{Wi}_{\mathrm{R}}^{(\mathrm{s})} \simeq 3.6 \times 10^{-2}$) and (ii) $\mathrm{Wi}_{\mathrm{d}}^{(\mathrm{s})} \simeq 21$ ($\mathrm{Wi}_{\mathrm{R}}^{(\mathrm{s})} \simeq 0.36$). The contour lines correspond to values of 0.12, 0.21, 0.3, 0.45, 0.6, 0.75 and 0.9 in (b-i) and 0.09, 0.15, 0.24, 0.36, 0.5, 0.65 and 0.8 in (b-ii).

equation:

$$S(\boldsymbol{q}) = \frac{1}{N}\sum_{n,m}^{Z}\left\langle \int_0^{M_n} ds \int_0^{M_m} ds' \exp\Big[-i\boldsymbol{q}\cdot\{\boldsymbol{r}(n,s)-\boldsymbol{r}(m,s')\}\Big]\right\rangle. \tag{2.13}$$

Here, N is the number of all segments per polymer chain, $\boldsymbol{r}(n,s)$ is the position of the s-th segment existing between the n-th and $(n+1)$-th slip links, and M_n is the number of segments between them (for more details, see Appendix 2.C). In Figs. 2.14, 2.15 and 2.16, $S(\boldsymbol{q})$ is obtained by taking ensemble averages of $N_{\mathrm{p}} = 1000$ chains. As shown in Fig. 2.13, both the conformation of polymer chains and the static structure factor at equilibrium are isotropic. As shown in Figs. 2.15 and 2.16, polymer chains are clearly oriented to the direction that is determined by flow types. Furthermore, we can observe that the shapes of $S(\boldsymbol{q})$ are determined by the strain rates. This information will be the stepping stone for comparing the microscopic structure obtained from SL simulations with scattering experiments.

Finally, we calculate the number distribution of entanglements along a polymer chain

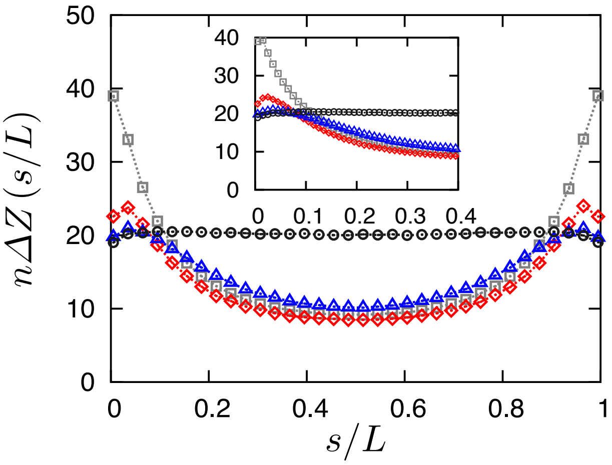

Fig. 2.17: The number distribution of entanglements along a polymer chain for $\mathrm{Wi}_\mathrm{R}^{(\mathrm{e})} = 0$ (black circles), $\mathrm{Wi}_\mathrm{R}^{(\mathrm{e})} \simeq 0.11$ (blue triangles), $\mathrm{Wi}_\mathrm{R}^{(\mathrm{e})} \simeq 0.36$ (red diamonds) and $\mathrm{Wi}_\mathrm{R}^{(\mathrm{e})} \simeq 1.1$ (gray squares). The results obtained by using a discretized number larger than that in the main figure are shown in the inset.

defined as $p_Z(\dot\gamma, s) = n\langle \Delta Z(\dot\gamma, s; s < s < s + \Delta s)\rangle$. Here, s $(0 \le s \le L)$ is the internal coordinate along the polymer chain, L is the contour length of the polymer chain, Δs is the interval length defined as $\Delta s \equiv L/n$, and n is the division number (here, we employ $n = 100$). By definition, $p_Z(\dot\gamma, s)$ satisfies the relation $\int_0^1 p_Z(\dot\gamma, s/L) d(s/L) = \langle Z(\dot\gamma)\rangle$. Fig. 2.17 shows $p_Z(\dot\gamma, s/L)$ for $\mathrm{Wi}_\mathrm{R}^{(\mathrm{e})} = 0$ (black squares), $\mathrm{Wi}_\mathrm{R}^{(\mathrm{e})} \simeq 0.11$ (blue triangles), $\mathrm{Wi}_\mathrm{R}^{(\mathrm{e})} \simeq 0.36$ (red diamonds) and $\mathrm{Wi}_\mathrm{R}^{(\mathrm{e})} \simeq 1.1$ (gray squares). In addition to the strain rate region $\mathrm{Wi}_\mathrm{R}^{(\mathrm{e})} < 1$, to examine a possible origin of increasing $Z/\langle Z\rangle_\mathrm{eq}$ in $\mathrm{Wi}_\mathrm{R}^{(\mathrm{e/s})} \gtrsim 1$ shown in Figs. 2.7 (c) and 2.9 (c), we also show $p_Z(\dot\gamma, s/L)$ for $\mathrm{Wi}_\mathrm{R}^{(\mathrm{e})} \simeq 1.1$. At equilibrium, $p_Z(\dot\gamma = 0, s)$ is almost constant. At the strain rate region $\tau_\mathrm{d}^{-1} < \dot\epsilon < \tau_\mathrm{R}^{-1}$, we can observe that $p_Z(\dot\gamma, s)$ has two peaks near the ends of the polymer chain and decreases mainly in the middle region ($s/L \sim 0.5$). This behavior can be explained by the CCR (convected constraint release) mechanism and is consistent with our previous work [113]. However, as the strain rate increases, the two peaks near the ends of the polymer chain are moved to both ends, as shown in the inset. Moreover, the number distributions of entanglements near both ends are highly enhanced at $\mathrm{Wi}_\mathrm{R}^{(\mathrm{e})} \simeq 1.1$. This leads to the increase in $Z/\langle Z\rangle_\mathrm{eq}$ in the high strain rate region ($\mathrm{Wi}_\mathrm{R}^{(\mathrm{e/s})} \gtrsim 1$), as shown in Fig. 2.7 (c) and Fig. 2.9 (c). This behavior in entanglement structure along a polymer chain suggests that the criterion for creating a new entanglement point in the high strain rate region ($\mathrm{Wi}_{\mathrm{R}}^{(\mathrm{e/s})} \gtrsim 1$) should be modified; that is, the hooking rate might be a function of the orientation and stretch of polymer chains as discussed in the literature [160].

2.4 Conclusions

We have examined the rheological properties and statistical properties of the microscopic structure of well-entangled polymer melts described by the slip-link model proposed by Doi and Takimoto (DT model) [67]. Since we have recognized that the DT model does not well-describe nonlinear rheological behavior for strain rates larger than τ_{R}^{-1}, we have incorporated the concept of the stretch/orientation-induced reduction of friction (SORF), which was originally proposed by Ianniruberto *et al.* [148], with the DT model.

In the linear region, we have confirmed that the rheological behavior obtained by the DT model with and without SORF are almost the same because the effect of SORF works only when polymer chains are highly oriented and stretched. For the statistical properties of the microscopic structure of polymer chains in the linear region, the probability distribution of the number of slip links per polymer chain and the static structure factor are shown. The probability distribution of the number of slip links per polymer chain obtained from the DT model can be fitted by the Gaussian distribution function rather than the theoretically obtained Poisson distribution function. This result shows the same tendency as the result obtained by the PCN model [66]. Moreover, as expected, the static structure factor at equilibrium is almost isotropic.

In the nonlinear region, the effect of SORF is striking, particularly under uniaxial elongational flows. The steady-state elongational viscosities without SORF show thinning behavior for $\tau_{\mathrm{d}}^{-1} \lesssim \dot{\epsilon} \lesssim \tau_{\mathrm{R}}^{-1}$ and thickening behavior for $\dot{\epsilon} \gtrsim \tau_{\mathrm{R}}^{-1}$, which is typical for entangled polymer solutions. However, the steady-state elongational viscosities with SORF show almost monotonic thinning behavior. From the decoupling approximation, we can understand that the major reason for the nonmonotonic behavior comes from not enough reduction of chain stretch under fast flows. Under shear flows, the effect of SORF can be observed in a relatively high strain rate region $\mathrm{Wi}_{\mathrm{R}}^{(\mathrm{s})} \gtrsim 10$. Although SORF can improve the rheological properties obtained by the DT model, note that the validity for employing the assumption that $\tau_{\mathrm{e}}(F_{\mathrm{s/o}})$ can be described using Eq. (2.7) with the original parameters is uncertain for the DT model. For more accurate predictions using the DT model with SORF, it is necessary to obtain a more suitable expression for the friction ζ of the DT model directly by fitting the experimental data of relaxation after cessation of elongational flows [154]. For the microscopic structure in the nonlinear region, we have found that the normalized number of slip links per chain shows nonmonotonic behavior; that is, the normalized number of slip links first decreases with the strain rate for $\tau_{\mathrm{d}}^{-1} \lesssim \dot{\epsilon}, \dot{\gamma} \lesssim \tau_{\mathrm{R}}^{-1}$, which is consistent with the results obtained from the PCN model [64], and then increases for $\dot{\epsilon}, \dot{\gamma} \gtrsim \tau_{\mathrm{R}}^{-1}$.

Judging from the increasing behavior of the steady-state normalized number of slip links per chain under elongational and shear flows in the region $\mathrm{Wi}_{\mathrm{R}}^{(\mathrm{e/s})} \gtrsim 1$, we have concluded that the microscopic structure obtained from the DT model for $\mathrm{Wi}_{\mathrm{R}}^{(\mathrm{e/s})} \gtrsim 1$ is questionable. For a reliable deformation rate region $\mathrm{Wi}_{\mathrm{R}}^{(\mathrm{e/s})} \lesssim 1$, the probability distribution of the number of slip links per chain and the static structure factor are shown. In particular, the static structure factor will be useful when comparing scattering experiments [108, 110]. Finally, we have examined the number distribution of entanglements along a polymer chain. Consequently, we have found that the number distribution of entanglements has peaks near both ends for $\mathrm{Wi}_{\mathrm{R}}^{(\mathrm{e})} \lesssim 1$, and the peaks are highly enhanced and moved to the ends for $\mathrm{Wi}_{\mathrm{R}}^{(\mathrm{e})} \gtrsim 1$. This behavior in the region of $\mathrm{Wi}_{\mathrm{R}}^{(\mathrm{e})} \gtrsim 1$ indicates that the hooking rate of the DT model should be modified to be a function of orientation and stretch of polymer chains in the high strain rate region.

Although room for improvement on the microscopic dynamics of polymer chains for $\mathrm{Wi}_{\mathrm{R}}^{(\mathrm{e/s})} \gtrsim 1$ still exists, the rheological properties obtained by the DT model can be improved using SORF. Incorporating the DT model having the SORF with a macroscopic model, we are able to extend our MSS method to highly nonlinear regions including strain hardening

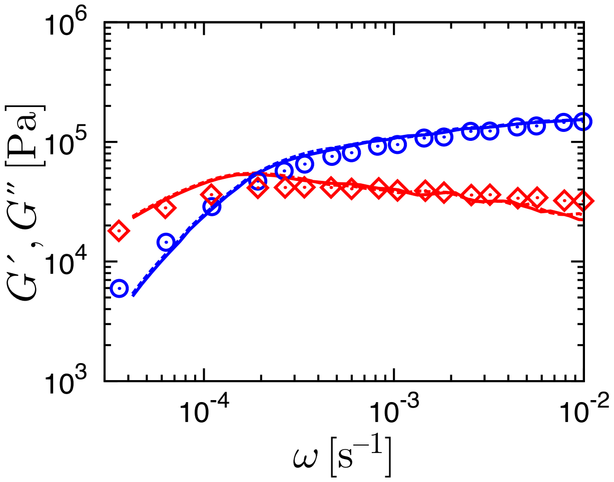

Fig. 2.18: Linear viscoelasticity of PS390K. Circles and diamonds indicate G' and G'' extracted from Ref. [53]. Simulation results with and without SORF are shown by dashed and solid lines, respectively.

under fast elongational flows. This MSS method bring us improved predictions of processing flows, such as a polymer melt spinning process [146], where the elongational strain rate easily reaches a value larger than τ_{R}^{-1}. Nevertheless, further studies from various directions are clearly needed to improve the DT model. For instance, although the DT model can successfully predict rheological properties, the thermodynamical properties of the DT model are not yet fully understood. Furthermore, to examine the rheological properties of more complicated systems, such as entangled branched polymer melts, we should refine the DT model. We are continuing our study on the DT model along these directions, and the results will be reported elsewhere.

Appendix 2.A Rheological Properties of PS390K

SL simulations were performed in the linear and nonlinear viscoelastic ranges for a linear monodisperse PS polymer melt with a molecular weight $M_{\mathrm{w}} = 390$ K ($Z_0 = 37$) (henceforth, it is referred to as PS390K). The parameters for the simulations in Figs. 2.18, 2.20 and 2.21 are the same as those of Figs. 2.2, 2.6 and 2.7, except for the equilibrium number of strands Z_0. Namely, the unit time and stress are the same as those determined in Fig. 2.2. Fig. 2.18

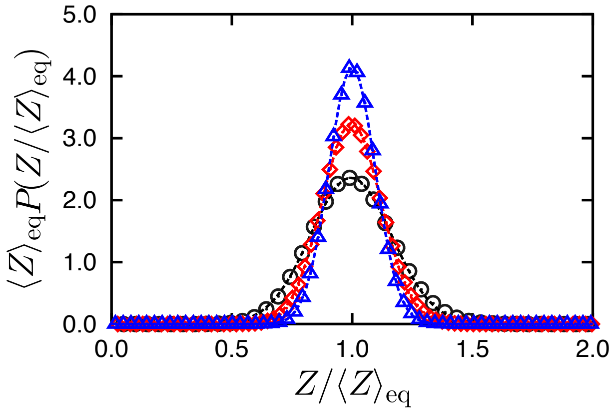

Fig. 2.19: The normalized probability distribution of the number of slip links per chain at equilibrium for $Z_0 = 19$ (black circles), 37 (red diamonds) and 60 (blue triangles). The dashed lines indicate the fitted Gaussian distribution.

shows the linear viscoelasticity data of the polymer melt PS390K ($Z_0 = 37$) calculated from Eqs. (2.11) and (2.12) using the stress relaxation modulus $G(t)$ in Eq. (2.10) after applying step shear strain $\gamma_0 = 0.4$. As shown in Fig. 2.18, the results obtained from the SL simulations are in reasonable agreement with the experimental data [53]. In addition, as is the case with PS200K, there is no difference between the cases with and without SORF in linear viscoelasticity data for PS390K. Fig. 2.19 shows the normalized probability distribution of the number of slip links per chain $\langle Z\rangle_{\mathrm{eq}}P(Z/\langle Z\rangle_{\mathrm{eq}})$ at equilibrium (we have also examined the probability distribution of $Z_0 = 60$ as a reference). The fitted Gaussian distributions are also shown. The variance σ^2 of PS390K ($Z_0 = 37$) is smaller than that of PS200K ($Z_0 = 19$), as shown in Fig. 2.19 ($\sigma^2(Z_0 = 19) = 2.9 \times 10^{-2}$, $\sigma^2(Z_0 = 37) = 1.5 \times 10^{-2}$, and $\sigma^2(Z_0 = 60) = 9.3 \times 10^{-3}$). Fig. 2.20 shows the (a) transient uniaxial viscosities and (b) steady uniaxial elongational viscosities for a PS390K melt at 130°C [53, 155]. The basic behavior is almost the same as that of PS200K; that is, the SL simulations with SORF can capture the rheological properties under fast elongational flows better than the SL simulations without SORF. Fig. 2.21 shows (a) the reduced chain stretch squared λ^2, (b) the average orientation $\bar{S}$, and (c) number of slip links per chain normalized using the equilibrium value $Z/\langle Z\rangle_{\mathrm{eq}}$ under uniaxial elongational flows for PS390K. Furthermore, the results of PCN simulations [64] with and without SORF for PS390K are also shown. As shown in Fig. 2.21,

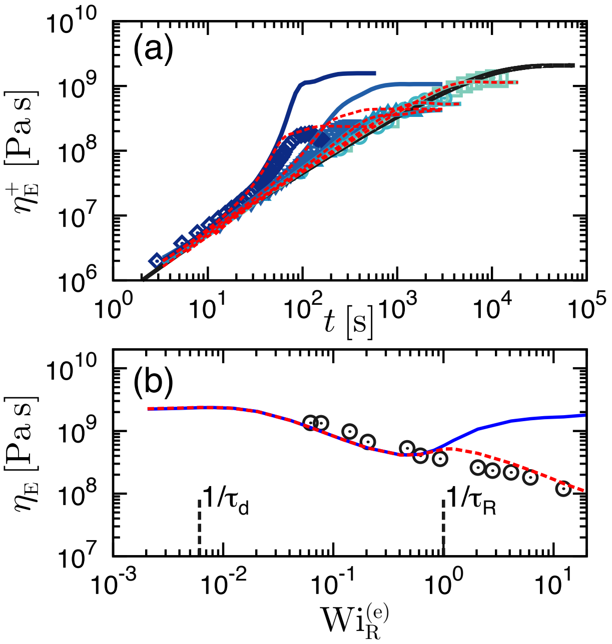

Fig. 2.20: (a) Transient uniaxial viscosities and (b) steady uniaxial elongational viscosities for a monodisperse linear PS melt (PS390K) at 130°C. In (a), the strain rates are 0.03 (diamonds), 0.01 (reverse triangles), 0.003 (triangles), 0.001 (circles) and 0.0003 (squares) s^{-1} from left to right, and the bold solid line is the linear viscosity growth function $3\eta_0^+(t)$ calculated from the linear viscoelasticity data. The experimental data for (a) and (b) from Refs. [53] and [155] are shown with symbols, respectively. Dashed and solid lines indicate the SL simulation results with and without SORF, respectively.

the tendencies of these values are almost identical to those of PS200K. As shown in Figs. 2.21 (a) and (b), the values of λ^2 and $\bar{S}$ are in qualitative agreement with those of the PCN simulations. Because of the degree of coarse-graining, the values obtained from these models are slightly different. Although the values of $Z/\langle Z\rangle_{\mathrm{eq}}$ for the strain rate region $\tau_{\mathrm{d}}^{-1} \lesssim \dot{\epsilon} \lesssim \tau_{\mathrm{R}}^{-1}$ are in reasonable agreement with those of the PCN simulations, the values of $Z/\langle Z\rangle_{\mathrm{eq}}$ for the strain rate region $\dot{\epsilon} > \tau_{\mathrm{R}}^{-1}$ are clearly larger than those of the PCN simulations. As discussed in Fig. 2.17, this difference is presumably because entanglement near the ends, which contributes less to the stress than in the middle region, increases for the strain rate $\dot{\epsilon} > \tau_{\mathrm{R}}^{-1}$. Since the number of entanglements cannot be measured by present experiments, the validity of the microscopic structure including the number of entanglements for the strain rate region $\dot{\epsilon} > \tau_{\mathrm{R}}^{-1}$ should be carefully examined by comparing with less-coarse-grained models.

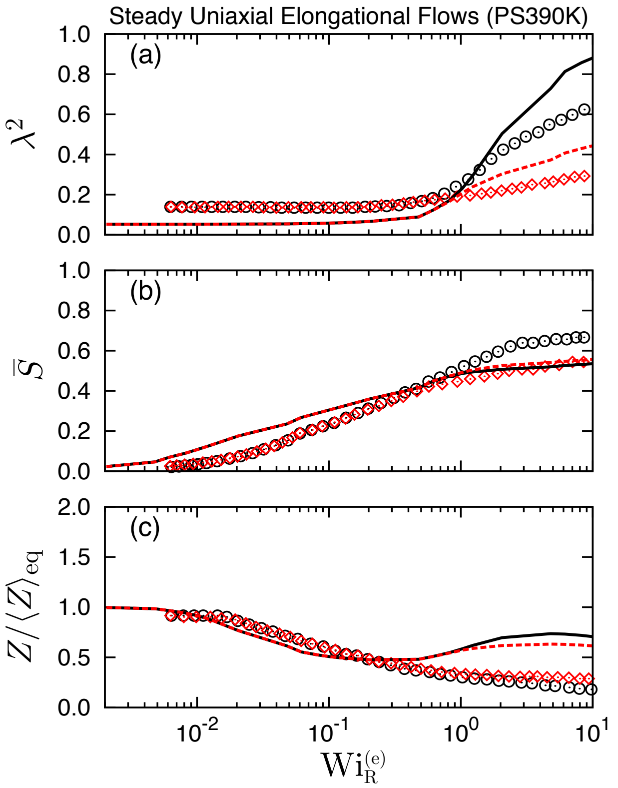

Fig. 2.21: (a) The reduced chain stretch squared λ^2, (b) the average orientation $\bar{S}$ and (c) the number of slip links per chain normalized using the equilibrium value $Z/\langle Z\rangle_{\mathrm{eq}}$ under uniaxial elongational flows for PS390K. These values are plotted against the Rouse-relaxation-time-based Weissenberg number $\mathrm{Wi}_{\mathrm{R}}^{(\mathrm{e})} \equiv \dot{\epsilon}\tau_{\mathrm{R}}$. The simulation results with and without SORF are indicated with the dashed and solid lines, respectively. The diamonds correspond to the PCN simulation with SORF, and the circles correspond to the PCN simulation without SORF extracted from Ref. [64].

However, we have concluded that the DT model for the strain rate region $\dot{\epsilon} > \tau_{\mathrm{R}}^{-1}$ has been improved by incorporating SORF because the prediction of stress σ_{E} that can be measured by experiments is correctly captured.

Appendix 2.B Linear Viscoelasticity of the Star Polymer Melt

SL simulations were performed for a symmetric star PS melt having three arms with an arm molecular weight $M_{\mathrm{w}} = 92.4$ K ($Z_0^{(\mathrm{star})} = 9$) [157]. Fig. 2.22 shows the linear viscoelasticity data of the star polymer melt ($Z_0^{(\mathrm{star})} = 9$) calculated from Eqs. (2.11) and (2.12) using the stress relaxation modulus $G(t)$ in Eq. (2.10) after applying step shear strain $\gamma_0 = 0.4$. The

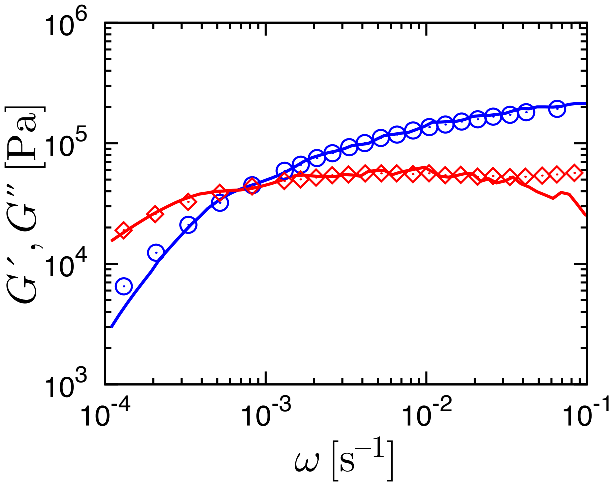

Fig. 2.22: Linear viscoelasticity of the star polymer melt. Circles and diamonds indicate G' and G'' extracted from Ref. [157].

unit time $\tau_{\mathrm{e}}^{(\mathrm{star})}(0)$ and the unit stress $\sigma_{\mathrm{e}}^{(\mathrm{star})}$ can be determined through comparison with the experimental data [157] as $\tau_{\mathrm{e}}^{(\mathrm{star})}(0) = 0.23$ s and $\sigma_{\mathrm{e}}^{(\mathrm{star})} = 0.84$ MPa for the star PS melt.

Appendix 2.C Derivation of Structure Factor

In the DT model, a polymer chain is composed of $(Z-1)$ entangled strands and two ends (head and tail), as shown in Fig. 2.23 (a). The strands depicted with black lines in Fig. 2.23 (a) are referred to as entangled strands. Namely, the polymer chain has $(Z+1)$ strands whose lengths are ℓ_i $(0 \le n \le Z)$. To derive the expression for the structure factor $S(\boldsymbol{q})$ of a well-entangled polymer chain from the slip link positions obtained by the DT model, we assume that entangled strands and the head and tail are Gaussian chains with two and one fixed ends, respectively, as shown in Fig. 2.23 (b). Here, the Gaussian chain of a strand n consists of M_n segments having equal length b. Since we assume the Gaussian chain, M_n can be evaluated as $M_n \simeq \ell_n^2/b^2$, and the Green function of the Gaussian chain with a length sb whose two ends are located at $\boldsymbol{r}$ and $\boldsymbol{r}'$, $G_s[\boldsymbol{r}, \boldsymbol{r}']$, is defined as [21]

$$G_s[\boldsymbol{r}, \boldsymbol{r}'] = \left(\frac{3}{2\pi s b^2}\right)^{3/2} \exp\left[-\frac{3}{2sb^2}\left(\boldsymbol{r}-\boldsymbol{r}'\right)^2\right]. \tag{2.14}$$

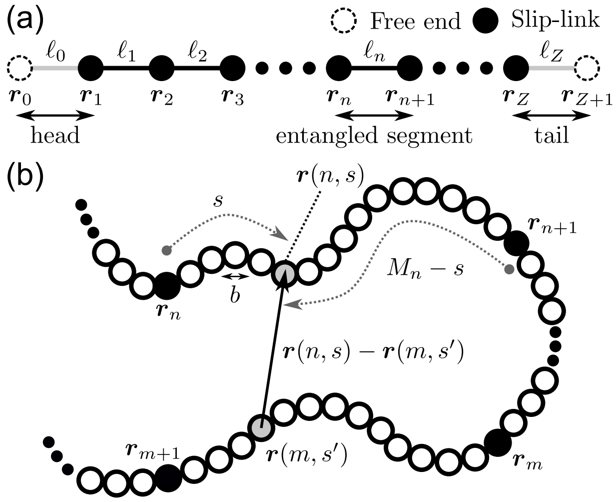

Fig. 2.23: (a) Schematic illustration of a polymer chain considered in the DT model and (b) schematic illustration of a well-entangled polymer chain to evaluate the structure factor $S(\boldsymbol{q})$.

From the assumption mentioned above, the structure factor $S(\boldsymbol{q})$ can be described as

$$NS(\boldsymbol{q}) = \sum_{n=0}^{Z}\sum_{m=0}^{Z}\left\langle \int_0^{M_n} ds \int_0^{M_m} ds' \exp\Big[-i\boldsymbol{q}\cdot\{\boldsymbol{r}(n,s)-\boldsymbol{r}(m,s')\}\Big]\right\rangle \tag{2.15}$$

$$\begin{aligned}
&= \sum_{n=0}^{Z}\int_0^{M_n} ds \int_0^{M_n} ds' \left\langle \exp\Big[-i\boldsymbol{q}\cdot\{\boldsymbol{r}(n,s)-\boldsymbol{r}(n,s')\}\Big]\right\rangle \left(\delta_{n,0}+\delta_{n,Z}+\bar{\delta}_{n,(0,Z)}\right) \\
&+ \sum_{n=0}^{Z}\sum_{m=0}^{Z}\int_0^{M_n} ds \int_0^{M_m} ds' \left\langle \exp\Big[-i\boldsymbol{q}\cdot\{\boldsymbol{r}(n,s)-\boldsymbol{r}(m,s')\}\Big]\right\rangle \\
&\times \Big\{\delta_{n,0}\delta_{m,Z}+\delta_{n,Z}\delta_{m,0}+\left(\delta_{n,0}\bar{\delta}_{m,(0,Z)}+\delta_{n,Z}\bar{\delta}_{m,(0,Z)}+\bar{\delta}_{n,(0,Z)}\delta_{m,0}+\bar{\delta}_{n,(0,Z)}\delta_{m,Z}\right) \\
&+ \bar{\delta}_{n,(0,Z)}\bar{\delta}_{m,(0,Z)}\Big\} \\
&\equiv \left(F_0+F_Z+\sum_{n=1}^{Z-1}F_n\right)+\Bigg\{P_0^-P_Z^+ + P_0^+P_Z^- \\
&+ \sum_{n=1}^{Z-1}\left(P_0^-P_n^+ + P_Z^-P_n^+ + P_0^+P_n^- + P_Z^+P_n^-\right)+\sum_{n=1}^{Z-1}\sum_{m=1}^{Z-1}\bar{\delta}_{n,m}P_n^-P_m^+\Bigg\},
\end{aligned} \tag{2.16}$$

where $N \equiv \sum_{n=0}^{Z} M_n$ is the number of all segments, $\delta_{n,m}$ is the delta function, and $\bar{\delta}_{n,m}$ is the inverse of the delta function defined as $\bar{\delta}_{n,m} = 1-\delta_{n,m}$. The first terms in Eq. (2.16) are the contribution from $n = m$, namely, a correlation between two segments in the head F_0, the tail F_Z and an entangled segment F_n $(1 \leq n \leq Z-1)$. The second terms in Eq. (2.16) are the contribution from $n \neq m$, namely, a correlation between two segments in the different strands. Here, $P_0^{\pm}$ stands for the contribution from the head, $P_Z^{\pm}$ is the contribution from the tail, and $P_n^{\pm}$ $(1 \leq n \leq Z-1)$ is the contribution from entangled segments. The first two contributions in the second terms are correlations between the segments in the head and tail, the terms from the third to sixth stand for the correlations between segments in the head or tail and an entangled strand, and the last contribution in the second terms is the correlation between segments in different entangled strands. The first terms in Eq. (2.16) can be written as

$$
\begin{aligned}
F_0 \equiv{}& \int_0^{M_0} ds \int_0^{M_0} ds' \left\langle \exp\Big[-i\boldsymbol{q}\cdot\{\boldsymbol{r}(0,s)-\boldsymbol{r}(0,s')\}\Big]\right\rangle \\
={}& \frac{1}{N_0^{(1)}}\Bigg(\int_0^{M_0} ds' \int_0^{s'} ds \int d\boldsymbol{r}_0 \int d\boldsymbol{r}(0,s) \int d\boldsymbol{r}(0,s') \\
&\times G_s[\boldsymbol{r}_0,\boldsymbol{r}(0,s)]G_{s'-s}[\boldsymbol{r}(0,s'),\boldsymbol{r}(0,s)]G_{M_0-s'}[\boldsymbol{r}(0,s'),\boldsymbol{r}_1] \\
&+\int_0^{M_0} ds \int_0^{s} ds' \int d\boldsymbol{r}_0 \int d\boldsymbol{r}(0,s) \int d\boldsymbol{r}(0,s') \\
&\times G_{s'}[\boldsymbol{r}_0,\boldsymbol{r}(0,s')]G_{s-s'}[\boldsymbol{r}(0,s'),\boldsymbol{r}(0,s)]G_{M_0-s}[\boldsymbol{r}(0,s),\boldsymbol{r}_1]\Bigg) \exp\Big[-i\boldsymbol{q}\cdot\{\boldsymbol{r}(0,s)-\boldsymbol{r}(0,s')\}\Big] \\
={}& M_0^2 f(K_0), \qquad (2.17)
\end{aligned}
$$

$$
\begin{aligned}
F_Z \equiv{}& \int_0^{M_Z} ds \int_0^{M_Z} ds' \left\langle \exp\Big[-i\boldsymbol{q}\cdot\{\boldsymbol{r}(Z,s)-\boldsymbol{r}(Z,s')\}\Big]\right\rangle \\
={}& \frac{1}{N_Z^{(1)}}\Bigg(\int_0^{M_Z} ds' \int_0^{s'} ds \int d\boldsymbol{r}_{Z+1} \int d\boldsymbol{r}(Z,s) \int d\boldsymbol{r}(Z,s') \\
&\times G_s[\boldsymbol{r}_{Z+1},\boldsymbol{r}(Z,s)]G_{s'-s}[\boldsymbol{r}(Z,s),\boldsymbol{r}(Z,s')]G_{M_Z-s'}[\boldsymbol{r}(Z,s'),\boldsymbol{r}_Z] \\
&+\int_0^{M_Z} ds \int_0^{s} ds' \int d\boldsymbol{r}_{Z+1} \int d\boldsymbol{r}(Z,s) \int d\boldsymbol{r}(Z,s') \\
&\times G_{s'}[\boldsymbol{r}_{Z+1},\boldsymbol{r}(Z,s')]G_{s-s'}[\boldsymbol{r}(Z,s'),\boldsymbol{r}(Z,s)]G_{M_Z-s}[\boldsymbol{r}(Z,s),\boldsymbol{r}_Z]\Bigg) \\
&\times \exp\Big[-i\boldsymbol{q}\cdot\{\boldsymbol{r}(Z,s)-\boldsymbol{r}(Z,s')\}\Big] = M_Z^2 f(K_Z), \qquad (2.18)
\end{aligned}
$$

and

$$
\begin{aligned}
F_n \equiv & \int_0^{M_n} ds \int_0^{M_n} ds' \left\langle \exp\Big[-i\boldsymbol{q}\cdot\{\boldsymbol{r}(n,s)-\boldsymbol{r}(n,s')\}\Big]\right\rangle \\
= & \frac{1}{N_n^{(1)}}\Bigg(\int_0^{M_n} ds' \int_0^{s'} ds \int d\boldsymbol{r}(n,s) \int d\boldsymbol{r}(n,s') \\
& \times G_s[\boldsymbol{r}_n, \boldsymbol{r}(n,s)] G_{s'-s}[\boldsymbol{r}(n,s), \boldsymbol{r}(n,s')] G_{M_n-s'}[\boldsymbol{r}(n,s'), \boldsymbol{r}_{n+1}] \\
& + \int_0^{M_n} ds \int_0^{s} ds' \int d\boldsymbol{r}(n,s) \int d\boldsymbol{r}(n,s') \\
& \times G_{s'}[\boldsymbol{r}_n, \boldsymbol{r}(n,s')] G_{s-s'}[\boldsymbol{r}(n,s'), \boldsymbol{r}(n,s)] G_{M_n-s}[\boldsymbol{r}(n,s), \boldsymbol{r}_{n+1}]\Bigg) \\
& \times \exp\Big[-i\boldsymbol{q}\cdot\{\boldsymbol{r}(n,s)-\boldsymbol{r}(n,s')\}\Big] \\
= & \pi^{1/2}\frac{M_n^2}{K_n^2}\mathrm{Re}\Big[\mathrm{e}^{(z_1^-)^2} z_2^- \left\{\mathrm{erf}\left(z_1^-\right)-\mathrm{erf}\left(z_2^-\right)\right\} + \Big(1-\mathrm{e}^{(z_1^-)^2-(z_2^-)^2}\Big)\Big],
\end{aligned}
\tag{2.19}
$$

where $N_0^{(1)}$, $N_Z^{(1)}$ and $N_n^{(1)}$ are the normalization constants, K_n depends on $\boldsymbol{q}$ as $K_n \equiv (M_n b^2 \boldsymbol{q}^2/6)^{1/2}$, $f(x)$ is the Debye function defined as

$$
f(x) = \frac{2}{x^4}\left(\mathrm{e}^{-x^2} + x^2 - 1\right), \tag{2.20}
$$

z_1^- and z_2^- are complex numbers defined later in Eq. (2.25), and $\mathrm{erf}(z)$ is the error function described as

$$
\mathrm{erf}(z) = \frac{2}{\sqrt{\pi}}\int_0^z \mathrm{e}^{-t^2} dt. \tag{2.21}
$$

Moreover, by use of the Green function of the Gaussian chain, the second terms in Eq. (2.16) can be written as

$$\begin{aligned}
P_0^{\pm} &= \int_0^{M_0} ds \left\langle \mathrm{e}^{\pm i\boldsymbol{q}\cdot\boldsymbol{r}(0,s)} \right\rangle \\
&= \frac{1}{N_0^{(2)}} \int_0^{M_0} ds \int d\boldsymbol{r}_0 \int d\boldsymbol{r}(0,s) G_s[\boldsymbol{r}_0, \boldsymbol{r}(0,s)] G_{M_0-s}[\boldsymbol{r}(0,s), \boldsymbol{r}_1] \mathrm{e}^{\pm i\boldsymbol{q}\cdot\boldsymbol{r}(0,s)} \\
&= \frac{M_0}{K_0^2} \mathrm{e}^{\pm i\boldsymbol{q}\cdot\boldsymbol{r}_1} \left(1 - \mathrm{e}^{-K_0^2}\right), \qquad (2.22) \\
P_Z^{\pm} &= \int_0^{M_Z} ds \left\langle \mathrm{e}^{\pm i\boldsymbol{q}\cdot\boldsymbol{r}(Z,s)} \right\rangle \\
&= \frac{1}{N_Z^{(2)}} \int_0^{M_Z} ds \int d\boldsymbol{r}_{Z+1} \int d\boldsymbol{r}(Z,s) G_s[\boldsymbol{r}_{Z+1}, \boldsymbol{r}(Z,s)] G_{M_Z-s}[\boldsymbol{r}(Z,s), \boldsymbol{r}_Z] \mathrm{e}^{\pm i\boldsymbol{q}\cdot\boldsymbol{r}(Z,s)} \\
&= \frac{M_Z}{K_Z^2} \mathrm{e}^{\pm i\boldsymbol{q}\cdot\boldsymbol{r}_Z} \left(1 - \mathrm{e}^{-K_Z^2}\right), \qquad (2.23)
\end{aligned}$$

and

$$\begin{aligned}
P_n^{\pm} &= \int_0^{M_n} ds \left\langle \mathrm{e}^{\pm i\boldsymbol{q}\cdot\boldsymbol{r}(n,s)} \right\rangle \\
&= \frac{1}{N_n^{(2)}} \int_0^{M_n} ds \int d\boldsymbol{r}(n,s) G_s[\boldsymbol{r}_n, \boldsymbol{r}(n,s)] G_{M_n-s}[\boldsymbol{r}(n,s), \boldsymbol{r}_{n+1}] \mathrm{e}^{\pm i\boldsymbol{q}\cdot\boldsymbol{r}(n,s)} \\
&= i\sqrt{\pi} \frac{M_n}{2K_n} \mathrm{e}^{(z_1^{\mp})^2 \pm i\boldsymbol{q}\cdot\boldsymbol{r}_n} \left\{ \mathrm{erf}\left(z_1^{\mp}\right) - \mathrm{erf}\left(z_2^{\mp}\right) \right\} \qquad (2.24)
\end{aligned}$$

with

$$\left\{ \begin{aligned}
z_1^{\pm} &= \pm \frac{\boldsymbol{q}\cdot(\boldsymbol{r}_{n+1} - \boldsymbol{r}_n)}{2K_n} - i\frac{K_n}{2}, \\
z_2^{\pm} &= \pm \frac{\boldsymbol{q}\cdot(\boldsymbol{r}_{n+1} - \boldsymbol{r}_n)}{2K_n} + i\frac{K_n}{2},
\end{aligned} \right. \qquad (2.25)$$

where $N_0^{(2)}$, $N_Z^{(2)}$ and $N_n^{(2)}$ are the normalization constants. The normalization constants $N_0^{(1)}$, $N_Z^{(1)}$, $N_n^{(1)}$, $N_0^{(2)}$, $N_Z^{(2)}$, and $N_n^{(2)}$ are defined such that the second equations of Eqs. (2.17), (2.18), (2.19), (2.22), (2.23), and (2.24) turn out to be unity when $\boldsymbol{q} = \boldsymbol{0}$. Note that a large proportion ($> 80\%$) of the contribution to $S(\boldsymbol{q})$ comes from the correlation between segments in entangled strands. In our numerical simulations, we choose the equilibrium length between adjacent slip links a as unit length. Moreover, to avoid numerical instability when calculating $S(\boldsymbol{q})$, we ignore contributions from strands consisting of small number of segments.

3 Multi-Scale Simulations for Entangled Polymer Melt Spinning Process

3.1 Introduction

In this chapter, we focus specifically on a polymer melt spinning process, which is a common process for manufacturing polymeric fibers. This process is important from both industrial and scientific aspects for the following reasons [161]: Industrially, an ideal process for manufacturing polymeric fibers should be simple, effective and stable. Therefore, it is important to stably operate this simple process and produce strong fibers with high degree of polymer chain orientation and crystallinity. Scientifically, research interests include the relation between microscopic polymer chain structure induced by an elongational flow and physical properties of the resultant fiber. From this point of view, there are many experimental and numerical studies on the polymer melt spinning process.

To the best of our knowledge, from a simulation perspective, a phenomenological constitutive equation is used to couple the strain rate with the polymeric stress in all of the studies on the polymer melt spinning process. However, it is often difficult to uniquely choose an appropriate constitutive equation and obtain a parameter set that fits the experiments on targeting polymer melt because there is no definite method for choosing a proper constitutive equation from among the known ones. Moreover, to use the constitutive equation prohibits one from directly obtaining microscopic information that is tightly related to the macroscopic flow and physical properties of the resultant product. In fact, to develop well-controlled polymeric products, it is significantly important to know the correlation between the macroscopic flow behavior and the state of polymer chains at a local place. One of the reliable methods to obtain microscopic information is a molecular dynamics (MD) simulation. However, despite the recent rapid development of computational ability, it is still difficult to solve flow problems of polymeric liquids by using solely the MD simulation because of its high computational cost. To overcome these difficulties, increasing attention has been paid to a multi-scale approach that directly combines the macroscopic model with the microscopic model.

The authors developed a multi-scale simulation method for the spinning process by using the particle-based Lagrangian method and the dumbbell model recently [145]. However, realistic polymer melts used in the spinning process are more complex due, for example, to the effect of entanglements. Entangled polymer melts are used to enhance the strength of the product in industrial cases. Based on the current situation mentioned above, the aim of this chapter is to establish a multi-scale simulation method for the spinning process of well-entangled polymer melts. In the present chapter, we therefore employ a more complex microscopic polymer model that can describe well-entangled polymer melts called the slip-link model proposed by Doi and Takimoto [67], and analyze the spinning process from both the macroscopic and microscopic viewpoints.

3.2 Model of Entangled Polymer Melt Spinning

3.2.1 Macroscopic Model

In the multi-scale simulation of the polymer melt spinning process, we must connect the macroscopic flow behavior of the filament and the microscopic molecular motions. A schematic view of the polymer melt spinning process considered in this study is shown in Fig.3.1. Here we briefly explain macroscopic equations; see our previous study for details [145]. To set up the macroscopic equations, we made the following assumptions.

(i) The shape of the filament is axi-symmetric.

(ii) The polymer chains are relaxed at the location where the diameter of the filament shows a maximum due to the die swelling effect.

(iii) The filament in the air gap region is isothermal.

(iv) The gravitational force, the surface tension between the polymer melt and the air, and

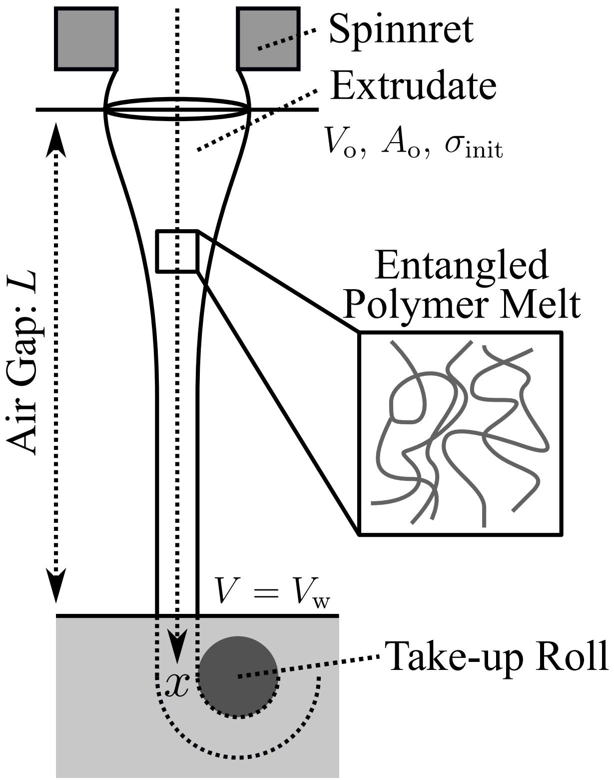

Fig. 3.1: Schematic view of the polymer melt spinning process.

the friction of the filament with the air are all neglected.

(v) The polymer filament is in the melt state just before reaching the surface of the cooling-water; just after it has gone into the water bath, it is solidified instantaneously by cooling.

A number of previous studies made assumptions (i) and (ii), (v) particularly in isothermal condition. However, the initial condition originating from assumption (ii) does not exactly fit with the condition in the real process because the flow history in the die is neglected. To obtain more practical solution, we must consider the shear flow in the die as shown in Refs. [96, 98]. Assumptions (iii) and (iv) appear to be strong for industrial applications. In particular, we should replace the isothermal assumption (iii) with the non-isothermal one to discuss crystallization and/or solidification. In principle, it is possible to consider the non-isothermal condition in our multi-scale method by employing a microscopic polymer model that takes into account temperature change. However, the aim of this study is to assess the present multi-scale simulation method because the industrial application of the multi-scale simulation method has not yet been established. Therefore, it is suitable to make these assumptions in the present work.

Under these conditions, the dynamics of the melt spinning process in the macroscopic scale can be described by the equation of continuity and equation of motion as follows:

$$\begin{aligned} \frac{\partial A\left(x,t\right)}{\partial t} &= -\frac{\partial}{\partial x}\Big(A\left(x,t\right)V\left(x,t\right)\Big), &(3.1)\\ \rho A(x,t)\frac{DV(x,t)}{Dt} &= \frac{\partial}{\partial x}\Big(A(x,t)\sigma(x,t)\Big), &(3.2)\\ \sigma(x,t) = \sigma_{xx} &- \frac{1}{2}\left(\sigma_{yy}+\sigma_{zz}\right) &(3.3)\end{aligned}$$

where x-axis is taken along the spinning line, $A(x,t)$ is the cross-sectional area, $V(x,t)$ is the velocity, and $\sigma_{\alpha\alpha}$ is the normal stress of α-direction at a position x and time t. As seen in Eq. (3.2), the force acting on the filament is given by the tension defined by $T(x,t) \equiv A(x,t)\sigma(x,t)$. The boundary conditions for A and V at x=0 are given as:

$$V(x=0,t) = V_{\text{o}} \quad \text{and} \quad A(x=0,t) = A_{\text{o}}. \tag{3.4}$$

We set the position that shows the maximum of the cross-sectional area to be the origin of the x-axis. In addition, to solve the equations mentioned above, we need an initial value of the normal stress difference σ in Eq. (3.3). In the present work, we use σ_{init} evaluated by a microscopic polymer model at a quiescent state ($\boldsymbol{\kappa} = \mathbf{0}$) based on assumption (ii), where $\boldsymbol{\kappa}$ is the velocity gradient tensor. Strictly speaking, to evaluate $\sigma(x=0,t) = \sigma_{\text{init}}$, we must consider an upstream flow before extrusion from the die. However, considering the flow in the die is beyond the scope of the present work; thus, the boundary condition for σ is given as

$$\sigma(x=0,t) = \sigma_{\text{init}}. \tag{3.5}$$

Here, the initial value of the stress σ_{init} is close to zero but $\sigma_{\mathrm{init}} \neq 0$. At $x = L$, a water bath is settled and the polymer melt filament is cooled to the water temperature. Because the filament is solidified just after entering the water bath, the velocity of the filament at $x = L$ is the same as the winding velocity V_{w}. Namely, the boundary condition for V at $x = L$ is given as

$$V(x = L, t) = V_{\mathrm{w}}. \tag{3.6}$$

The velocity ratio between V_{o} and the winding velocity V_{w} is called the draw ratio $\mathrm{Dr} \equiv V_{\mathrm{w}}/V_{\mathrm{o}}$. It is known that such elongational flow becomes unstable above a critical draw ratio $\mathrm{Dr}^{(\mathrm{c})}$; above the critical draw ratio, the draw resonance phenomenon appears, and the cross-sectional area of the fiber varies periodically. In this study, we consider the spinning process under the draw ratio Dr that is less than the critical draw ratio $\mathrm{Dr}^{(\mathrm{c})}$.

3.2.2 Bridge between Macroscopic and Microscopic Scales

In this section, we briefly explain the multi-scale simulation method for the entangled polymer melt spinning process. For the macroscopic level, governing equations are Eqs. (3.1)∼(3.3). A remaining problem here is to calculate the stress tensor coming from entangled polymer dynamics. To obtain the stress tensor, we employ the Doi-Takimoto slip-link model without SORF presented in Sec. 2.2.1.

The equations used in our simulations are expressed by nondimensional variables. In the macroscopic scale, we choose L as the unit length, $\tau_0 \equiv L/V_{\mathrm{o}}$ as the unit time, and $\sigma_0 \equiv \eta_0 V_{\mathrm{o}}/L$ as the unit stress. Here, η_0 is the zero shear viscosity. In addition, the cross-sectional area A is scaled by A_{o}. In the microscopic scale, we choose a as the unit length, τ_0 as the unit time, and σ_0 as the unit stress. Here, a is the equilibrium length between adjacent slip-links. All of the macroscopic variables are scaled by these units and are expressed with a tilde symbol on their top. After scaling, the macroscopic Eqs. (3.1)∼(3.3) are rewritten as follows:

$$\frac{\partial \widetilde{A}\left(\tilde{x},\tilde{t}\right)}{\partial \tilde{t}} = -\frac{\partial}{\partial \tilde{x}}\Big(\widetilde{A}\left(\tilde{x},\tilde{t}\right)\widetilde{V}\left(\tilde{x},\tilde{t}\right)\Big), \tag{3.7}$$

$$\mathrm{Re}\widetilde{A}(\tilde{x},\tilde{t})\frac{D\widetilde{V}(\tilde{x},\tilde{t})}{D\tilde{t}} = \frac{\partial}{\partial \tilde{x}}\left(\widetilde{A}(\tilde{x},\tilde{t})\tilde{\sigma}(\tilde{x},\tilde{t})\right), \tag{3.8}$$

$$\tilde{\sigma}(\tilde{x},\tilde{t}) = \tilde{\sigma}_{xx} - \frac{1}{2}\left(\tilde{\sigma}_{yy}+\tilde{\sigma}_{zz}\right), \tag{3.9}$$

where Re ($\equiv \rho V_{\mathrm{o}} L/\eta_0$) is the Reynolds number. After scaling, the boundary conditions are as follows:

$$\widetilde{V}(\tilde{x}=0,\tilde{t})=1, \quad \widetilde{V}(\tilde{x}=1,\tilde{t})=\mathrm{Dr}, \quad \widetilde{A}(\tilde{x}=0,\tilde{t})=1, \quad \tilde{\sigma}(\tilde{x}=0,\tilde{t})=\tilde{\sigma}_{\mathrm{init}}. \tag{3.10}$$

In the same manner, the microscopic equations Eq. (2.2) and Eq. (2.5) are rewritten as follows:

$$\frac{d\widetilde{L}_{\mathrm{p}}}{d\tilde{t}} = -\frac{1}{\mathrm{De}}\left(\widetilde{L}_{\mathrm{p}}\left(\tilde{t}\right)-\widetilde{L}_{\mathrm{p,eq}}\right)+\left(\frac{d\widetilde{L}_{\mathrm{p}}}{d\tilde{t}}\right)_{\mathrm{affine}}+\sqrt{\frac{2Z_{\mathrm{eq}}}{3\mathrm{De}\Delta\tilde{t}}}\,g, \tag{3.11}$$

$$\tilde{\sigma}_{\alpha\beta} = \frac{\sigma_{\mathrm{e}}}{\sigma_0}\left\langle\frac{\tilde{r}_{i\alpha}\tilde{r}_{i\beta}}{|\tilde{\boldsymbol{r}}_i|}\right\rangle = \frac{1}{\tilde{\eta}_0(Z_{\mathrm{eq}})}\left\langle\frac{\tilde{r}_{i\alpha}\tilde{r}_{i\beta}}{|\tilde{\boldsymbol{r}}_i|}\right\rangle \tag{3.12}$$

where De ($\equiv \tau_{\mathrm{R}}/\tau_0$) is the Deborah number, and Z_{eq} is the equilibrium number of strands. Here, the primitive path length is expressed as L_{p} instead of L_i in Eq. (2.2) to avoid confusion in the notation.

The control parameters for simulating the isothermal polymer melt spinning process are the Reynolds number (Re), the Deborah number (De) and the draw ratio (Dr). Moreover, the scaled shear viscosity $\tilde{\eta}_0(Z_{\mathrm{eq}})$, depending only on the number of entanglements Z_{eq}, is determined from the bulk slip-link simulation.

Fig. 3.2 (a) and (b) show the schematic picture of our multi-scale simulation method. The spinning line is divided into M regions, which have a constant spatial interval $\Delta x = 1/M$, to solve the macroscopic equations in the Eulerian manner. However, the stress tensor of a

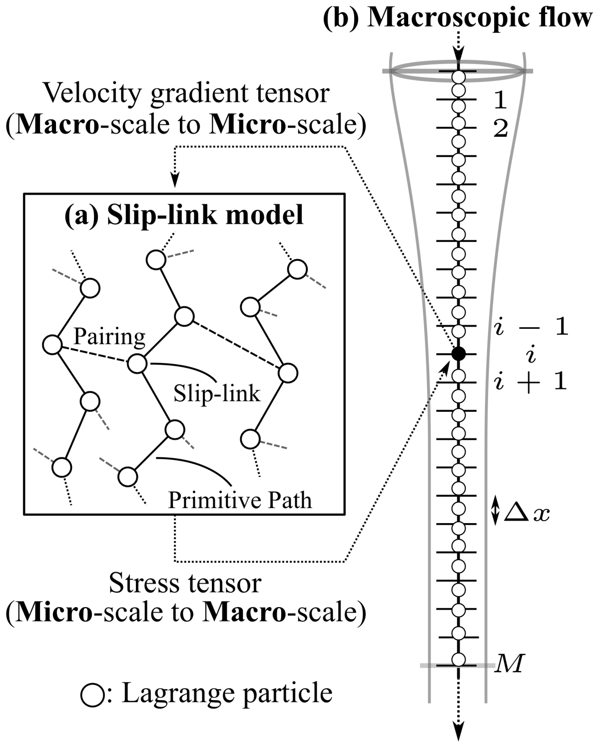

Fig. 3.2: Multi-scale simulation method of a spinning process of a well-entangled polymer melt. (a) Microscopic polymer model and (b) macroscopic fluid dynamics.

polymeric fluid has a historical dependency on the strain rate. Therefore, it is suitable to evaluate the stress tensor on a fluid particle based on the Lagrangian picture, as shown in Fig. 3.2. The procedure of our multi-scale simulation is as follows:

(i) Macroscopic calculation to update the velocity V, the cross-sectional area A, and the position of each Lagrange particle by using Eq. (3.7) and Eq. (3.8). When the position of a Lagrange particle closest to $x = 0$ becomes greater than x_{init}, a new Lagrangian particle located at $x = 0$ is inserted into the system. The state of polymer chains on the newly inserted particle is fully equilibrated under $\boldsymbol{\kappa} = \mathbf{0}$.

(ii) Calculation of the velocity gradient tensor $\boldsymbol{\kappa}$ at the position of each Lagrange particle.

(iii) Microscopic polymer simulation using the slip-link model to update $\boldsymbol{\sigma}$ by using $\boldsymbol{\kappa}$ evaluated in (ii).

(iv) Evaluation of the stress tensor on the staggered lattice, which is obtained by taking an average over the stress tensors on the particles located in between two grid points (*i.e.*, the spatial interval $[(i-1)\Delta\tilde{x},\ i\Delta\tilde{x}]$).

(v) Return to item (i).

The parameters of our multi-scale simulations are determined as follows. In an industrial case, the density, the length of the air gap, the initial value of the cross-sectional area and the spinning velocity are, as an example, $\rho \simeq 1000$ kg/m^3, $L \simeq 0.1$ m, $A_\mathrm{o} \simeq 0.2$ mm^2 and $V_\mathrm{w} \simeq 2 \times 10^3$ m/min, respectively. We treat a low Dr region (Dr $\simeq 10$) in the present work. Therefore, the output velocity is estimated to be $V_\mathrm{o} \simeq 10^2$ m/min. If one considers a melt spinning process for a entangled polystyrene melt with $Z_\mathrm{eq} = 10$ at temperature $T \simeq 200$ °C, the zero shear viscosity η_0 and the Rouse relaxation time τ_R are almost equal to $\eta_0 \simeq 10^3$ Pa $\cdot$ s and $\tau_\mathrm{R} \simeq 10^{-4}$ s, respectively. From these typical values, the Reynolds number (Re) and the Deborah number (De) are calculated as $\mathrm{Re}_0 \simeq 0.33$ and $\mathrm{De}_0 \simeq 3.3 \times 10^{-3}$, respectively. The results indicate that the inertia term cannot be discarded from Eq. (3.8), because the Reynolds number estimated here is based on the velocity at $x = 0$; therefore, the actual Reynolds number becomes larger than unity at approximately $x = L$.

In this chapter, we treat two types of polymer melts $Z_\mathrm{eq} = 10$ and $Z_\mathrm{eq} = 15$. The characteristic times are changed according to the expressions of the relaxation times $\tau_\mathrm{d} = 3Z_\mathrm{eq}^3\tau_\mathrm{e}$ and $\tau_\mathrm{R} = Z_\mathrm{eq}^2\tau_\mathrm{e}$ in the reptation model (In fact, the reptation time τ_d is almost proportional to $Z^{3.45}$ in the slip-link model [67]. However, we estimate the parameters based on the reptation model for simplification). Therefore, the Reynolds number and the Deborah number are changed by replacing the polymer melt from $Z_\mathrm{eq} = 10$ to $Z_\mathrm{eq} = 15$. The Reynolds number and the Deborah number of the polymer melt $Z_\mathrm{eq} = 15$ are estimated to be $\mathrm{Re} \simeq \mathrm{Re}_0 \times 1.5^{-3}$ and $\mathrm{De} \simeq \mathrm{De}_0 \times 1.5^2$. In this chapter, the Reynolds number and the Deborah number are Re $= 0.5$ and De $= 0.004$ in $Z_\mathrm{eq} = 10$ and Re $= 0.15$ and De $= 0.009$ in $Z_\mathrm{eq} = 15$.

In the slip-link simulation, the statistical error of the stress tensor depends on the number of polymers N_p on a Lagrange particle. Here, we show how the stress is affected by a microscopic system consisting of N_p polymer chains. Fig. 3.3 shows the startup elongational

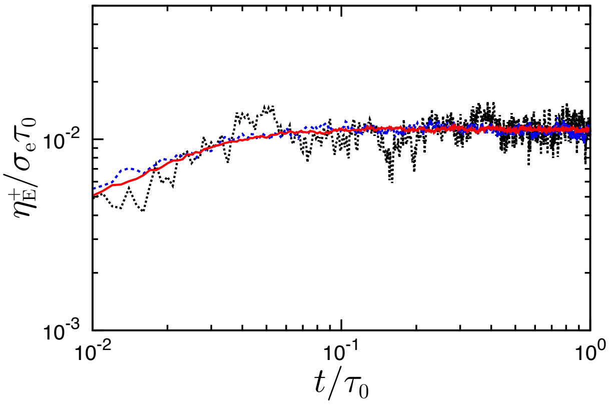

Fig. 3.3: Bulk startup elongational viscosity for $N_{\mathrm{p}} = 10^2$ (black), $N_{\mathrm{p}} = 10^3$ (blue) and $N_{\mathrm{p}} = 10^4$ (red).

viscosity calculated by the slip-link model with a constant velocity gradient $\kappa_{xx}(= dV/dx) = D_{xx} = 15\tau_0^{-1}$, the Deborah number De $= 0.004$ and the equilibrium number of entanglements $Z_{\mathrm{eq}} = 10$, but with different numbers of polymers, $N_{\mathrm{p}} = 10^2$, 10^3, and 10^4. Here, $\boldsymbol{D} \equiv (\boldsymbol{\kappa} + \boldsymbol{\kappa}^{\mathrm{T}})/2$ is the strain rate tensor. $D_{xx} = 15\tau_0^{-1}$ is a typical value in the present multi-scale simulations of the melt spinning process. We confirmed that the statistical error decreases with $1/\sqrt{N_{\mathrm{p}}}$ and decided to use $N_{\mathrm{p}} = 10^3$ as the number of polymers on a single Lagrangian particle from the viewpoint of the trade-off between the accuracy of the stress tensor and the computational cost.

In the multi-scale simulation, we used $M = 100$ as the number of the grid points, $x_{\mathrm{init}} \simeq 10^{-4}$ depending on Dr, Dr $= 10$, 15, 20 for $Z_{\mathrm{eq}} = 10$ and Dr $= 10$ for $Z_{\mathrm{eq}} = 15$, $\Delta t = 1.0 \times 10^{-5}\tau_0$ for $Z_{\mathrm{eq}} = 10$ and $\Delta t = 2.5 \times 10^{-6}\tau_0$ for $Z_{\mathrm{eq}} = 15$. Moreover, we used a parallel computation that is quite effective for our calculation because the calculation of the stress tensor on a fluid particle is independent of those on other fluid particles. We developed a parallelized simulation code by Message Passing Interface (MPI) and performed the calculations by 72 cores for Dr $= 10$ and 15 (Xeon E5-1680v3, 3.2GHz), and by 96 cores for Dr $= 20$ (Xeon E5-2680, 2.7GHz).

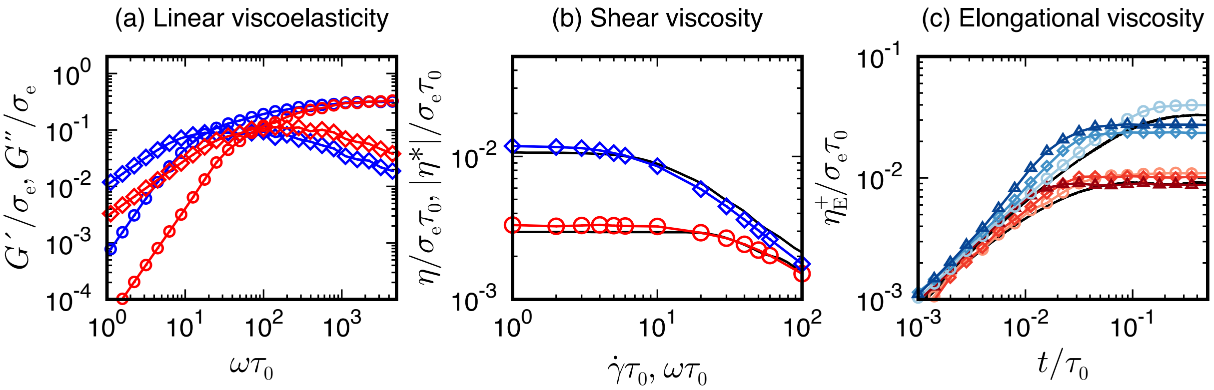

Fig. 3.4: Bulk rheological properties of entangled polymer melts, (a) linear viscoelasticity, (b) shear viscosity and (c) elongational viscosity. In (a), the storage modulus G'(circle), the loss modulus G''(diamond) are plotted against the angular frequency ω for $Z_{\mathrm{eq}} = 10$ (red) and $Z_{\mathrm{eq}} = 15$ (blue). In (b), the shear viscosity η is plotted against the shear rate. The red line corresponds to $Z_{\mathrm{eq}} = 10$, the blue line corresponds to $Z_{\mathrm{eq}} = 15$ and the black line is the absolute value of the complex dynamic viscosity $|\eta^*|$ obtained from the linear viscoelastic data. In (c), the elongational viscosity is plotted against time t for three different strain rates, $D_{xx} = 10\ \tau_0^{-1}$ (circle), $D_{xx} = 50\ \tau_0^{-1}$ (diamond) and $D_{xx} = 100\ \tau_0^{-1}$ (triangle). The red series is for $Z_{\mathrm{eq}} = 10$, the blue series is for $Z_{\mathrm{eq}} = 15$ and the black solid lines are the linear viscosity growth function $3\eta_0^+(t)$.

3.3 Results and Discussion

Unless otherwise stated, in what follows, we omit the tilde symbols on the dimensionless variables (except where doing so might cause confusion) to simplify the resulting expressions.

3.3.1 Macroscopic Behavior

The linear viscoelasticity data obtained for $Z_{\mathrm{eq}} = 10$ (red) and $Z_{\mathrm{eq}} = 15$ (blue) from the slip-link simulation are shown in Fig. 3.4(a). The longest relaxation time $\tau_{\mathrm{d}} \simeq 1.4 \times 10^{-2}\ \tau_0$ for $Z_{\mathrm{eq}} = 10$ and $\tau_{\mathrm{d}} \simeq 5.9 \times 10^{-2}\ \tau_0$ for $Z_{\mathrm{eq}} = 15$ are determined. Fig. 3.4(b) shows the shear viscosity plotted against various shear rates for $Z_{\mathrm{eq}} = 10$ (red) and $Z_{\mathrm{eq}} = 15$ (blue). Moreover, the complex viscosity $|\eta^*|$ (black line) is plotted. From Fig. 3.4(b), we observe the shear thinning and determine the zero shear viscosity. The shear viscosities are $\eta_0 = 3.3 \times 10^{-3}\ \sigma_{\mathrm{e}}\tau_0$ for $Z_{\mathrm{eq}} = 10$ and $\eta_0 = 1.2 \times 10^{-2}\ \sigma_{\mathrm{e}}\tau_0$ for $Z_{\mathrm{eq}} = 15$. (As estimated by the reptation theory, the zero shear viscosities are almost proportional to Z^3). The absolute

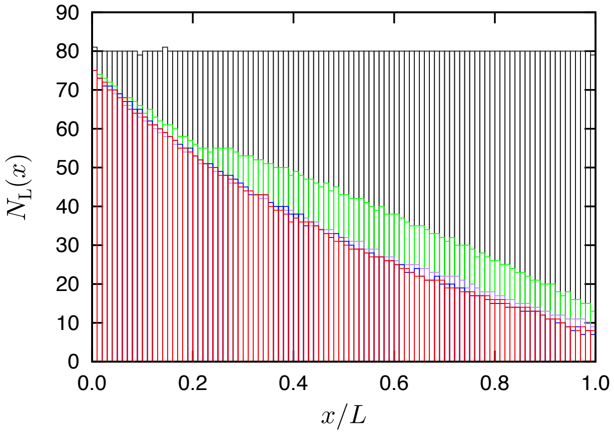

Fig. 3.5: Spatial distributions of the number of Lagrangian particles $N_{\mathrm{L}}(x)$ existing in the interval $[x, x+\Delta x]$ on the spinning line in $\mathrm{Dr} = 10$ at $t = 0$ (black), $t = 0.2$ (green), $t = 0.5$ (purple), $t = 1$ (blue) and $t = 2$ (red). After $t = 0.5$, the distribution of Lagrangian particles shows almost the same shape.

value of the complex dynamic viscosity $|\eta^*|$ shows almost the same behavior as the shear viscosity η, *i.e.*, the Cox-Merz rule holds. Fig. 3.4(c) shows the elongational viscosity plotted against different three strain rates $D_{xx} = 10\ \tau_0^{-1}$ (circle), $D_{xx} = 50\ \tau_0^{-1}$ (diamond) and $D_{xx} = 100\ \tau_0^{-1}$ (triangle). The red series is for $Z_{\mathrm{eq}} = 10$, the blue series is for $Z_{\mathrm{eq}} = 15$ and the black solid lines are the linear viscosity growth function $3\eta_0^+(t)$. From Fig.3.4(c), the elongational viscosities show almost the same behavior as the linear viscosity growth function $3\eta_0^+(t)$. These three strain rates $(D_{xx} < \tau_{\mathrm{R}}^{-1})$ are typical values for our multi-scale simulations. The melt spinning for these two polymer melts are analyzed by the multi-scale simulation method.

Before performing a multi-scale simulation using the slip-link model, the polymer chains should be equilibrated. The equilibration of a polymer chains requires a simulation of the system under $\boldsymbol{\kappa} = \mathbf{0}$ to be performed for a longer time than at least the longest relaxation time τ_{d}. Hence, we equilibrate the microscopic systems on all of the Lagrangian particles for a time duration $t = 0.1\tau_0$ and then start the multi-scale simulations.

Fig. 3.5 shows spatial distributions of the number of Lagrangian particles $N_{\mathrm{L}}(x)$ between two grids $[x, x+\Delta x]$ with $\Delta x = 1/M$. At $t = 0$, the particle distribution is set to be almost uniform, and the total number of Lagrangian particles in the spinning line $N_{\mathrm{L}}^{(\mathrm{Total})}$ is

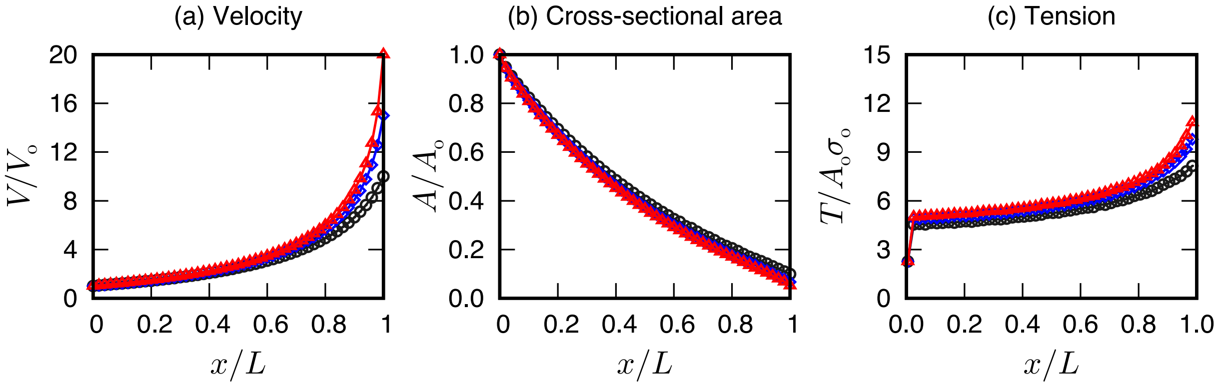

Fig. 3.6: Macroscopic properties at steady state obtained from the multi-scale simulation for a polymer melt $Z_{\rm eq} = 10$. (a) Velocity, (b) cross-sectional area and (c) tension profiles along the spinning line for three draw ratios Dr = 10 (black), 15 (blue) and 20 (red), respectively. Each data point is averaged over the time duration from $t = 1$ to 2.

approximately 8000 for Dr = 10. The number of particles decreases over time and reaches a steady state at approximately $t = 0.5$, as shown in Fig.3.5. After $t \simeq 0.5$, the distribution of Lagrangian particles shows almost the same shape, and the total number of Lagrange particles $N_{\rm L}$ is $N_{\rm L}^{\rm (Total)} \simeq 3400$.

Fig. 3.6 shows the velocity (a), the cross-sectional area (b) and the tension (c) averaged over the time duration from $t = 1$ to $t = 2$ of the filament as a function of the position x at steady state. We investigate the change in these physical variables at steady state by altering the draw ratio Dr ($\equiv V_{\rm w}/V_{\rm o}$). Here, the standard errors of each data are almost the same as or less than the sizes of symbols in Fig. 3.6(a) and (b). In Fig. 3.6(c), standard errors are slightly larger than symbols mainly in the vicinity of the end of the spinning line because the number of Lagrangian particles $N_{\rm L}(x)$ in the region is less than that at the upstream side, as shown in Fig. 3.5. From Fig. 3.6(b), the cross-sectional area profile slightly decreases as increasing Dr. Compared with the velocity and tension profiles, the cross-sectional area profile depends only slightly on Dr. The microscopic structure however show significant difference, as explained later in Fig. 3.9 and Fig. 3.10. From Fig. 3.6(c), the tension of the filament profile increases as increasing Dr. In particular, in the region at the end of the spinning line, the tension increases in response to the large velocity gradient by increasing

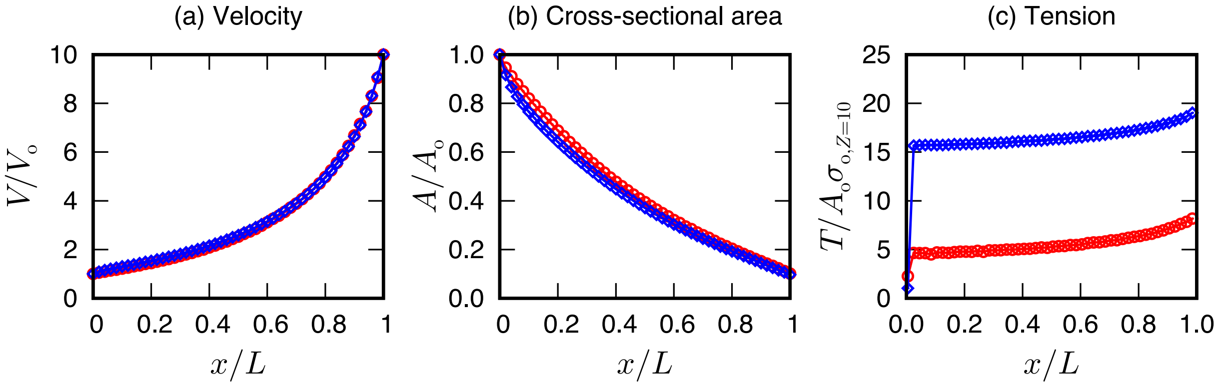

Fig. 3.7: Macroscopic properties at steady state obtained from the multi-scale simulation for Dr = 10. (a) Velocity, (b) cross-sectional area and (c) tension profiles along the spinning line for two different polymer melts $Z_\mathrm{eq} = 10$ (red) and $Z_\mathrm{eq} = 15$ (blue). Each data point is averaged over the time duration from $t = 0.5$ to 1.

the Dr. Moreover, a steep increase in tension T is observed at the region very close to $x = 0$ because the initial state of polymer chains is almost isotropic because of assumption (ii). To reduce this steep increase of the tension, we should consider an upstream flow in a die. However, considering an upstream flow in the die is outside the scope of the current work and will be investigated in future work. Fig. 3.7 shows the velocity (a), the cross-sectional area (b) and the tension (c) of the filament as a function of the position x at steady state in Dr = 10 for two different polymer melts of $Z_\mathrm{eq} = 10$ (red) and $Z_\mathrm{eq} = 15$ (blue). The values are averaged over the time duration from $t = 0.5$ to $t = 1$. Regarding the standard errors of the data in Fig. 3.7, the tendencies are the same as those in Fig. 3.6. The velocity profile for the polymer melt of $Z_\mathrm{eq} = 15$ is almost the same as that of the polymer melt of $Z_\mathrm{eq} = 10$, but the former is slightly higher especially at the beginning of the spinning line. The phenomenon occurs because the elastic effect coming from the slow relaxation of the well-entangled polymer melt is strong in the polymer melt $Z_\mathrm{eq} = 15$. The cross-sectional area for $Z_\mathrm{eq} = 15$ is smaller than that for $Z_\mathrm{eq} = 10$, especially in the beginning of the spinning line. This tendency for the cross-sectional area A is consistent with that expected from the velocity profiles, as shown in Fig. 3.7(a). Moreover, we can confirm that the tension profiles for $Z_\mathrm{eq} = 15$ is almost three times larger than that for $Z_\mathrm{eq} = 10$, as seen from Fig. 3.7(c).

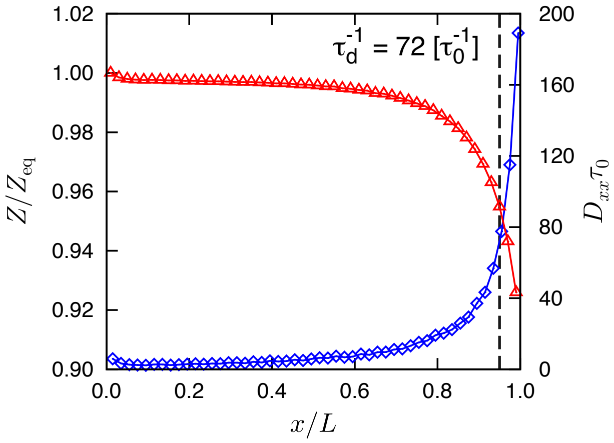

Fig. 3.8: The average number of entanglements normalized by the equilibrium number of entanglements Z_{eq} ($Z_{\text{eq}} = 10$) (red) and the velocity gradient κ_{xx} ($= D_{xx}$) (blue) profiles along the spinning line for $\text{Dr} = 20$. A vertical line at $x \simeq 0.9$ divides the spinning line into a linear and an orienting region.

3.3.2 Microscopic Behavior

We also investigate the microscopic state of the polymer chains as a function of position x. Fig. 3.8 shows the average number of entanglements Z normalized by Z_{eq} (red) and the velocity gradient κ_{xx} ($= D_{xx}$) (blue) along the spinning line. In the initial part of the spinning line, the average number of entanglements Z decreases slightly, and the velocity gradient κ_{xx} ($= D_{xx}$) increases because the initial value of stress is almost zero. This effect, however, vanishes at a position not far from the position $x = 0$. We can see that the number of entanglements decreases, particularly in the vicinity of the end section. This phenomenon occurs because the convective constraint release (CCR) effect starts to work strongly after a position at approximately $x \simeq 0.9$ where the velocity gradient κ_{xx} ($= D_{xx}$) steeply increases. By introducing the Weissenberg number ($\text{Wi}_{\text{d}}^{(\text{e})}$), defined as $\text{Wi}_{\text{d}}^{(\text{e})} = \tau_{\text{d}} D_{xx}$, the system can be quantitatively divided into two characteristic regions. The first region is the linear region ($\text{Wi}_{\text{d}}^{(\text{e})} < 1$), and the second is the orienting region ($\text{Wi}_{\text{d}}^{(\text{e})} > 1$). The region where the velocity gradient is greater than $\tau_{\text{d}}^{-1} = 72\tau_0^{-1}$ corresponds to the $\text{Wi}_{\text{d}}^{(\text{e})} > 1$. From Fig. 3.8, the number of entanglements is almost constant in the linear region and decreases drastically in the orienting region corresponding to $x \gtrsim 0.95$. Moreover, Fig. 3.9 shows the

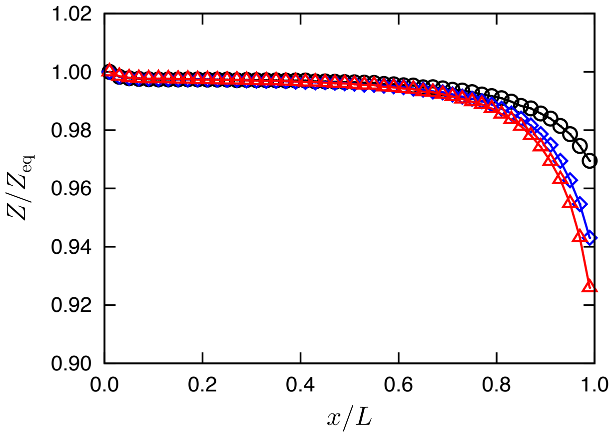

Fig. 3.9: The average number of entanglements Z normalized by the equilibrium number of entanglements Z_{eq} ($Z_{\mathrm{eq}} = 10$) for different three draw ratios Dr = 10 (black), Dr = 15 (blue) and Dr = 20 (red).

average number of entanglements Z normalized by Z_{eq} for different three draw ratios Dr = 10 (black), Dr = 15 (blue) and Dr = 20 (red). The number of entanglements decreases at the end part of the spinning line with increasing Dr because of the higher velocity gradients κ_{xx} ($= D_{xx}$).

Fig. 3.10 shows the superimposed conformation of all of the polymer chains by fixing the center of mass to the origin for three different draw ratios Dr = 10 (black), Dr = 15 (blue), and Dr = 20 (red) in Lagrange particles located at typical four points (a) $x \simeq 0$, (b) $x \simeq 0.5$, (c) $x \simeq 0.75$ and (d) $x \simeq 1$. In these figures, the flow direction is the x-axis, and the perpendicular direction to the flow is the y-axis. The polymer chains at $x \simeq 0$ are almost isotropic because of assumption (ii), but they have already been stretched slightly along the flow direction. At $x \simeq 0.5$ and at $x \simeq 0.75$, the polymer chains are clearly stretched along the x-direction. Moreover, after going through the orienting region ($\mathrm{Wi}_{\mathrm{d}}^{(\mathrm{e})} > 1$) mentioned above, the polymer chain is strongly stretched and oriented along the x-direction as shown in Fig3.10(d). It is also found that the orientation is enhanced by increasing Dr. To evaluate the orientation quantitatively, we introduce the conformation tensor described as follows:

$$W_{\alpha\beta} = \langle R_\alpha R_\beta \rangle = \frac{1}{N_{\mathrm{p}}} \sum_{i=1}^{N_{\mathrm{p}}} R_{i\alpha} R_{i\beta} \tag{3.13}$$

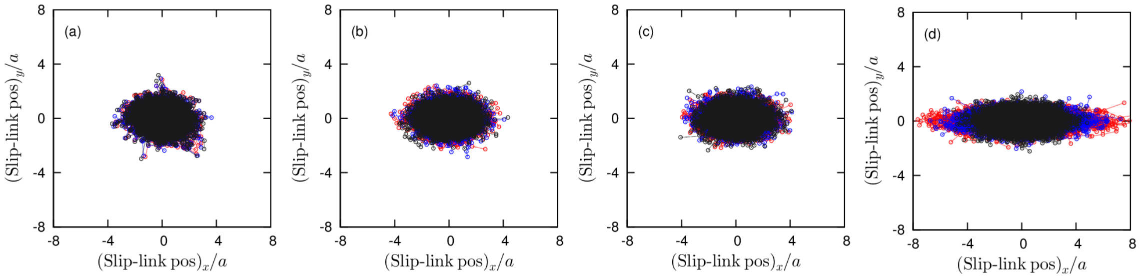

Fig. 3.10: The structure of the polymer chain in Lagrange particles for three different draw ratios Dr = 10 (black), Dr = 15 (blue) and Dr = 20 (red) located at typical four points (a) $x \simeq 0$, (b) $x \simeq 0.5$, (c) $x \simeq 0.75$ and (d) $x \simeq 1$. The 3D conformation of the polymer chain is projected on the xy plane. Here, the x-axis is the flow direction, and the y-axis is the perpendicular to the flow direction.

Table 3.1: Orientation parameter.

Dr	$\lambda_{\max}(x \simeq 0)$	$\lambda_{\max}(x \simeq 0.5)$	$\lambda_{\max}(x \simeq 0.75)$	$\lambda_{\max}(x \simeq 1)$
10	0.36	0.41	0.43	0.64
15	0.36	0.39	0.47	0.82
20	0.36	0.42	0.51	0.89

where $\boldsymbol{R}_i$ is the end-to-end vector of a polymer chain i. Note that $\mathrm{Tr}\boldsymbol{W} = \langle \boldsymbol{R}^2 \rangle$. The eigenvalues λ_α of $\boldsymbol{W}$ indicate the degree of orientation in each direction [162]. We define the normalized conformation tensor as $\boldsymbol{S} = \boldsymbol{W}/\mathrm{Tr}\boldsymbol{W}$. When the polymer melt is isotopic, $S_{\alpha\beta} = \delta_{\alpha\beta}/3$. We can define the orientation parameter $\lambda_{\max}$, which denotes the degree of orientation, by the largest eigenvalue of $\boldsymbol{S}$. Here, the orientation parameter should be 1/3 when a conformation of the polymer chains is isotropic. Table 3.1 shows the orientation parameter at four typical points along the spinning line. From Table 3.1, we can see how the polymer chains are oriented to the x-direction quantitatively. The polymer chains at $x \simeq 0$ are almost isotropic but are weakly stretched because the values are slightly larger than 1/3, and the chains are clearly oriented to the x-direction at $x \simeq 0.5$ and $x \simeq 0.75$. Moreover, the degree of orientation is drastically enhanced at $x \simeq 1$. This tendency gives good agreement with Fig. 3.10.

Next, to analyze the entanglements on polymer chains in detail, we introduce an internal

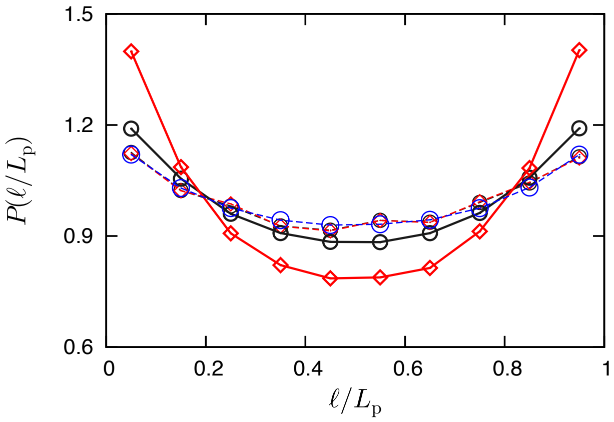

Fig. 3.11: Probability density of entanglements $P(\tilde{\ell})$ as a function of the internal coordinate $\tilde{\ell}$ on a polymer chain at $x \simeq 0$ (dashed line) and $x \simeq 1$ (solid line) for $\mathrm{Dr} = 10$ (black circle) and $\mathrm{Dr} = 20$ (red diamond). Each data point is averaged over the time duration from $t = 1$ to 2. Moreover, the blue circle is the probability density for a quiescent state ($\boldsymbol{\kappa} = \mathbf{0}$).

coordinate ℓ as the length along the primitive path of a polymer chain from one of the ends to the other. The internal coordinate is scaled by the length of the primitive path L_p. In addition, the polymer chains are divided into M_p sections, which have a constant interval $\Delta\ell = L_\mathrm{p}/M_\mathrm{p}$ ($M_\mathrm{p} = 10$). By using the internal coordinate $\tilde{\ell}$, we define an average probability density of entanglements $P(\tilde{\ell}) \equiv \langle \delta Z(\tilde{\ell})/Z \rangle$, where Z is the total number of entanglements on a polymer chain and $\delta Z(\tilde{\ell})$ is the number of entanglements in the interval $[(i-1)\Delta\ell,\ i\Delta\ell]$ ($1 \leq i \leq M_\mathrm{p}$) on the same chain, and $\langle \cdots \rangle$ denotes the statistical average of $(\cdots)$. By definition, $P(\tilde{\ell})$ satisfies the condition $\int_0^1 P(\tilde{\ell}) d\tilde{\ell} = 1$. In Fig. 3.11, we show the average density of entanglements $P(\tilde{\ell})$ at $x \simeq 0$ (thin dashed line) and $x \simeq 1$ (bold solid line) for $\mathrm{Dr} = 10$ (black circle) and $\mathrm{Dr} = 20$ (red diamond) averaged over the time duration from $t = 1$ to $t = 2$ as a function of $\tilde{\ell}$. Moreover, the probability density for a quiescent state ($\boldsymbol{\kappa} = \mathbf{0}$) is plotted in Fig. 3.11 (blue circle). The probability density $P(\tilde{\ell})$ is almost the same as the quiescent state at $x \simeq 0$. At $x \simeq 1$, we observe that the number of entanglements mainly decreases in the middle region of a polymer chain and increases at both ends. Moreover, the tendency is enhanced with increasing Dr. The entanglements at the both ends is actively created or removed depending on the length of strands in the slip-link model. In contract, the entanglements in the middle region are created or removed only in a passive manner.

Therefore, the frequency of a recreation of the entanglement at the ends is higher than that in the middle region. The above-described microscopic information leads to a new idea and insight for the design of a polymer melt that has desirable physical properties for use in a fiber.

3.4 Conclusion

In this chapter, we successfully applied a multi-scale simulation method to spinning processes of well-entangled polymer melts. The rheological properties were obtained by a coarse-grained polymer model called the slip-link model, which can universally describe the entangled polymer melt. In our multi-scale simulations, the macroscopic equations were solved using the Eulerian picture. The stress tensors coming from entangled polymer chains were calculated on all the fluid particles based on the Lagrangian picture as a response to the local velocity gradient tensors obtained macroscopically at the positions of the fluid particles.

We investigated the microscopic information based on the multi-scale simulations. We found that the number of entanglements decreases with flow because of the convective constraint release (CCR) effect. By introducing the Weissenberg number, we determined the linear region and the orienting region and found that the microscopic structure is mainly altered in the orienting region. Moreover, we found that the number of entanglements mainly decreases in a middle region on a polymer chain and is enhanced at both ends. This information will be useful for a molecular design optimized for producing a strong fiber.

We hope that the multi-scale simulation method takes us to a new stage in the field of material science. In many industrial applications, the temperature change, including cooling air, plays an important role for solidification and/or crystallization. A detailed mechanism of the solidification and/or crystallization that occurs along the spinning line has not been clarified yet. To address the effects of solidification and/or crystallization, we must develop a multi-scale simulation method that can take into account temperature change by employing another microscopic model. Moreover, we used mono-disperse linear polymer melts in the present work. However, in the realistic spinning case, various types of the polymer melts composed of poly-dispersed linear, star and branched polymers melts and mixtures thereof are used to realize desirable properties. Such polydispersity and blends of different chain architectures can be considered in our multi-scale simulation method by developing the slip-link model or employing a new microscopic model.

A high computational cost is always one of problems in this type of multi-scale simulation. To overcome the problem, we must improve the numerical schemes, including the parallelization of the numerical codes. Thereby the multi-scale simulation method will become a new and effective tool for analyzing the melt spinning process.

4 Multi-Scale Simulations for Flows of a Well-Entangled Polymer Melt in a Contraction-Expansion Channel

4.1 Introduction

In this chapter, we focus specifically on flows in a contraction-expansion channel, which can be considered to be one of the model flow geometries in the injection molding process. The contraction-expansion channel is one of the complex flow geometries, and flows in this channel have been extensibly examined with both experiments and numerical simulations [102, 103, 105–107, 109]. However, to the best of our knowledge, the majority of previous studies have employed the constitutive equations such as the Pom-Pom model [103, 105] and the Rolie-Poly model [106, 107], except for a few MSS approaches [115, 131].

To develop a more sophisticated method for predicting flow properties in the contraction-expansion channel, the focus in this chapter is on the MSS method originally developed by Murashima and Taniguchi [137, 142]. Using this MSS method, they have successfully examined flows of an entangled polymer melt around a cylinder [137]. Based on this background, the aim of the present chapter is to extend the MSS method developed by Murashima and Taniguchi to flows in the contraction-expansion channel and to assess the present MSS method.

4.2 Smoothed Particle Hydrodynamics

4.2.1 Lagrangian Fluid Particle Method

Here, we present a Lagrangian fluid particle method that is employed as the macroscopic fluid simulation model in the MSS method. Since entangled polymer chains show slow relaxations, a macroscopic flow of the entangled polymer melt depends on the strain rate history. Therefore, to employ a simulation technique in a Lagrangian manner is suitable for properly analyzing flows of entangled polymer melts. To describe macroscopic flows in the contraction-expansion channel, we employ the Lagrangian picture, where a fluid is described by a number of fluid particles. At the macroscopic level of the MSS, the dynamics of fluid particle i is described by the following equations based on the Lagrangian picture:

$$\frac{\mathrm{d}\boldsymbol{x}_i}{\mathrm{d}t} = \boldsymbol{v}_i, \tag{4.1}$$

$$\frac{\mathrm{d}\boldsymbol{v}_i}{\mathrm{d}t} = \frac{1}{\rho_i}\big[\boldsymbol{\nabla}\cdot(\boldsymbol{\sigma} - P\boldsymbol{I})\big]_{\boldsymbol{x}_i} + \boldsymbol{F}_i \tag{4.2}$$

where $\boldsymbol{x}_i$ and $\boldsymbol{v}_i$ are the position and velocity of fluid particle i, respectively; ρ_i is the density; and $\boldsymbol{F}_i$ is the external body force at position $\boldsymbol{x}_i$. The first term on the right-hand side in Eq. (4.2) is calculated by taking a spatial derivative of the field $(\boldsymbol{\sigma} - P\boldsymbol{I})$ constructed from sets $\{\boldsymbol{\sigma}_j\}$ and $\{P_j\}$ based on an interpolation method explained later in Eq. (4.4), where $\boldsymbol{\sigma}$ and P are the stress tensor field and pressure field, respectively; $\boldsymbol{\sigma}_j$ and P_j are the stress tensor and pressure on fluid particle j located at position $\boldsymbol{x}_j$, respectively; and $\boldsymbol{I}$ is the unit tensor. In this study, the stress tensor $\boldsymbol{\sigma}_i$ is described as follows:

$$\boldsymbol{\sigma}_i = \boldsymbol{\sigma}_i^{(\mathrm{p})} + \boldsymbol{\sigma}_i^{(\mathrm{d})} \tag{4.3}$$

where $\boldsymbol{\sigma}_i^{(\mathrm{p})}$ is the stress originating from the temporal network of the entangled polymer chains and $\boldsymbol{\sigma}_i^{(\mathrm{d})}$ $(\equiv \eta_\mathrm{d}(\boldsymbol{\kappa}_i+\boldsymbol{\kappa}_i^\mathrm{T}))$ is the dissipative stress arising from a non-bonding interaction between unentangled parts [137]. Here, η_d is the Newtonian viscosity, and $\boldsymbol{\kappa}_i$ is the velocity gradient tensor $(\nabla\boldsymbol{v})|_{\boldsymbol{x}_i}$ at position $\boldsymbol{x}_i$. The dissipative stress $\boldsymbol{\sigma}_i^{(\mathrm{d})}$ is generally neglected in flow problems of well-entangled polymer melts because the magnitude of the dissipative stress is quite small compared with the stress originating from the temporal polymer network $\boldsymbol{\sigma}_i^{(\mathrm{p})}$. However, in the present MSS, we take the contribution from the dissipative stress $\boldsymbol{\sigma}_i^{(\mathrm{d})}$ to the total stress into account to stabilize the simulation by suppressing relative stress fluctuations in less-important velocity regions, *e.g.*, at the corners in the flow path.

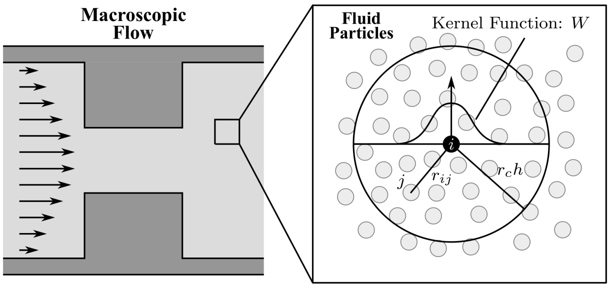

Fig. 4.1: Schematic illustration of the Smoothed Particle Hydrodynamics (SPH) method.

4.2.2 Basic Equations of Smoothed Particle Hydrodynamics

To solve Eqs. (4.1) and (4.2), we employ a Lagrangian fluid particle method. There are several types of fluid particle methods, such as a Smoothed Particle Hydrodynamics (SPH) method [163], and a Moving-Particle Semi-implicit (MPS) method [164]. In this study, we employ the SPH method originally developed by Gingold and Monaghan [163] as schematically shown in Fig. 4.1. In SPH, a fluid is discretized into a number of fluid particles, and a physical quantity $A(\boldsymbol{x}_i)$ is determined by the following equation:

$$A(\boldsymbol{x}_i) = \int A(\boldsymbol{x}')W(\boldsymbol{x}_i - \boldsymbol{x}', h)d\boldsymbol{x}' \simeq \sum_j \frac{m_j}{\rho_j} A(\boldsymbol{x}_j)W(\boldsymbol{x}_i - \boldsymbol{x}_j, h) \tag{4.4}$$

where $W(\boldsymbol{x}_i - \boldsymbol{x}', h)$ is the smoothing kernel function, h is the smoothing length, m_j is the mass of fluid particle j, and ρ_j is the density of fluid particle j. In this study, we use the following Gaussian kernel:

$$W(\boldsymbol{x}_i - \boldsymbol{x}_j, h) = \frac{1}{(h\sqrt{\pi})^n} \exp\left[-\left(\frac{\boldsymbol{x}_i - \boldsymbol{x}_j}{h}\right)^2\right], \tag{4.5}$$

where n is the dimension. From Eq. (4.4), the density $\rho(\boldsymbol{x}_i)$ at position $\boldsymbol{x}_i$ can be obtained as

$$\rho(\boldsymbol{x}_i) \simeq \sum_j m_j W(\boldsymbol{x}_i - \boldsymbol{x}_j, h). \tag{4.6}$$

Moreover, a spatial derivative of the physical quantity $\nabla A(\boldsymbol{x}_i)$ is expressed by using a derivative of the kernel function as

$$\nabla A(\boldsymbol{x}_i) = \int A(\boldsymbol{x}')\nabla W(\boldsymbol{x}_i - \boldsymbol{x}', h)d\boldsymbol{x}' \simeq \sum_j \frac{m_j}{\rho_j} A(\boldsymbol{x}_j)\nabla_i W(\boldsymbol{x}_i - \boldsymbol{x}_j, h). \tag{4.7}$$

Similarly, a second derivative of the physical quantity $\nabla^2 A(\boldsymbol{x}_i)$ is expressed by using a second derivative of the kernel function as

$$\nabla^2 A(\boldsymbol{x}_i) \simeq \sum_j \frac{m_j}{\rho_j} A(\boldsymbol{x}_j)\nabla_i^2 W(\boldsymbol{x}_i - \boldsymbol{x}_j, h). \tag{4.8}$$

However, this expression is too sensitive to particle disorder to be practically employed [165]. Alternatively, the following expression for a second derivative is frequently used:

$$\nabla^2 A(\boldsymbol{x}_i) \simeq \sum_j \frac{2m_j}{\rho_i \rho_j} \left(A(\boldsymbol{x}_j) - A(\boldsymbol{x}_i)\right) \frac{(\boldsymbol{x}_j - \boldsymbol{x}_i) \cdot \nabla_i W(\boldsymbol{x}_i - \boldsymbol{x}_j, h)}{|\boldsymbol{x}_j - \boldsymbol{x}_i|^2}, \tag{4.9}$$

which is called the Morris formula [166].

There are primarily two types of SPH methods for simulating incompressible fluids, which satisfy Eq. (1.2). The first is weakly compressible SPH (WCSPH), and the second is incompressible SPH (ISPH). In WCSPH [141, 166], density fluctuations are suppressed within 1% by employing the equation of state including a speed of sound to provide a very low Mach number. Note that WCSPH is acceptable for a low Reynolds number case [167]. On the other hand, in ISPH [167–169], the incompressibility is basically achieved by introducing the projection method that can numerically solve the incompressible Navier-Stokes equation. Generally, due to the pressure projection algorithm for a pressure Poisson equation, the ISPH method has a higher computational cost than the WCSPH method. Moreover, in this study, we consider polymeric flows that have low Reynolds numbers. Therefore, we employ the WCSPH method.

The dynamic pressure used in the WCSPH method is determined by the following equa-

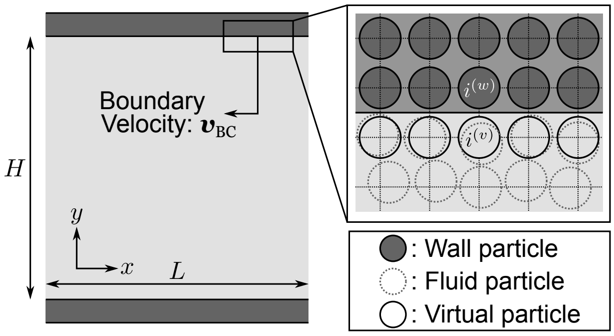

Fig. 4.2: Schematic illustration of how to provide the velocity of a wall particle from the boundary condition.

tion of state:

$$P_i^{(\mathrm{d})} = \frac{c_{\mathrm{s}}^2 \rho_0}{\gamma}\left[\left(\frac{\rho_i}{\rho_0}\right)^{\gamma} - 1\right] \tag{4.10}$$

where c_{s} is the speed of sound and ρ_0 is the initial density. The speed of sound c_{s} should be determined such that the density fluctuation can be suppressed within 1%. Moreover, in a low Reynolds number case corresponding to this study, the exponent $\gamma = 1$ is widely used to evaluate the dynamic pressure [166].

The no-slip boundary condition is imposed in this study. There are mainly two approaches to implement the no-slip boundary condition in SPH simulations. The first is the method to introduce virtual particles [170], and the second is the method that uses boundary particle forces [171]. In the MSS simulations shown in the chapter 4, we employ the former method. Fig. 4.2 shows the schematic illustration that realizes the no-slip boundary condition. As shown in Fig. 4.2, fluid particles distribute randomly, while wall particles are regularly arranged to mimic the wall. At every time step, we place a virtual particle $i^{(v)}$ $(1 \leq i^{(v)} \leq N_{\mathrm{w}})$ in a position symmetrical to a wall particle $i^{(w)}$ $(1 \leq i^{(w)} \leq N_{\mathrm{w}})$ with respect to the boundary. Here, N_{w} is the number of wall particles forming the first layer that is closest to the fluid phase. After placing the virtual particles, we calculate the velocities at the positions of virtual particles by using the basic SPH method. Following this procedure, we calculate the velocity of the wall particle as follows:

$$\boldsymbol{v}_{i^{(w)}} = 2\boldsymbol{v}_{\mathrm{BC}} - \boldsymbol{v}_{i^{(v)}} \tag{4.11}$$

where $\boldsymbol{v}_{\mathrm{BC}}$ is the value of velocity at the boundary position ($\boldsymbol{v}_{\mathrm{BC}} = \mathbf{0}$ for the no-slip boundary condition) and $\boldsymbol{v}_{i^{(v)}}$ and $\boldsymbol{v}_{i^{(w)}}$ are the velocities at the positions of the virtual particle $i^{(v)}$ and the wall particle $i^{(w)}$, respectively.

4.2.3 Poiseuille and Couette Flows for a Newtonian Fluid

Here, two test cases for SPH simulations are shown: one is the Couette flow, and the other is the Poiseuille flow. In both cases, flows between parallel plates located at $y = -H/2$ and $y = +H/2$ are considered. For the left and right boundaries, periodic boundary conditions are employed to consider flows between infinite parallel plates. Here, a Newtonian fluid is employed to validate the SPH.

The first test case is the Couette flow. Initially, the fluid velocity is set to zero. At time $t = 0$, the upper plate moves at constant velocity $+V_{\mathrm{wall}}$, and the lower plate moves at constant velocity $-V_{\mathrm{wall}}$. The series solution for the time dependent behavior of the Couette flow can be written as

$$v_x(y,t) = \frac{2V_{\mathrm{wall}}}{H}y - \frac{2V_{\mathrm{wall}}}{\pi}\sum_{n=1}^{\infty}\frac{1}{n}\sin\left[\pi n\left(1-\frac{2y}{H}\right)\right]\exp\left(-\frac{4\pi^2\nu n^2}{H^2}t\right), \tag{4.12}$$

where V_{wall} is the wall velocity, $\nu = \eta/\rho$ is the kinetic viscosity [166]. The flow is simulated using SPH for $V_{\mathrm{wall}} = 4\times10^{-5}$ m/s, $H = 0.01$ m, $\rho = 10^3$ kg/m^3, $\eta = 10^{-3}$ Pa$\cdot$s, and with 40 particles spanning the channel. As shown in Fig. 4.3 (a), the simulation results are in good agreement with the series solution.

The second test is the Poiseuille flow. Initially, the fluid velocity is set to zero. The flow is induced by a body force F_x parallel to x-axis for time $t \geq 0$. The series solution for the

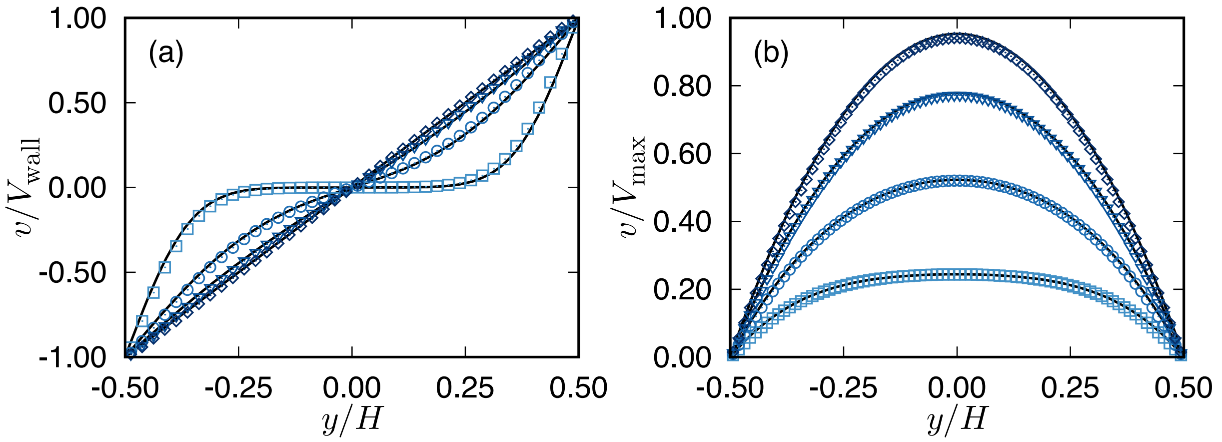

Fig. 4.3: Comparison of SPH and series solutions. In (a), the flow profiles for the Couette flow is plotted against position y/H for deferent four times, $t/\tau_0 = 1$ (square), $t/\tau_0 = 5$ (circle), $t/\tau_0 = 10$ (reverse triangle) and $t/\tau_0 = 200$ (diamond), where τ_0 is the unit time. In (b), the flow profiles for the Poiseuille flow is plotted against position y/H for deferent four times, $t/\tau_0 = 20$ (square), $t/\tau_0 = 50$ (circle), $t/\tau_0 = 100$ (reverse triangle) and $t/\tau_0 = 200$ (diamond). The black solid lines are analytical solutions at the corresponding time.

time dependent behavior of the Poiseuille flow can be written as

$$\begin{aligned} v_x(y,t) = &-\frac{F_x}{2\nu}\left(y+\frac{H}{2}\right)\left(y-\frac{H}{2}\right) \\ &-\frac{4F_xH^2}{\pi^3\nu}\sum_{n=0}^{\infty}\frac{(-1)^n}{(2n+1)^3}\cos\left[\frac{\pi y}{H}(2n+1)\right]\exp\left(-\frac{\pi^2\nu\,(2n+1)^2}{H^2}t\right), \end{aligned} \tag{4.13}$$

where F_x is the external force [166]. The flow is simulated using SPH for $F = 3.2\times10^{-7}$ m/s^2, $H = 0.01$ m, $\rho = 10^3$ kg/m^3, $\eta = 10^{-3}$ Pa $\cdot$ s, and with 80 particles spanning the channel. As shown in Fig. 4.3 (b), the simulation results are in reasonably agreement with the series solution. The slight deviation in a steady state presumably comes from resolution of the simulation.

4.2.4 Stabilization methods in the SPH

The original SPH method has some problems. For example, the physical quantities near wall boundaries cannot be treated accurately, and fluid particles form clusters, which cause a numerical instability. In the MSS simulations shown in this chapter, to overcome inaccuracy

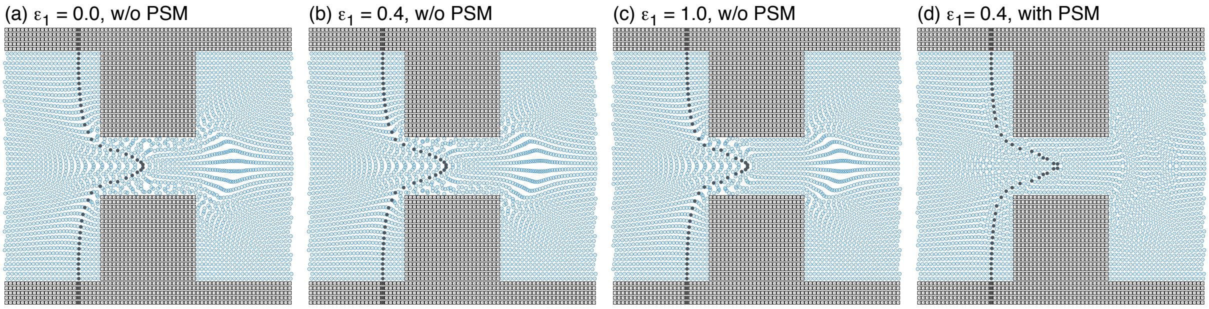

Fig. 4.4: Flow profiles obtained from SPH simulations. In (a)∼(c), the flow profiles without the particle shifting method are plotted for four different XSPH parameter values. In (d), the flow profile with the particle shifting method is plotted.

in the physical quantities near wall boundaries, we employed the modified SPH (MSPH) method developed by Zhang and Batra [172], which is based on the Taylor expansion of the SPH averages (see Ref. [172] for more information). The MSPH method enables accurate evaluations of physical properties near boundaries.

Additionally, in the SPH simulations, particle clusterings cause a numerical instability. To prevent spatial inhomogeneity of fluid particles by the clusterings, it is quite effective to employ the following two methods when calculating the time evolution of Eq. (4.1).

The first one is the XSPH method developed by Monaghan [173]. In the XSPH method, the time integration of Eq. (4.1) is performed as follows:

$$\frac{\mathrm{d}\boldsymbol{x}_i}{\mathrm{d}t} = \hat{\boldsymbol{v}}_i = \boldsymbol{v}_i + \epsilon_1 \sum_j \frac{m_j}{\rho_j} \left(\boldsymbol{v}_j - \boldsymbol{v}_i\right) W(\boldsymbol{x}_i - \boldsymbol{x}_j, h) \tag{4.14}$$

where $\boldsymbol{v}_i$ and $\boldsymbol{v}_j$ are the velocities of fluid particles i and j, respectively, and ϵ_1 is a constant ($0 \leq \epsilon_1 \leq 1$). Figs. 4.4 (a)∼(c) show the flow profiles obtained from the SPH simulations with the XSPH method for (a) $\epsilon_1 = 0.0$, (b) $\epsilon_1 = 0.4$, and (c) $\epsilon_1 = 1.0$. As shown in Fig. 4.4 (a), fluid particles form small clusters in the narrow channel region and string structures after passing through the narrow channel. When increasing the value of ϵ_1, fluid particles in the narrow channel region becomes dispersed. However, string structures after passing through the narrow channel do not disappear only by the XSPH method.

The second one is the particle shifting method developed by Xu *et al* [168]. To prevent particles from clustering, the fluid particles are slightly shifted every time step. The shifting vector $\Delta \boldsymbol{x}_i$ of particle i located at position $\boldsymbol{x}_i$ is determined as follows:

$$\Delta \boldsymbol{x}_i = \epsilon_2 b \boldsymbol{n}(\boldsymbol{x}_i) \tag{4.15}$$

where ϵ_2 is a shifting parameter ($0.001 \leq \epsilon_2 \leq 0.1$), b is the initial distance between fluid particles, and $\boldsymbol{n}(\boldsymbol{x}_i)$ is determined by the distribution of fluid particles as follows [174]:

$$\boldsymbol{n}(\boldsymbol{x}_i) = \int \frac{\boldsymbol{x}_i - \boldsymbol{x}'}{|\boldsymbol{x}_i - \boldsymbol{x}'|} W(\boldsymbol{x}_i - \boldsymbol{x}', h) \mathrm{d}\boldsymbol{x}' \simeq \sum_j \frac{m_j}{\rho_j} \frac{\boldsymbol{x}_i - \boldsymbol{x}_j}{|\boldsymbol{x}_i - \boldsymbol{x}_j|} W(\boldsymbol{x}_i - \boldsymbol{x}_j, h). \tag{4.16}$$

After updating the position and the velocity from $(\boldsymbol{x}_i(t),\ \boldsymbol{v}_i(t))$ to $(\boldsymbol{x}_i^*,\ \boldsymbol{v}_i^*)$ according to Eqs. (4.1) and (4.2), we apply the following particle shifting method:

$$\boldsymbol{x}_i(t + \Delta t) = \boldsymbol{x}_i^* + \Delta \boldsymbol{x}_i, \tag{4.17}$$

$$\boldsymbol{v}_i(t + \Delta t) = \boldsymbol{v}_i^* + \Delta \boldsymbol{x}_i \cdot \nabla \boldsymbol{v}_i. \tag{4.18}$$

Eq. (4.18) can be derived by Taylor expansion of the velocity $\boldsymbol{v}(\boldsymbol{x}_i + \Delta \boldsymbol{x}_i)$ around $\boldsymbol{x}_i$. Note that the particle shifting method does not conserve the total momentum. Nevertheless, this method is used to stabilize SPH simulations [168, 169]. Figs. 4.4 (b) and (d) show flow profiles obtained from the SPH simulations without and with the particle shifting method, respectively. As shown in Fig. 4.4 (b), fluid particles form string structures after passing through the narrow channel. Moreover, the density fluctuation is approximately 1.2%. On the other hand, as shown in Fig. 4.4 (d), we can confirm that fluid particles are well dispersed during the simulation by using the particle shifting method. Moreover, the density fluctuation is at most 0.5%.

Figs. 4.5 (a)∼(c) show (a) the x-component of velocity v_x, (b) the xy-component of the velocity gradient tensor κ_{xy}, and (c) the xx-component of the velocity gradient tensor κ_{xx}

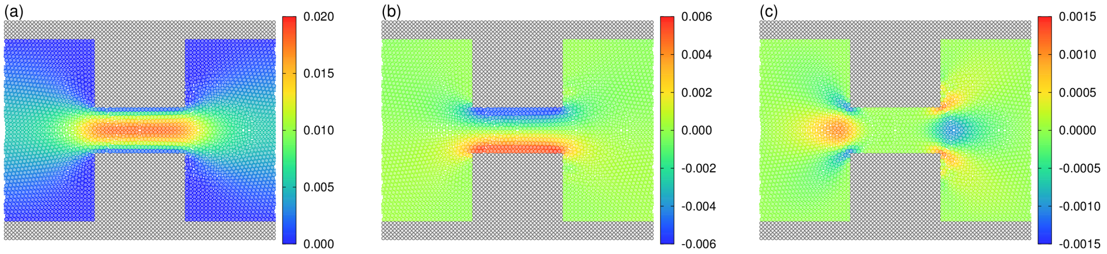

Fig. 4.5: Flow properties obtained from SPH simulations for the Newtonian fluid. (a) The x-component of velocity v_x, (b) the xy-component of the velocity gradient tensor κ_{xy}, and (c) the xx-component of the velocity gradient tensor κ_{xx}.

for the Newtonian fluid. As shown in Figs. 4.5 (a)∼(c), we can correctly capture the flow properties in the contraction-expansion channel by using the SPH with the XSPH method and the particle shifting method.

4.3 Multiscale Simulation Method

4.3.1 Bridge between Macroscopic and Microscopic Levels

In the MSS method shown in this chapter, we employ the SPH method for macroscopic fluid simulations and the Doi-Takimoto slip-link (SL) model for microscopic entangled polymer simulations. A schematic illustration is shown in Fig. 4.6. For the macroscopic level, governing equations are Eqs. (4.1), (4.2), and (4.10) described in Sec. 4.2. For the microscopic level, the SL model without SORF described in Sec. 2.2.1 is employed since polymer chain stretch is not significant in all of multi-scale simulations presented in this chapter. MSSs including polymer stretch will be investigated in a future work.

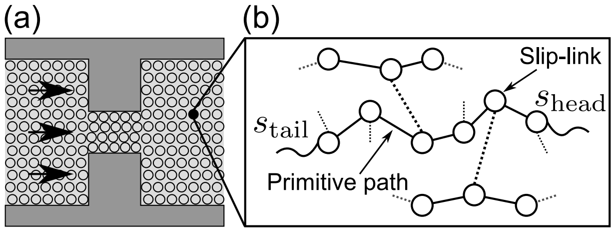

Fig. 4.6: Schematic illustration of the present MSS method for a contraction-expansion channel by using (a) SPH method and (b) the slip-link model.

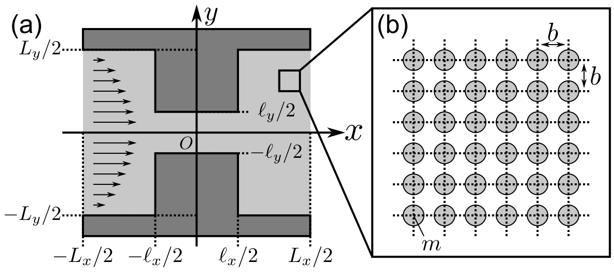

Fig. 4.7: (a) Schematic illustration of a contraction-expansion channel and (b) initial configuration for fluid particles. In (a), the origin of the coordinate is at the center of the system.

Fig. 4.7 shows (a) a flow geometry of the MSS and (b) initial configuration for fluid particles. In Fig. 4.7(b), b is the initial distance between adjacent fluid particles, which roughly corresponds to a grid interval in an Eulerian picture, and m ($= \rho_0 b^3$) is the mass of a fluid particle. Here, the masses of all fluid particles are set to be the same. The equations used in our simulations are expressed by nondimensional variables as below. At the macroscopic scale, we choose b as the unit length, m as the unit mass, τ_{e} as the unit time, and η_0/τ_{e} as the unit stress. Here, η_0 is the zero shear viscosity given by $\eta_0 = \eta_0^{(\mathrm{P})} + \eta_{\mathrm{d}}$, where $\eta_0^{(\mathrm{P})}$ is the zero shear viscosity obtained from the SL model. At the microscopic scale, we choose a as the unit length, τ_{e} as the unit time, and σ_{e} as the unit stress (for the definition of the variables, see Sec. 2.2.1). All of the variables are scaled by these units. Moreover, all the scaled variables are expressed with a tilde symbol on their top. After scaling, Eqs. (4.1) and (4.2) are rewritten as follows:

$$\frac{\mathrm{d}\tilde{\boldsymbol{x}}_i}{\mathrm{d}\tilde{t}} = \tilde{\boldsymbol{v}}_i, \tag{4.19}$$

$$\mathrm{C}_1 \frac{\mathrm{d}\tilde{\boldsymbol{v}}_i}{\mathrm{d}\tilde{t}} = \frac{1}{\tilde{\rho}_i} \Big[\widetilde{\boldsymbol{\nabla}} \cdot \Big(\widetilde{\boldsymbol{\sigma}}_i - \widetilde{P}_i^{(\mathrm{d})} \boldsymbol{I} \Big) \Big]_{\tilde{\boldsymbol{x}}_i} + \widetilde{\boldsymbol{F}}_i, \tag{4.20}$$

where C_1 ($\equiv \rho_0 b^2/\tau_{\mathrm{e}}\eta_0$) is a dimensionless parameter. Moreover, Eq. (4.3) is rewritten as follows:

$$\widetilde{\boldsymbol{\sigma}}_i = \left(\frac{\sigma_{\mathrm{e}}\tau_{\mathrm{e}}}{\eta_0} \right) \widetilde{\boldsymbol{\sigma}}_i^{(\mathrm{p})} + \mathrm{C}_2 \left(\tilde{\boldsymbol{\kappa}}_i + \tilde{\boldsymbol{\kappa}}_i^{\mathrm{T}} \right) = \frac{1 - \mathrm{C}_2}{\eta_0^{(\mathrm{P})}/(\sigma_{\mathrm{e}}\tau_{\mathrm{e}})} \widetilde{\boldsymbol{\sigma}}_i^{(\mathrm{p})} + \mathrm{C}_2 \left(\tilde{\boldsymbol{\kappa}}_i + \tilde{\boldsymbol{\kappa}}_i^{\mathrm{T}} \right) \tag{4.21}$$

where C_2 ($\equiv \eta_{\mathrm{d}}/\eta_0$) is a dimensionless parameter and is a small value in a well-entangled polymer melt. Here, we use the relation $\eta_0 = \eta_0^{(\mathrm{p})}/(1-\mathrm{C}_2)$. In the same manner, the dynamic pressure defined by Eq. (4.10) is scaled as follows:

$$\widetilde{P}_i^{(\mathrm{d})} = \mathrm{C}_3 \left(\frac{\rho_i}{\rho_0} - 1 \right), \tag{4.22}$$

where the dimensionless parameter C_3 ($\equiv c_\mathrm{s}^2 \rho_0 \tau_\mathrm{e}/\eta_0$) is related to the artificial speed of sound. The exponent γ in Eq. (4.22) is set to unity. Summarizing the above, the control parameters are C_1, C_2, C_3 and Z_0 through the scaled shear viscosity of the polymer melt $\widetilde{\eta}_0^{(\mathrm{P})}(Z_0) = \eta_0^{(\mathrm{P})}/(\sigma_\mathrm{e}\tau_\mathrm{e})$. Note that $\widetilde{\eta}_0^{(\mathrm{P})}(Z_0)$ depends only on the equilibrium number of entanglements Z_0 and is determined from the bulk SL simulation.

Our MSS method is summarized as follows:

(1) Calculate the velocity gradient tensor $\boldsymbol{\kappa}_i$ ($1 \le i \le N_\mathrm{f}$) at the position of fluid particle i using the MSPH technique. Here, N_f is the number of fluid particles.

(2) At the microscopic level, calculate polymeric stress $\boldsymbol{\sigma}_i^{(\mathrm{p})}$ in fluid particle i with the SL model using $\boldsymbol{\kappa}_i$ evaluated in item (1).

(3) Update the velocity $\boldsymbol{v}_i$ using Eq. (4.20) (MSPH).

(4) Update the position $\boldsymbol{x}_i$ using Eq. (4.19) and XSPH explained in Sec. 4.2.4.

(5) Particle shifting (see Sec. 4.2.4).

(6) Return to item (1).

4.3.2 Parameters

To determine the parameters used in the MSS, we assume that the well-entangled polymer melt is a polystyrene with a monodispersed molecular weight ($Z_0 = 7$) at a temperature of $T \simeq 200$ °C. Therefore, the density ρ_0, the unit time τ_e and the unit stress σ_e are, as an example, $\rho_0 \simeq 1.0 \times 10^3$ kg/m^3, $\tau_\mathrm{e} \simeq 1.6 \times 10^{-5}$ s and $\sigma_\mathrm{e} \simeq 5.5 \times 10^5$ Pa (where τ_e and σ_e

Table 4.1: Parameters and rheological properties of the SL model used in simulations.

Parameter	definition	value
C_1	dimensionless parameter in Eq. (4.20)	0.01
C_2	dimensionless parameter in Eq. (4.21)	0.1 [137]
C_3	dimensionless parameter in Eq. (4.22)	25
Δt	time-integral step	$0.005\tau_{\mathrm{e}}$
N_{f}	no. of fluid particles	3304
(L_x, L_y)	system size	$(80b, 56b)$
(ℓ_x, ℓ_y)	system size of a contraction region	$(28b, 14b)$
N_{p}	no. of polymer chains in a particle	1000 [146]
Z_0	equilibrium no. of entanglements	7
$\langle Z \rangle$	average no. of entanglements	8.0±2.4
τ_{d}	Reptation time	$630\tau_{\mathrm{e}}$
$\eta_0^{(\mathrm{P})}$	zero shear viscosity	$22.1\sigma_{\mathrm{e}}\tau_{\mathrm{e}}$

are evaluated by using the time-temperature superposition rule and the experimental data at $T = 160$ °C [175]). Our simulations are performed in a 4:1:4 contraction-expansion channel with a channel width, for example, $L_y = 10$ mm as shown in Fig. 4.7. Here, we assume that the width of the z-direction is infinite, and we consider a two-dimensional flow. The parameters used in the MSSs are summarized in Table 4.1. In this study, we examined flows in the following two cases, condition I: $\widetilde{\boldsymbol{F}} = (1.5 \times 10^{-4}, 0)$ and condition II: $\widetilde{\boldsymbol{F}} = (7.5 \times 10^{-4}, 0)$, where $\widetilde{\boldsymbol{F}}$ is the externally applied body force. The simulations are conducted with 48 cores (Xeon E5-2680, 2.7 GHz) and require approximately 72 hours for the system to reach a steady state.

4.4 Results and Discussion

4.4.1 Rheological properties

In Fig. 4.8, we show the rheological properties of the polymer melt $Z_0 = 7$, which are obtained from SL simulations. Before applying a strain or a strain rate, the system is fully equilibrated under $\boldsymbol{D} = \boldsymbol{0}$, namely, we equilibrate the system for a time duration that is longer than the longest relaxation time estimated in advance by the bulk SL simulation.

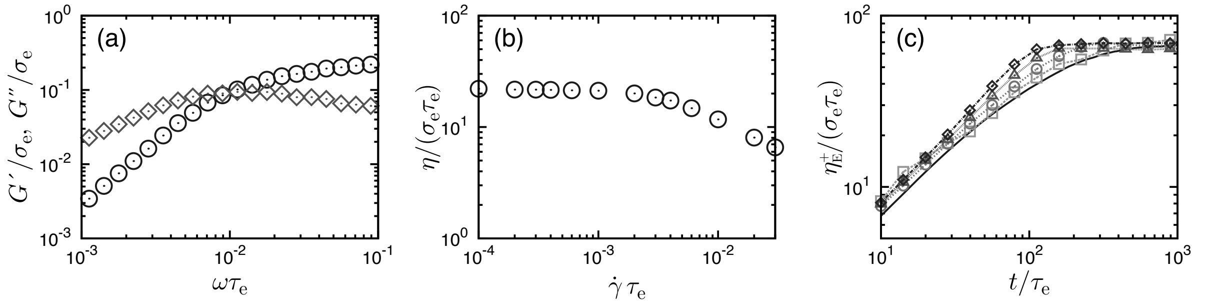

Fig. 4.8: Rheological properties of the polymer melt used in multi-scale simulations. (a) The linear viscoelasticity, (b) the steady shear viscosity and (c) the uniaxial elongational viscosities. In (a), circles are the storage modulus G' and diamonds are the loss modulus G''. In (c), the transient elongational viscosity is plotted for four different strain rates: $\dot{\epsilon}\tau_e = 1.0 \times 10^{-3}$ (square), $\dot{\epsilon}\tau_e = 5.0 \times 10^{-3}$ (circle), $\dot{\epsilon}\tau_e = 1.0 \times 10^{-2}$ (triangle), and $\dot{\epsilon}\tau_e = 1.5 \times 10^{-2}$ (diamond). The black solid line is the linear viscoelasticity growth function $3\eta_0^+(t)$.

Here, $\boldsymbol{D} \equiv (\boldsymbol{\kappa} + \boldsymbol{\kappa}^T)/2$ is the strain rate tensor. After the equilibration, the average number of entanglements $\langle Z \rangle_{eq}$ is found to be $\langle Z \rangle_{eq} \simeq 8.0$, as shown in Table 4.1. Fig. 4.8(a) shows the linear viscoelasticity data. From Fig. 4.8(a), the longest relaxation time is determined to be $\tau_d \simeq 630\tau_e$. Fig. 4.8(b) shows the steady shear viscosity plotted against various shear rates. As shown in Fig. 4.8(b), the system exhibits a shear thinning at a shear rate above approximately $\dot{\gamma}\tau_e \simeq 1.6 \times 10^{-3}$. The zero shear viscosity $\eta_0^{(p)}$ is found to be $\eta_0^{(p)} \simeq 22.1\ \sigma_e\tau_e$. Fig. 4.8(c) shows the transient uniaxial elongational viscosities $\eta_E^+(t)$ plotted against time t/τ_e for various elongational strain rates. As shown in Fig. 4.8(c), the uniaxial elongational viscosities present almost the same behavior as the linear viscoelasticity growth function $3\eta_0^+(t)$ in the low strain rate region, whereas in the high strain rate region, they are slightly larger than $3\eta_0^+(t)$. This tendency of the uniaxial elongational viscosities can also be found in the literature [67].

4.4.2 Macroscopic scale

Fig. 4.9 shows snapshots of our MSSs at four characteristic times. First, fluid particles are uniformly arranged on rectangular grid points with a spacing of b, as shown in Fig. 4.9(a). Before starting the MSSs, we equilibrate the polymer chains in each particle for a longer time

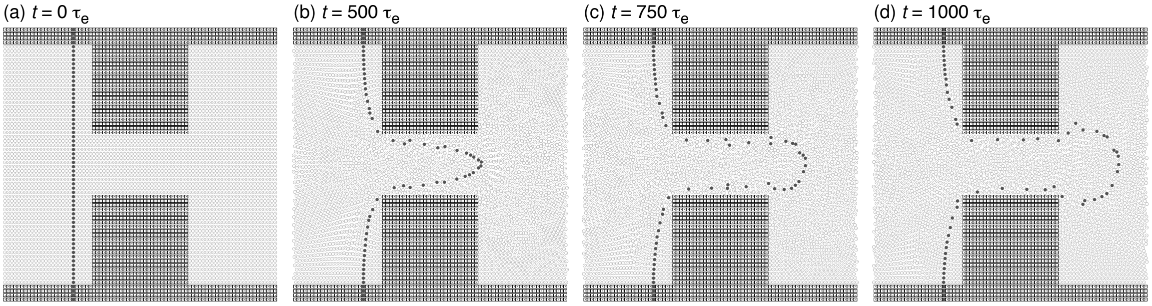

Fig. 4.9: Flow profiles obtained from the multi-scale simulation at four typical times: (a) $t/\tau_\mathrm{e} = 0$, (b) 500, (c) 750 and (d) 1000.

than the reptation time τ_d ($\simeq 630\tau_\mathrm{e}$), specifically for a time duration of $\Delta T_\mathrm{eq} = 1500\ \tau_\mathrm{e}$, and then we apply the external force $\widetilde{\boldsymbol{F}}$ to start the MSSs. From Figs. 4.9(b), (c) and (d), we can confirm that fluid particles are well dispersed during the simulation. The density fluctuation is at most 0.09% for condition I and 0.3% for condition II, which means that the density fluctuation can be sufficiently suppressed (*i.e.*, less than 1%) by Eq. (4.22) and the particle shifting method.

The macroscopic flow reaches a steady state after $1000\tau_\mathrm{e}$. To reduce the noise of the data, the values obtained from the MSSs are averaged over the time duration from $t = 1000\tau_\mathrm{e}$ to $t = 1500\tau_\mathrm{e}$. For the macroscopic properties in the steady state, Fig. 4.10 shows the spatial distributions of the magnitude of (a) velocity $|\boldsymbol{v}|/(b/\tau_\mathrm{e})$, (b) the shear-deformation-based Weissenberg number $\mathrm{Wi}_\mathrm{d}^{(\mathrm{s})} \equiv |D_{xy}|\tau_\mathrm{d}$, (c) the planar elongational-deformation-based Weissenberg number $\mathrm{Wi}_\mathrm{d}^{(\mathrm{e})} \equiv |D_{xx}|\tau_\mathrm{d}$, and (d) the principal stress difference [103] PSD $\equiv |\lambda_1 - \lambda_2| = \sqrt{4\sigma_{xy}^2 + N_1^2}$ for conditions I (upper panels) and II (lower panels). Here, N_1 is the first normal stress difference, and λ_1 and λ_2 ($\lambda_1 > \lambda_2$) are the eigenvalues of the stress tensor. In (d), the arrows show the eigenvectors $\boldsymbol{x}_{\lambda_1}$ that belong to the larger eigenvalues. The directions of arrows are defined to satisfy $\boldsymbol{x}_{\lambda_1} \cdot \mathbf{e}_x > 0$ ($\mathbf{e}_x = (1, 0)$). Note that the scales of the color bars for (a), (b) and (d) are different between conditions I and II. In condition I, the local Weissenberg numbers are smaller than unity ($\mathrm{Wi}_\mathrm{d}^{(\mathrm{s})} \lesssim 1$) in almost the entire region. Therefore, the flow in condition I is close to a Newtonian flow. In condition II, however, as expected from Fig. 4.10(II-a), the velocity gradient tensor becomes large in a narrow channel

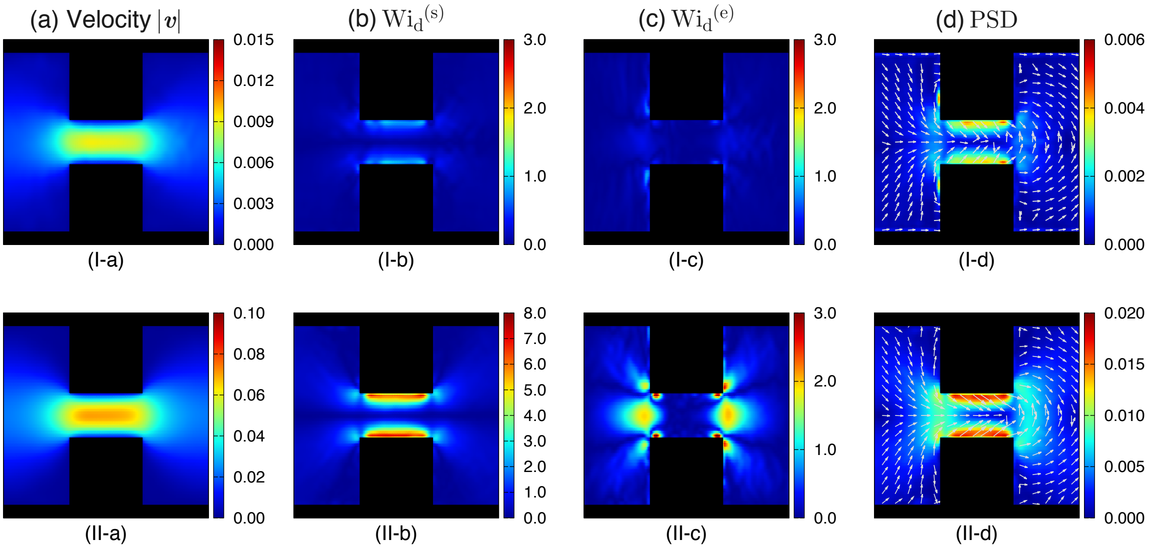

Fig. 4.10: Macroscopic flow properties obtained from the multi-scale simulation for condition I (upper panels) and condition II (lower panels). (a) Magnitudes of velocity, (b) the shear-deformation-based Weissenberg number, (c) the elongational-deformation-based Weissenberg number and (d) the principal stress difference. In (d), the arrows show the eigenvectors that belong to the larger eigenvalues, and the lengths of the arrows show the magnitude of the eigenvalues. The directions of the arrows are the same as the direction of the flow.

region. In Fig. 4.10(II-b), we can observe the region of $\mathrm{Wi_d^{(s)}} > 1$, particularly near the wall of the narrow channel region. Moreover, planar elongational flows can be observed in the region of the inlet and outlet, as shown in Fig. 4.10(II-c). The Weissenberg number related to the chain stretch or compression $\mathrm{Wi_R^{(e)}} \equiv |D_{xx}|\tau_\mathrm{R}$ is still smaller than unity. Therefore, polymer chains show almost no stretching during the planar elongational flow. Flows showing $\mathrm{Wi_R^{(e)}} > 1$ (including flow instabilities) will be investigated in a future work. As shown in Fig. 4.10(II-d), the principal stress difference PSD becomes large mainly in the following two regions: (i) near the wall of the narrow channel region and (ii) around the inlet and the outlet. The former (i) arises from the large values of shear stress σ_{xy} in response to the shear flow, as shown in Fig. 4.10(II-b). Conversely, the latter (ii) arises from large values of N_1 in response to the planar elongational flow, as shown in Fig. 4.10(II-c). Moreover, the directions of the eigenvectors are changed to reflect the flow field (as shown in Fig. 4.12).

For a more quantitative analysis, we show the physical quantities along the centerline

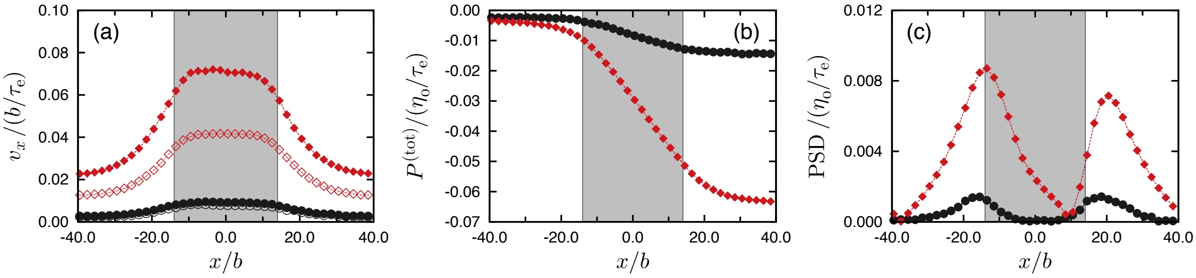

Fig. 4.11: The macroscopic variables along the center line ($y = 0$) for condition I (black circle) and condition II (red diamond). Closed symbols show the results obtained by the multi-scale simulation using the SL model. Open symbols show the results obtained by the Newtonian fluid having a shear viscosity that is the same as the zero shear viscosity η_0. (a) The x component of the velocity, v_x, (b) the total pressure and (c) the principal stress difference. The shaded region represents the narrow channel region.

in Fig. 4.11. The shaded region represents the narrow channel region ($-\ell_x/2 < x < \ell_x/2$, $\ell_x = 28b$). In Fig. 4.11, the standard deviations of each macroscopic data point are less than the sizes of the symbols. Fig. 4.11(a) shows the x-component of the velocity, v_x, along the center line $y = 0$ (filled symbol: the polymer melt flow with $Z_0 = 7$; open symbol: the flow of the Newtonian fluid with the shear viscosity η_0). As shown in Fig. 4.11(a), the x-component of the velocity in condition I is almost the same profile as that of the Newtonian flow, which is consistent with $\mathrm{Wi}_\mathrm{d}^{(\mathrm{s})} \lesssim 1$ in almost the entire region. Conversely, the x-component of the velocity in condition II is larger than that of the Newtonian flow. This result can be understood by the shear thinning effect that starts to work mainly near the wall of the narrow channel region, as expected from Fig. 4.8(b). Fig. 4.11(b) shows the total pressure $P^{(\mathrm{tot})} \equiv P^{(\mathrm{d})} + P^{(\mathrm{h})}$ along the center line $y = 0$. Here, $P^{(\mathrm{d})}$ is the dynamic pressure that is defined by Eq. (4.10), and $P^{(\mathrm{h})}$ is the hydrostatic pressure that corresponds to the externally applied body force $\boldsymbol{F}$ ($= (1/\rho)\nabla P^{(\mathrm{h})}$) [166]. As shown in Fig. 4.11(b), the pressure along the center line steeply decreases in the narrow channel region. This nonlinear pressure profile was also observed in a previous study (see Fig. 7 in Ref. [102]). Fig. 4.11(c) shows the principal stress difference PSD along the center line $y = 0$. In condition I, the principal stress difference PSD profile is almost symmetric with respect to the vertical center line $x = 0$. This behavior is consistent with that of the corresponding Newtonian flow. Conversely, in condition II, the principal stress difference PSD shows an asymmetric profile. This result is in qualitative agreement with a previous study; that is, the PSD along the centerline has two peaks. One peak is near the entrance of the narrow channel region, and the other peak is slightly behind the exit of the narrow channel region (see, for example, Fig. 7 in Ref. [105]). However, the magnitude of the PSD depending on the positions along the centerline is not in quantitative agreement because the materials used in reference [105] and the flow channel geometry are different from those in this study. Note that the decrease in PSD in the vicinity of the position $x \simeq -40b$ results from the periodic boundary condition. The polymer chains almost relax at the position $x \simeq 40b$, although the effect of the periodic boundary condition slightly remains. Further study including the dependence of system geometry and system size is needed.

4.4.3 Microscopic scale

We now focus on microscopic information that is unique to our MSS. A priori, one might expect that the entanglement structure obtained from the MSS will depend on particular model used to account for the effect of entanglements. If this were the case, the purpose and the meaning of the analysis that follows might be questioned. Therefore, we have compared two relevant entanglement characteristics of our SL model with those of other models from the literature [66, 76, 80]. For the conditions relevant to the present work, we found that the entanglement characteristics of our SL model and the other models considered were essentially identical. Armed with this agreement, we proceed with our analysis of the entanglement structure of our SL model as seen during the MSS simulations.

Fig. 4.12 shows (a) the effective strain rate $\dot{\gamma} \equiv \sqrt{\boldsymbol{D} : \boldsymbol{D}}$ and (b) snapshots of the superimposed conformation of all of the polymer chains for eight typical points: (i) $(x, y) = (-30b, 0)$, (ii) $(-15b, 0)$, (iii) $(0, 0)$, (iv) $(15b, 0)$, (v) $(-14b, -7b)$, (vi) $(0, -7b)$, (vii) $(14b, -7b)$ and (viii) $(20b, -7b)$ at $t = 1500\tau_{\mathrm{e}}$ in condition II. In figures (b-(i))–(b-(viii)), the center of mass of the polymer chain is fixed at the origin, and the x-axis and y-axis are scaled by the equilibrium

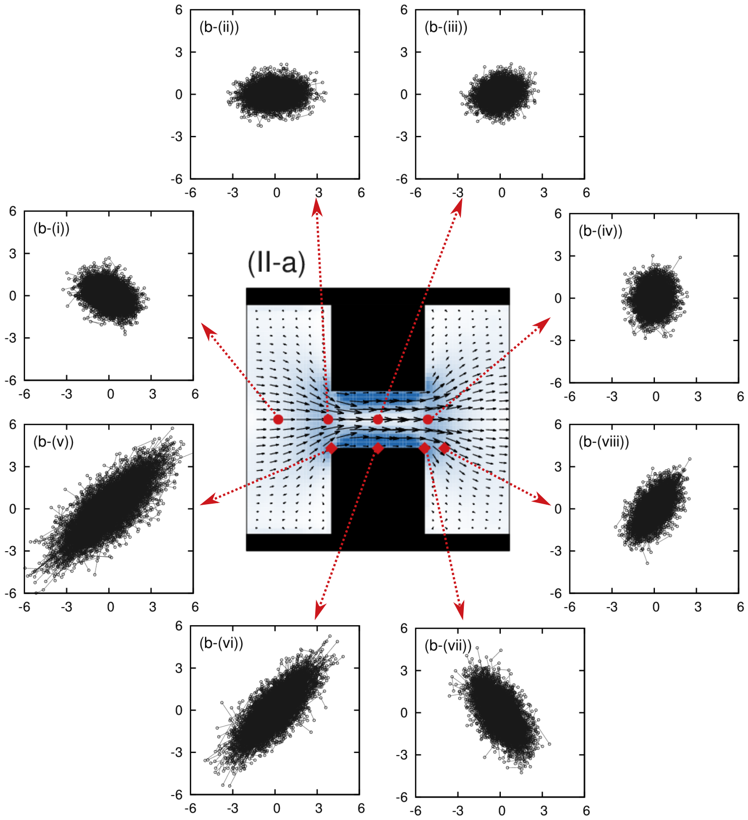

Fig. 4.12: (a) The effective strain rate $\dot{\gamma}\tau_{\mathrm{e}} \equiv \sqrt{\boldsymbol{D} : \boldsymbol{D}}$ and (b) snapshots of the superimposed conformation of all of the polymer chains for eight typical points: (i) $(x, y) = (-30b, 0)$, (ii) $(-15b, 0)$, (iii) $(0, 0)$, (iv) $(15b, 0)$, (v) $(-14b, -7b)$, (vi) $(0, -7b)$, (vii) $(14b, -7b)$ and (viii) $(20b, -7b)$ at $t = 1500\tau_{\mathrm{e}}$ in condition II. In (a), the background color map shows the effective strain rate $\dot{\gamma}$, and the arrows show the velocity field. Here, the arrows are magnified by 125. In (b), the x-axis and y-axis are scaled by the equilibrium length between adjacent slip-links a.

length between adjacent slip-links a. The flow along the center line is dominated by the planar elongational flow. At (i) $(x, y) = (-30b, 0)$ (see Fig. 4.12(b-(i))), the polymer chains are almost relaxed. At (ii) $(-15b, 0)$ (see Fig. 4.12(b-(ii))), the polymer chains are slightly oriented to the x-direction in response to the planar elongational flow ($D_{xx} > 0$) of the inlet area, as shown in Fig. 4.10(II-c). At (iii) $(0, 0)$ (see Fig. 4.12(b-(iii))), the polymer chains are almost relaxed. Moreover, at (iv) $(15b, 0)$ (see Fig. 4.12(b-iv)), the polymer chains are slightly oriented to the y-direction in response to the planar elongational flow with $D_{xx} < 0$ and $D_{yy} > 0$ in the outlet region, as shown in Fig. 4.10(II-c). However, the flow near the wall of the narrow channel is mainly dominated by the shear flow. At (v) $(-14b, -7b)$ (see Fig. 4.12(b-(v))), the

Table 4.2: Orientation tensor at characteristic positions. Positions (i)–(viii) correspond to those in Fig. 4.12(b).

	Position		S_{xx}	S_{yy}	S_{zz}	S_{xy}	S_{yz}	S_{zx}	$\lambda_{\max}$	θ [deg.]
I	(i)	$(-30b, 0)$	0.33	0.34	0.33	-8.4×10^{-4}	4.7×10^{-3}	3.7×10^{-4}	0.34	-86.5
	(ii)	$(-15b, 0)$	0.38	0.30	0.32	1.1×10^{-2}	-2.6×10^{-3}	6.8×10^{-3}	0.38	7.2
	(iii)	$(0, 0)$	0.33	0.33	0.34	-2.1×10^{-3}	2.7×10^{-4}	-8.4×10^{-3}	0.35	-8.1
	(iv)	$(15b, 0)$	0.29	0.36	0.35	-1.5×10^{-3}	2.6×10^{-3}	-2.2×10^{-3}	0.36	-88.6
	(v)	$(-14b, -7b)$	0.43	0.34	0.23	6.0×10^{-2}	-3.7×10^{-3}	-4.9×10^{-3}	0.46	25.2
	(vi)	$(0, -7b)$	0.29	0.46	0.25	1.0×10^{-1}	-2.9×10^{-3}	-1.7×10^{-4}	0.51	65.2
	(vii)	$(14b, -7b)$	0.31	0.36	0.33	-6.2×10^{-2}	-3.6×10^{-3}	-4.1×10^{-3}	0.40	-55.3
	(viii)	$(20b, -7b)$	0.35	0.32	0.33	2.0×10^{-2}	2.5×10^{-3}	-3.3×10^{-4}	0.36	28.1
II	(i)	$(-30b, 0)$	0.38	0.29	0.33	-4.2×10^{-3}	1.9×10^{-3}	8.8×10^{-4}	0.38	-2.8
	(ii)	$(-15b, 0)$	0.52	0.20	0.28	6.6×10^{-4}	-1.1×10^{-3}	2.0×10^{-3}	0.52	0.1
	(iii)	$(0, 0)$	0.40	0.28	0.32	6.0×10^{-3}	-1.4×10^{-3}	2.2×10^{-3}	0.40	2.8
	(iv)	$(15b, 0)$	0.26	0.42	0.32	1.3×10^{-3}	-2.3×10^{-3}	2.4×10^{-4}	0.42	89.5
	(v)	$(-14b, -7b)$	0.50	0.37	0.13	2.9×10^{-1}	2.5×10^{-3}	2.0×10^{-3}	0.73	39.0
	(vi)	$(0, -7b)$	0.57	0.26	0.17	2.2×10^{-1}	-2.3×10^{-3}	5.6×10^{-4}	0.68	27.0
	(vii)	$(14b, -7b)$	0.47	0.35	0.18	-1.6×10^{-1}	-1.7×10^{-3}	6.4×10^{-4}	0.58	-34.3
	(viii)	$(20b, -7b)$	0.38	0.33	0.29	1.6×10^{-1}	1.2×10^{-3}	-1.2×10^{-3}	0.51	40.6

polymer chains are strongly oriented to the right diagonally upward direction due to the inlet flow and the shear flow near the wall. At (vi) $(0, -7b)$ (see Fig. 4.12(b-(vi))), the polymer chains are also strongly oriented to the right diagonally upward direction mainly due to the shear flow near the wall ($\mathrm{Wi}_{\mathrm{d}}^{(\mathrm{s})} \sim 7$), but the orientation direction at (vi) $(0, -7b)$ is a little bit larger than that at the steady state under the simple shear flow with $\mathrm{Wi}_{\mathrm{d}}^{(\mathrm{s})}$ at (vi), as discussed later. It should be noted that the orientation direction at (vi) is determined not by a shear flow at this position but by previously experienced shear and planar elongational flows. At (vii) $(14b, -7b)$ (see Fig. 4.12(b-(vii))), the orientation direction is changed due to the outlet flow. Moreover, at (viii) $(20b, -7b)$ (see Fig. 4.12(b-(viii))), the polymer chains orienting to the right diagonally upward direction are advected by the outlet flow, as shown in Fig. 4.12(a).

We also analyze the conformation tensor $\boldsymbol{W}$ defined by

$$W_{\alpha\beta} \equiv \left\langle \frac{1}{N_{\mathrm{p}}} \sum_{n=1}^{N_{\mathrm{p}}} R_{\alpha}^{(n)} R_{\beta}^{(n)} \right\rangle \tag{4.23}$$

where $\boldsymbol{R}^{(n)}$ is the end-to-end vector of a polymer chain n and $\langle \cdots \rangle$ is the time average. By using the conformation tensor $\boldsymbol{W}$, we introduce the orientation tensor as $\boldsymbol{S} \equiv \boldsymbol{W}/\mathrm{Tr}\boldsymbol{W}$. The maximum eigenvalue $\lambda_{\max}$ of the orientation tensor $\boldsymbol{S}$ denotes the degree of orientation. From the eigenvector that belongs to the maximum eigenvalue, $(x^{(\mathrm{P})}_{\lambda_{\max}}, y^{(\mathrm{P})}_{\lambda_{\max}}, z^{(\mathrm{P})}_{\lambda_{\max}})$, we can define the orientation direction by using the expression $\theta \equiv (180/\pi)\tan^{-1}(y^{(\mathrm{P})}_{\lambda_{\max}}/x^{(\mathrm{P})}_{\lambda_{\max}})$ $(-90^\circ \leq \theta \leq 90^\circ)$. Here, the directions of the eigenvectors are set to be the same as the direction of the flow. When the polymer chains are isotropic, the orientation tensor satisfies the relation $S_{\alpha\beta} = \delta_{\alpha\beta}/3$, the maximum eigenvalue $\lambda_{\max}$ should be 1/3, and the orientation direction θ has no specific direction. Table 4.2 shows the components of the orientation tensor, the maximum eigenvalue and the orientation direction. Positions (i)–(viii) shown in Table 4.2 correspond to those in Fig. 4.12(b). Table 4.2 quantitatively shows to what extent the polymer chains are oriented to the eigenvector direction of the maximum eigenvalue. For the components S_{yz} and S_{zx}, these values are one order or two orders of magnitude smaller than the other components. In condition I, the polymer chains along the center line $y = 0$ are almost isotropic. However, the polymer chains along the stream line near the wall of the narrow channel are slightly oriented. The tendencies of the orientation tensor in condition II are in good agreement with those in Fig. 4.12(b). At (ii) $(-15b, 0)$ and (iv) $(15b, 0)$, the polymer chains are oriented to the x-direction ($\theta \simeq 0^\circ$) and the y-direction ($\theta \simeq 90^\circ$), respectively. Moreover, along the stream line near the wall of the narrow channel, at (v) $(-14b, -7b)$ and (vi) $(0, -7b)$, the polymer chains are clearly oriented to the right diagonally upward directions ($\theta \simeq 39^\circ$ and 27°, respectively). The orientation angle at position (vi) (refer Fig. 4.12 (b-(vi))) is slightly larger than that obtained under steady simple shear flow ($\simeq 22.8^\circ$) (see supporting information if more specific information is necessary). Near the wall of the inlet of the narrow channel region, the polymer chains experience not only simple shear but also planar elongational deformation ($D_{xx} < 0$ and $D_{yy} > 0$). As the relaxation time τ_{d} is longer than the time taken to move from the entrance of the narrow channel to the position (vi), the larger orientation angle can be attributed to the residual effect of the

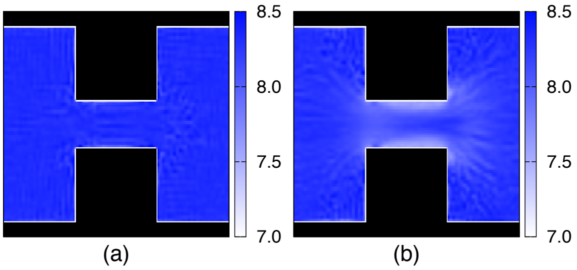

Fig. 4.13: Average number of entanglements $\bar{Z}$ obtained from the multi-scale simulation: (a) condition I and (b) condition II.

planar elongation experienced near the entrance. At (vii) $(14b, -7b)$, the orientation direction is dramatically changed to a right diagonally downward direction $\theta \simeq -34°$ according to the outlet flow. Moreover, at (viii) $(20b, -7b)$, the orientation direction is $\theta \simeq 41°$ because the oriented polymer chains are advected by the outlet flow, as observed in the velocity field shown in Fig. 4.12(a).

We evaluated the spatial distribution of the average number of entanglements on a single polymer chain, $\bar{Z}(\boldsymbol{x})$, by taking the average over all the polymer chains in fluid particles existing in a small box located at position $\boldsymbol{x}$. Fig. 4.13 shows the distribution $\bar{Z}(\boldsymbol{x})$ for (a) condition I and (b) condition II. As shown in Fig. 4.13(a), $\bar{Z}(\boldsymbol{x})$ is almost constant throughout the system in condition I, which is consistent with Figs. 4.10(I-b) and (I-c). In contrast, in condition II shown in Fig. 4.13(b), the average number of entanglements on a chain decreases, particularly in the positions where the Weissenberg number $\mathrm{Wi}_{\mathrm{d}}^{(\mathrm{s})}$ is larger than unity. This decrease in entanglements can be understood by the convective constraint release (CCR) [34] effect that strongly works at the region $\mathrm{Wi}_{\mathrm{d}}^{(\mathrm{s})} > 1$ (the polymer chains are weakly stretched in this region).

As with the macroscopic scale, we show the physical quantities along the line $y = -0.5b$ located at slightly below the center horizontal line and the line $y = -6.5b$ in Fig. 4.14. In this figure, the shaded region represents the narrow channel region. Fig. 4.14 shows (a) the Weissenberg numbers $\mathrm{Wi}_{\mathrm{d}}^{(\mathrm{e})}$ and $\mathrm{Wi}_{\mathrm{d}}^{(\mathrm{s})}$ and (b) the average number of entanglements $\bar{Z}$ on a single chain along (i) the line $y = -0.5b$ and (ii) the line $y = -6.5b$. The standard deviations

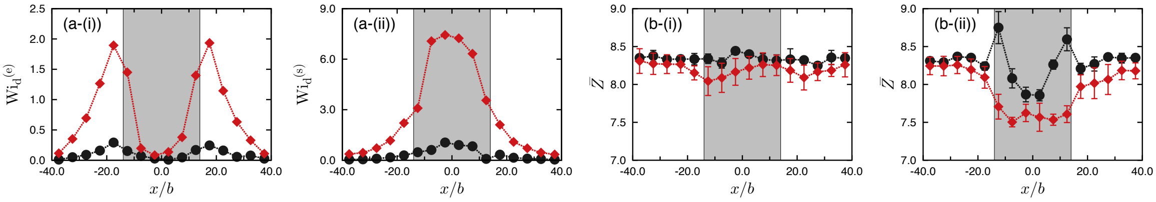

Fig. 4.14: (a) The Weissenberg numbers (i) $\mathrm{Wi}_\mathrm{d}^{(\mathrm{e})}$ and (ii) $\mathrm{Wi}_\mathrm{d}^{(\mathrm{s})}$, and (b) the average number of entanglements $\bar{Z}$ along two flow trajectories (i) along the center line ($y = -0.5b$) and (ii) along the line ($y = -6.5b$) near the wall of the narrow channel. The black circles are for condition I, and the red diamonds is for condition II. The shaded region represents the narrow channel region.

of the macroscopic data are almost the same as or less than the sizes of the symbols in Figs. 4.14(a-(i)) and (a-(ii)). However, the standard deviations of each microscopic data point are almost the same as or larger than the sizes of the symbols shown in Figs. 4.14(b-(i)) and (b-(ii)). From Fig. 4.14(a-(i)), the Weissenberg number $\mathrm{Wi}_\mathrm{d}^{(\mathrm{e})}$ reflecting the planar elongational deformation appears to be almost symmetric with respect to the vertical center line $x = 0$. However, the average number of entanglements $\bar{Z}$ of each condition shows asymmetric profiles with respect to the vertical center line $x = 0$, as shown in Fig. 4.14(b-(i)). This result occurs because the microscopic states of polymer chains such as the average number of entanglements $\bar{Z}$ on a single chain depend on the flow history. As with case (i), the average number of entanglements decreases with increasing Weissenberg number, as shown in Fig. 4.14(a-(ii)) and Fig. 4.14(b-(ii)).

Finally, to analyze the entanglements along a polymer chain in detail, we introduce the number density distribution of entanglements along a polymer chain, n. As mentioned earlier, in principle, the number density of entanglements along a polymer chain and its variation under flow may depend on the particular model. Therefore, we had compared the entanglement characteristics of our SL model to other models from the literature and found them to be essentially identical (see Appendix 4.A). In addition, even molecular models where the number density of entanglements is unchanged under flow (such as Ianniruberto-Marrucci model [176, 177], Mead-Larson-Doi model [37], Rolie-Poly model [39], etc.) can generate results similar to those presented here [108]. Be that as it may, we believe that the analysis

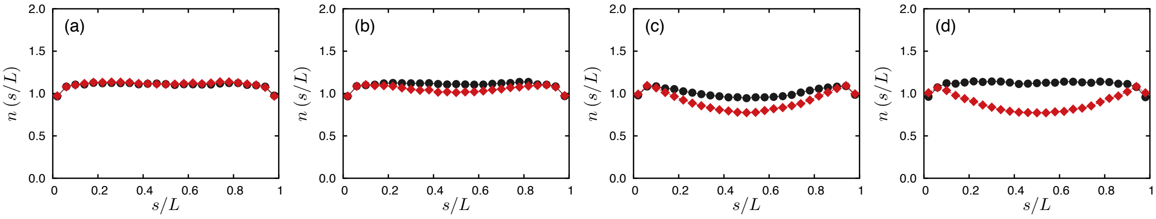

Fig. 4.15: Time-averaged number density of entanglements $n(s/L)$ at four typical positions: (a) $(x, y) = (-30b, 0)$ as a far upstream position from the inlet region, (b) $(-15b, 0)$ in the inlet region, (c) $(0, -7b)$ as a position near the wall of the narrow channel region and (d) $(14b, -7b)$ as a position in the outlet region for condition I (black circle) and condition II (red diamond).

that follows can enrich our understanding of the behavior of entangled polymer chains under flow. We calculate $n(s, t)$ as a function of internal coordinate s, which is the length along the primitive path from one end ($s = 0$) to the other ($s = L$). Polymer chains are divided into M sections (here, we employ $M = 25$) that have an interval $\Delta s = L/M$. The number density of entanglements along a polymer chain is defined as

$$n(s,t) \equiv \left\langle \frac{\Delta Z(s,t)}{\Delta s} \right\rangle, \tag{4.24}$$

where $\Delta Z(s, t)$ is the number of entanglements in the interval Δs at s and $\langle \cdots \rangle$ is the statistical average of $(\cdots)$. Moreover, the time-averaged number density of entanglements along a polymer chain is defined as $n(s) = (1/T) \int_{t_0}^{t_0+T} n(s, t)dt$, where t_0 is a time after reaching a steady state and T is the time averaging duration. By definition, $n(s)$ satisfies the relation $\int_0^L n(s)ds = \langle Z \rangle$. Fig. 4.15 shows $n(s/L)$ obtained by the MSS at four typical points: $(x, y) =$ (a) $(-30b, 0)$ as a far upstream position from the inlet region, (b) $(-15b, 0)$ in the inlet region, (c) $(0, -7b)$ near the wall of the narrow channel and (d) $(14b, -7b)$ in the outlet region for condition I (black circle) and condition II (red diamond). The quantities are averaged over the time duration from $t = 1000\tau_{\mathrm{e}}$ to $t = 1500\tau_{\mathrm{e}}$. At (a) $(-30b, 0)$ (see Fig. 4.15(a)), $n(s/L)$ is almost constant along s. At (b) $(-15b, 0)$ (see Fig. 4.15(b)), $n(s/L)$ for condition I is almost constant because of the small strain rate shown in Fig. 4.10(I-c) and Fig. 4.14(a-i). Meanwhile, $n(s/L)$ at $(-15b, 0)$ for condition II slightly decreases at

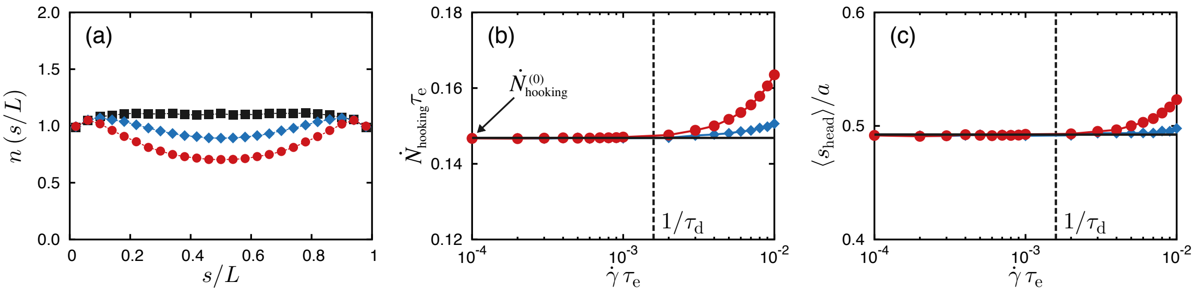

Fig. 4.16: Bulk properties obtained by SL simulations. (a) Average number density of entanglements in bulk $n(s/L)$ for a quiescent state (black square), for a steady state under a shear flow of $\dot{\gamma}\tau_{\rm e} = 1.0 \times 10^{-2}$ (blue diamond) and a steady state under an elongational flow of $\dot{\epsilon}\tau_{\rm e} = 1.0 \times 10^{-2}$ (red circle); (b) the hooking rate $\dot{N}_{\rm hooking}(\dot{\gamma})$; and (c) the average length of the chain end $\langle s_{\rm head}\rangle$. In (b) and (c), the black horizontal solid line is for a quiescent state, blue diamonds are for shear flows, red circles are for elongational flows, and black dashed line is the strain rate $1/\tau_{\rm d}$.

the position around $s/L \simeq 0.5$. This result occurs because of the planar elongational flow shown in Fig. 4.10(II-c) and Fig. 4.14(a-i). As shown in Figs. 4.15(c) and (d), $n(s/L)$ clearly decreases mainly in the middle region of the primitive path and has peaks near both ends, particularly in condition II. In these regions, $n(s/L)$ is determined by the high shear flow because the flow behavior close to the wall of the narrow channel region is mainly dominated by the shear flow, as shown in Fig. 4.10(I-b) and Fig. 4.10(II-b). The change in density near ends occurs because entanglements are created ("hooking") or removed ("dehooking") by their own motions, *i.e.*, in an *active* manner. In contrast, the change in density in the middle region occurs because entanglements in the middle region are created ("hooked by others") or removed ("the CR mechanism") only in a *passive* manner.

For a more quantitative analysis, we calculate some bulk properties. Fig. 4.16(a) shows $n(s/L)$ in bulk for a quiescent state (black square), for a shear flow (blue diamond) and for an uniaxial elongational flow (red circle). In the quiescent state, $n(s/L)$ is almost constant along s. However, $n(s/L)$ under the flows decreases in the middle region ($s/L \simeq 0.5$) of the primitive path and has peaks near both ends ($s/L \simeq 0$ and $s/L \simeq 1$). Similar results are obtained by using the SL model developed by Likhtman [71] (see Fig. 14 in Ref. [74]). Fig. 4.16(b) shows a hooking rate defined by $\dot{N}_{\rm hooking}(\dot{\gamma}) \equiv \left(1/N_{\rm p}\sum_{n=1}^{N_{\rm p}} N_{\rm hooking}(\dot{\gamma})\right)/\Delta T$ for a quiescent state (black solid line), for shear flows (blue diamond) and for uniaxial elongational flows (red circle). Here, $N_{\mathrm{hooking}}(\dot{\gamma})$ is the total number of events that create entanglements through the hooking of head and tail to other chains during a time ΔT. As shown in Fig. 4.16(b), the hooking rates under shear and uniaxial elongational flows are almost the same as that of the quiescent state in the small strain rate region. However, in the strain rate region larger than approximately $1/\tau_{\mathrm{d}}$ (vertical dashed line in Fig. 4.16(b)), the hooking rates monotonically increase. In addition, note that the dehooking rate, defined by the number of dehooking events of head and tail per time, is almost the same profile as that of the hooking rates. Fig. 4.16(c) shows the average length of the chain end $\langle s_{\mathrm{head}} \rangle$ for a quiescent state (black solid line), for shear flows (blue diamond) and for uniaxial elongational flows (red circle). As with the hooking rate case, the average lengths of the chain end monotonically increase in the strain rate region larger than approximately $1/\tau_{\mathrm{d}}$. Note that the average length of the other chain end $\langle s_{\mathrm{tail}} \rangle$ is almost the same profile as $\langle s_{\mathrm{head}} \rangle$. As shown in Fig. 4.16, the number density of entanglements along a polymer chain is deeply related to the hooking/dehooking rate. A further discussion on the relation between the number density of entanglements along a polymer chain and the hooking/dehooking rate will be presented in the next paragraph.

To clarify the reason why the number density of entanglements along a polymer chain exhibits the behaviors shown in Fig. 4.15 and Fig. 4.16, that is, has peaks near both ends under shear and elongational flows, we consider an equation that can describe the time evolution of the number density of entanglements along a polymer chain (a similar single-chain model can be found in Ref. [178]). The time evolution of the number density of entanglements along a polymer chain $n(s,t)$ can be described as

$$\frac{\partial n(s,t)}{\partial t} = -\frac{\partial J}{\partial s} + \dot{n}_{\mathrm{hooked}} + \dot{n}_{\mathrm{CR}} + \dot{n}_{\mathrm{hooking}} \tag{4.25}$$

where the first term on the right-hand side J $(= J_D + J_v)$ is the contribution of a diffusion of entanglements (J_D) and an effective advection of entanglements along the primitive path (J_v). Note that the effective advection is caused by the hooked event and the CR event (for more details, see Appendix 4.B). The second term is the contribution from gaining entanglements hooked by other polymer chains, the third term is the contribution from losing entanglements by the CR, and the last term is the contribution from gaining entanglements by the hooking event due to chain end motions. Hereafter, we consider the number density of entanglements along a polymer chain in a steady state under a strain rate $\dot{\gamma}$, $n(s)$. Moreover, we only consider the range $0 \leq s \leq L/2$ because the profile of $n(s)$ is symmetric with respect to $s = L/2$. To obtain a more detailed expression for each contribution on the right-hand side of Eq. (4.25), we make the following assumptions.

(A) The diffusion flux J_D of entanglements follows Fick's law. Moreover, the diffusion constant $D(s)$ can be written as $D(s) = D_{\mathrm{c}} + D_{\mathrm{CLF}} + D_{\mathrm{H/CR}}(s)$. Here, the first term on the right-hand side is the contribution from the reptation motion, the second term is the contribution from the CLF, and the third term is the contribution from the hooked and the CR events that are discussed later.

(B) The rate of increase of entanglements per unit length hooked by others, $\dot{n}_{\mathrm{hooked}}$, is constant along the primitive path, but the constant depends on the strain rate $\dot{\gamma}$.

(C) The rate of decrease of entanglements per unit length by the CR, $\dot{n}_{\mathrm{CR}}(s)$, is proportional to the number density of entanglements along a polymer chain at s.

(D) The hooking rate at head and tail per unit length, $\dot{n}_{\mathrm{hooking}}(s)$, depends on the strain rate, as shown in Fig. 4.16 (b).

(E) The length of a primitive path L is constant, but the constant depends on the strain rate.

From assumptions (A), (B), (C) and (D), J, $\dot{n}_{\mathrm{hooked}}$, $\dot{n}_{\mathrm{CR}}$ and $\dot{n}_{\mathrm{hooking}}$ can be written as follows:

$$J(s) = J_D + J_v = -D(s)\frac{\mathrm{d}n(s)}{\mathrm{d}s} + v(s)n(s), \tag{4.26}$$

$$\dot{n}_{\mathrm{hooked}}(s,\dot{\gamma}) \to \dot{n}_{\mathrm{hooked}}(\dot{\gamma}), \tag{4.27}$$

$$\dot{n}_{\mathrm{CR}}(s) = -\frac{1}{\tau_{\mathrm{CR}}(\dot{\gamma})}n(s) \tag{4.28}$$

and

$$\dot{n}_{\mathrm{hooking}}(s) = \frac{\dot{N}^{(0)}_{\mathrm{hooking}}}{a}\Big[\Theta\left(s_1(\dot{\gamma}) - s\right) + \Theta\left(s - s_Z(\dot{\gamma})\right)\Big] \tag{4.29}$$

where $v(s)$ is the effective advection velocity along the primitive path; $\dot{n}_{\mathrm{hooked}}(\dot{\gamma})$ and $1/\tau_{\mathrm{CR}}(\dot{\gamma})$ are positive constants depending on the strain rate; $\dot{N}^{(0)}_{\mathrm{hooking}}$ is the hooking rate in the quiescent state that can be determined by Fig. 4.16 (b); $s_1(\dot{\gamma})$ and $s_Z(\dot{\gamma})$ are the positions of the first and the *Z-th* entanglements, respectively; and $\Theta(x)$ is the step function defined as $\Theta(x) = 1$ for $x > 0$ and $\Theta(x) = 0$ otherwise. The diffusion constant arising from the hooked and the CR events $D_{\mathrm{H/CR}}(s)$ and the effective advection velocity $v(s)$ can be written as follows (for more details, see Appendix 4.B):

$$D_{\mathrm{H/CR}}(s) = \frac{\dot{N}_{\mathrm{hooking}}(\dot{\gamma})}{4}\left\{(\Delta s_{\mathrm{H}} + \Delta s_{\mathrm{CR}})\left(\frac{1}{2} - \frac{s}{L}\right)\right\}^2, \tag{4.30}$$

$$v(s) = -\dot{N}_{\mathrm{hooking}}(\dot{\gamma})(\Delta s_{\mathrm{H}} - \Delta s_{\mathrm{CR}})\left(\frac{1}{2} - \frac{s}{L}\right) \tag{4.31}$$

where Δs_{H} and Δs_{CR} are variations of the internal coordinate of a slip-link located at s per hooked event and CR event, respectively. Because the “hooked” event is related to the “hooking” event, $\dot{n}_{\mathrm{hooked}}$ and $\dot{n}_{\mathrm{hooking}}$ should satisfy the following equation:

$$\int \dot{n}_{\mathrm{hooked}} ds = \int \dot{n}_{\mathrm{hooking}} ds. \tag{4.32}$$

Using Eq. (4.32) and the relation $\dot{N}_{\text{hooking}}(\dot{\gamma}) = \int \dot{n}_{\text{hooking}} ds$, $\dot{n}_{\text{hooked}}(\dot{\gamma})$ can be written as

$$\dot{n}_{\text{hooked}}(\dot{\gamma}) = \frac{\dot{N}_{\text{hooking}}(\dot{\gamma})}{L}. \tag{4.33}$$

In addition, from the relation of $\dot{N}_{\text{hooking}}(\dot{\gamma})$ to $\dot{n}_{\text{hooking}}$ and Eq. (4.29), $\dot{N}_{\text{hooking}}(\dot{\gamma})$ can be connected to $\dot{N}^{(0)}_{\text{hooking}}$ as

$$\dot{N}_{\text{hooking}}(\dot{\gamma}) = \frac{\dot{N}^{(0)}_{\text{hooking}}}{a} \big[s_1(\dot{\gamma}) + (L - s_Z(\dot{\gamma})) \big]. \tag{4.34}$$

Using $L - s_Z(\dot{\gamma}) = s_1(\dot{\gamma})$ and the above equation, $s_1(\dot{\gamma})$ can be determined by $\dot{N}^{(0)}_{\text{hooking}}$ and $\dot{N}_{\text{hooking}}(\dot{\gamma})$ obtained from Fig. 4.16(b). Note that the obtained $s_1(\dot{\gamma})$ is found to be slightly larger than $\langle s_{\text{head}} \rangle$ in Fig. 4.16(c). Because an event of an entanglement-disappearance at both ends by the flux J is related to a CR event, $\dot{n}_{\text{CR}}$ should satisfy the equation $\int \dot{n}_{\text{CR}} ds = J(0) - J(L)$. We are now considering at a steady state the left-hand side of Eq. (4.25) $\partial n / \partial t = 0$. By integrating Eq. (4.25) along s from 0 to L and using Eq. (4.32) and the equation $\int \dot{n}_{\text{CR}} ds = J(0) - J(L)$, we can derive the relation $\int \dot{n}_{\text{CR}} ds = - \int \dot{n}_{\text{hooking}} ds$. From this relation, we have the following expression of $\dot{n}_{\text{CR}}$ as

$$\dot{n}_{\text{CR}}(s) = - \frac{\dot{N}_{\text{hooking}}(\dot{\gamma})}{Z} n(s). \tag{4.35}$$

Furthermore, a boundary condition can be determined by the relation $\int \dot{n}_{\text{hooking}} ds = -J(0) + J(L)$. Because we can have $J(0) = -J(L)$ from the symmetric nature of the density distribution with respect to $s = L/2$, the boundary condition can be obtained as $J(0) = -\dot{N}_{\text{hooking}}/2$, *i.e.*,

$$-D(0) \left. \frac{\mathrm{d}n}{\mathrm{d}s} \right|_{s=0} + v(0) n(0) = - \frac{\dot{N}_{\text{hooking}}(\dot{\gamma})}{2}. \tag{4.36}$$

We have solved Eq. (4.25) numerically by using Eqs. (4.26)–(4.36). Fig. 4.17 shows the average number densities of entanglements along a polymer chain at steady states $n(s/L)$ obtained by Eq. (4.25) for four typical non-dimensionalized parameter sets that are summa-

Table 4.3: Parameters for solving Eq. (4.25).

	$D_\mathrm{c}+D_\mathrm{CLF}$	L	Z	$\dot{N}_\mathrm{hooking}(\dot\gamma)$	Δs_H	Δs_CR
(a)	0.05	8.0	8.0	0.15	0.3	0.3
(b)	0.05	8.5	7.0	0.16	0.3	0.0
(c)	0.05	8.5	7.0	0.16	0.3	0.3
(d)	0.05	8.5	7.0	0.15	0.3	0.0

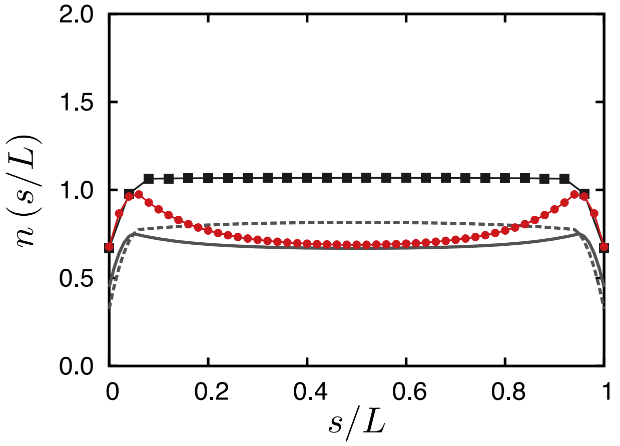

Fig. 4.17: The average number density of entanglements obtained by Eq. (4.25) for four typical parameter sets: (L, Z, $\dot{N}_\mathrm{hooking}(\dot\gamma)$, Δs_H, Δs_CR) = (a) (8.0, 8.0, 0.15, 0.3, 0.3) (black square), (b) (8.5, 7.0, 0.16, 0.3, 0.0) (red circle), (c) (8.5, 7.0, 0.16, 0.3, 0.3) (gray dashed line) and (d) (8.5, 7.0, 0.15, 0.3, 0.0) (gray solid line) with $D_\mathrm{c}+D_\mathrm{CLF}=0.05$.

rized in Table 4.3. The diffusion constant from the reptation and the CLF $D_\mathrm{c}+D_\mathrm{CLF}$ can be estimated as 0.05 by using the relations $D_\mathrm{c}\simeq L_0^2/(\pi^2\tau_\mathrm{d})$ and $D_\mathrm{CLF}\simeq a^2/(3Z_0\tau_\mathrm{e})$. Moreover, the variations of the internal coordinate Δs_H and Δs_CR can be estimated from the SL model. Here, the values of parameter sets (a) and (b) are typical ones that are obtained from the SL simulations shown in Fig. 4.16. In the quiescent state ($\dot\gamma=0$), the advection effect can be neglected ($v_\mathrm{eq}(s)=0$) because the variation in the internal coordinate of a hooked event Δs_H is the same as that of a CR event Δs_CR. Meanwhile, under a flow ($\dot\gamma\neq 0$), we should consider the advection effect ($v(s)\neq 0$) because the slip-link appears to be advected in the s-coordinate by a hooked event. In the case of parameter set (a), $n(s/L)$ is almost the same as that in the quiescent state. In the case of parameter set (b), which corresponds to the large strain rate case shown in Fig. 4.16, $n(s/L)$ decreases in the middle region ($s/L\simeq 0.5$)

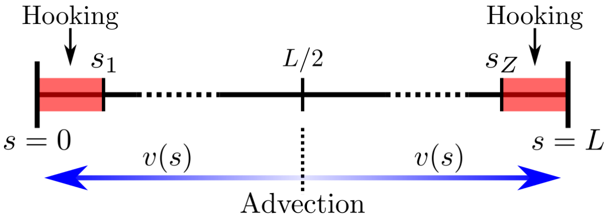

Fig. 4.18: Schematic illustration of the number density of entanglements along a polymer chain under a shear/elongational flow.

and has peaks near both ends. In the cases of parameter sets (c) and (d), which have the same length L, number of entanglements Z and Δs_{H} as parameter set (b) but have different Δs_{CR} and hooking rate $\dot{N}_{\mathrm{hooking}}(\dot{\gamma})$, respectively, although the values of $n(s/L)$ are altered, their shapes of distributions are almost the same as that in (a). Therefore, we can draw the following two points from Fig. 4.17. The first is that the height of $n(s/L)$ is mainly determined by the value of Z/L. The second is that the value of $n(s/L)$ near both ends is determined by competition between the effective advection effect at both ends and the hooking rate, as shown in Fig. 4.18.

The MSS method enables us to directly access molecular-level dynamics and macroscopic flow properties. From our MSS, we can obtain detailed microscopic information, such as the local orientation of polymer chains, the spatial distribution of the average number of entanglements and the number density of entanglements along a polymer chain as a function of the internal coordinate along the primitive path. Although further studies including comparisons with other models [48,58,75] are needed, these types of microscopic information can be useful when designing polymer melts with specific properties.

4.5 Conclusion

We have successfully applied an MSS method to flows of a well-entangled polymer melt in a contraction-expansion channel. In our MSS method, the macroscopic model based on the Lagrangian picture is combined with a microscopic model that can predict the rheological properties of well-entangled polymer melts. For the former, we employ SPH, and for the latter, we employ the SL model developed by Doi and Takimoto [67]. Using the MSS method mentioned above, we have examined flows in a contraction-expansion channel, which is one of the model flow channel geometries of polymer processing flows.

We have investigated both macroscopic and microscopic information obtained from the MSS for two different conditions. One is the condition in which the externally applied body force is small (condition I), and the other is the condition in which the force is large (condition II). In condition I, we have confirmed that the flow profile is almost the same as the Newtonian flow because the shear-deformation-based Weissenberg number $\mathrm{Wi}_{\mathrm{d}}^{(\mathrm{s})}$ is less than unity in almost the entire region. Conversely, in condition II, the Weissenberg number $\mathrm{Wi}_{\mathrm{d}}^{(\mathrm{s})}$ is partially larger than unity. Reflecting the macroscopic flow field, the states of polymer chains are different between each condition. For microscopic information, we have analyzed molecular orientations and entanglements between polymer chains in detail. In condition I, the polymer chains are weakly oriented, the average number of entanglements is almost constant, and the number density of entanglements along a polymer chain is almost the same as that in the equilibrium state. However, in condition II, the states of the polymer chains are altered mainly in the region corresponding to $\mathrm{Wi}_{\mathrm{d}}^{(\mathrm{s})} > 1$. In this region, the polymer chains are strongly oriented, and the average number of entanglements on a chain decreases. Furthermore, we have found that the number density distribution of entanglements along a polymer chain decreases in the center part on the primitive path and has peaks near the tails. To understand entanglements on a chain under flows in detail, we have developed a model equation that describes the time evolution of the number density of entanglements along a polymer chain. The model equation can successfully reproduce the profile of the number density of entanglements along a polymer chain in steady states. These types of microscopic information will provide us with new insights for the molecular design of a polymer chain.

To make the MSS method a new and effective tool for analyzing flows of polymer melts, further studies are clearly required. For example, the effects of temperature, molecular weight, molecular weight distribution, branching polymer and so on should be taken into account. Moreover, a three-dimensional simulation including comparisons with experiments is also needed. We are continuing our study to develop our MSS method along these directions, and the results will be reported elsewhere.

Appendix 4.A Microscopic Structures of the Slip-link Model

There are a lot of microscopic models with artificial entanglements that can successfully predict rheological properties [48, 58, 67–69, 71, 75]. The SL model employed in this work is a type of these microscopic models. Although the aforementioned microscopic models can successfully predict bulk rheological behavior of entangled polymer melts, it is not fully understood whether or not statistical properties of microscopic entanglement structure of these microscopic models are consistent with the results obtained from less coarse-grained simulations or theoretical studies. Here we present a short review on the works related to the entanglement structures of these microscopic models.

As for the entanglement structure at equilibrium states, Schieber theoretically derived equilibrium distribution functions for dynamic variables at a subchain level based on a free energy of a polymer chain [54]. Masubuchi *et al.* examined entangled network structure using the PCN model and compared their results with theories and less coarse-grained simulations [66]. Consequently, they concluded that the PCN model can reproduce the network structures that are consistent with less coarse-grained simulations. As for the entanglement structure under flows, Schieber reported that the average number of entanglements decreases although the distribution of the number of entanglements is almost same as that at an equilibrium state [48]. More recently, Sgouros *et al.* examined the number of entanglements under steady shear flows using the slip-spring model and compared their results with Brownian dynamics simulations and MD simulations [80]. They found that their results are in good agreement with both Brownian dynamics simulations and MD simulations.

Here, to verify validity of our SL model using in this study, we have examined of entanglement structure obtained from our SL model for two cases, (a) at equilibrium and (b) under

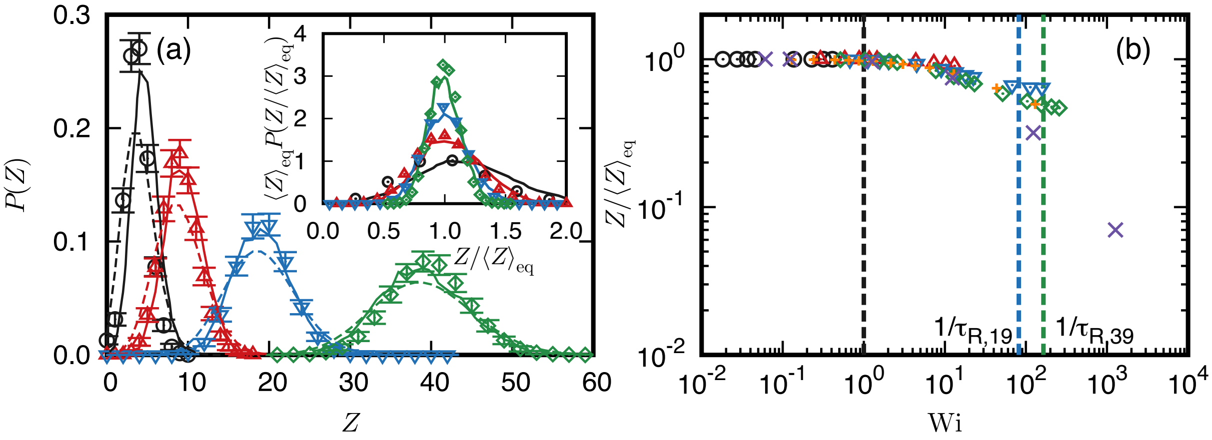

Fig. 4.19: Entanglement characteristics obtained from slip-link simulations. (a) Probability distribution of the number of slip-links per chain at equilibrium and (b) number of slip-links per chain under steady shear flow (normalized using the equilibrium value) for $\langle Z\rangle_{\text{eq}} = 4$ (circles), 9 (triangles), 19 (reverse triangles) and 39 (diamonds). In (a), the solid lines were extracted from literature [66] and the dashed lines indicate Poisson distributions with the same mean as the data. In an inset to the figure (a), the normalized probability distribution is shown. In the inset, results obtained from our SL simulations (symbols) and extracted from literature [66] (solid lines) are shown. In (b), the "×" correspond to the slip-spring model of Sgouros *et al.* [80] with $\langle Z\rangle_{\text{eq}} \simeq 19$ while the "+" correspond to the multi-chain slip-spring model of Masubuchi [76] with $\langle Z\rangle_{\text{eq}} \simeq 21$. The vertical dashed lines indicate $\dot{\gamma} = \tau_{\text{d}}^{-1}$, $\dot{\gamma} = \tau_{\text{R}}^{-1}(\langle Z\rangle_{\text{eq}} = 19)$ and $\dot{\gamma} = \tau_{\text{R}}^{-1}(\langle Z\rangle_{\text{eq}} = 39)$ from left to right.

steady simple shear flows.

First, Fig. 4.19 (a) shows distribution of the number of slip-links per chain at equilibrium. In an inset to the Fig. 4.19 (a), the normalized probability distribution $\langle Z\rangle_{\text{eq}}P(Z/\langle Z\rangle_{\text{eq}})$ is shown. Note that the value of equilibrium number of strands Z_0 is model-dependent. In general, the relation between G_0 and M_{e} is expressed as $M_{\text{e}} = A\rho RT/G_0$, where A is the model-dependent prefactor. For our SL model, A is just the same as the Doi-Edwards model [21], $A = 0.8$, whereas for the PCN model [59], $A \simeq 0.5$. This difference in A is due to the fluctuations around the entanglement point imposed in the specific model. Therefore, because of the difference of A, if we consider a certain molecular weight M, the number of entanglements Z for our SL model and that for the PCN model differ with each other. Here, we compare the statistics of the number of entanglements Z obtained from our SL model with those having the same average number of entanglements Z obtained from the PCN model.

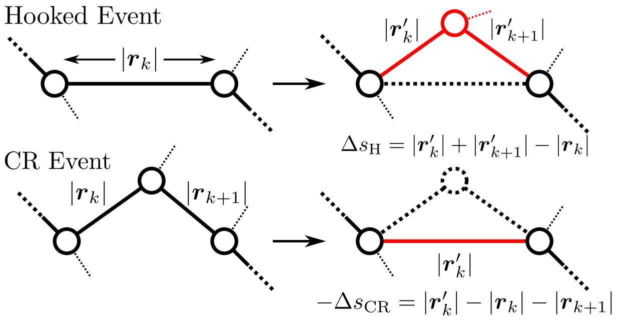

Fig. 4.20: Schematic illustration of the hooked event and the CR event in the SL model. Here, circles are the slip-links.

From Fig. 4.19 (a), it is clear that the equilibrium distributions obtained from our SL model are nearly identical to those obtained from the PCN model [66] rather than the theoretically expected Poisson distribution [48]. This is consistent with the findings in literature [66].

Second, Fig. 4.19 (b) shows normalized number of slip-links per chain ($Z/\langle Z\rangle_{\mathrm{eq}}$) under shear flows. Here, Z is the number of slip-links, $\langle Z\rangle_{\mathrm{eq}}$ is the equilibrium number of slip-links and Wi is the Weissenberg number defined as $\mathrm{Wi} \equiv \dot{\gamma}\tau_{\mathrm{d}}$. Moreover, data taken from Refs. [80] and [76] are also shown by × and + symbols, respectively. From Fig. 4.19 (b), for the strain rates examined in this work, *i.e.*, when $\dot{\gamma} \lesssim \tau_{\mathrm{R}}^{-1}$, the normalized number of slip-links from our model is essentially identical to those obtained from the slip-spring model of Sgouros *et al.* [80] and from the multi-chain slip-spring model of Masubuchi [76]. On the other hand, for $\dot{\gamma} \gtrsim \tau_{\mathrm{R}}^{-1}$, the different models clearly disagree. This disagreement is for shear rates larger than those considered in this work and hence outside the scope of our discussion.

Appendix 4.B Number Density of Entanglements

4.B.1 Hooked and CR event

In the SL model, the contour length of a primitive path changes at the same time that the hooked event or the CR event occurs, as shown in Fig. 4.20. We assume that probabilities of the hooked event $p_{\mathrm{H}}(s)$ and the CR event $p_{\mathrm{CR}}(s)$ occurring are constant, *i.e.*, $p_{\mathrm{H}}(s) = p_{\mathrm{CR}}(s) = 1/L$, where s is the internal coordinate, which is the length along the primitive path from one end ($s = 0$) to the other ($s = L$). More accurately, the probability of the CR event $p_{\mathrm{CR}}(s)$ is not constant, but it would be proportional to the number density of entanglements along a polymer chain $n(s)$. However, we consider $p_{\mathrm{CR}}(s)$ to be constant because $n(s)$ under flows does not deviate much from that in the quiescent state. Further study using MD simulations is needed to determine more reasonable assumptions for the model equation. When a hooked event occurs, the length of the primitive path locally increases by Δs_{H} (> 0). Conversely, when a CR event occurs, the length locally decreases by Δs_{CR} (> 0). Because we have assumed that the length $L(\dot{\gamma})$ is constant at the steady state under a constant strain rate (assumption (E)), we discuss three processes of recovering total length (i) after a hooked event, (ii) after a CR event in quiescent state and (iii) after a CR event under flows separately in the following sections, where we focus on a change in the local coordinate s specifying a slip-link after a hooked or a CR event occurs at s'.

4.B.2 Just after the Hooked Event

When a hooked event occurs at s', the coordinate s of a slip-link changes to $s + \Delta s_{\mathrm{H}}$ if $s > s'$, but it does not change otherwise. The changed coordinate s_{H} can be written as

$$s_{\mathrm{H}} = s\Theta(s' - s) + (s + \Delta s_{\mathrm{H}})\Theta(s - s'). \tag{4.37}$$

Here, the length of the primitive path becomes $L + \Delta s_{\mathrm{H}}$. As mentioned in assumption (E), the total length L is constant in the steady state, and the length returns to the original length L by the Rouse relaxation mechanism in Eq. (2.2). This change in length is equally allocated to the change in s_{head} and s_{tail} in the SL model. Therefore, a new coordinate $s_{\mathrm{H}}^{(\mathrm{new})}$ of the slip-link is given as

$$s_{\mathrm{H}}^{(\mathrm{new})} = s\Theta(s' - s) + (s + \Delta s_{\mathrm{H}})\Theta(s - s') - \frac{\Delta s_{\mathrm{H}}}{2}. \tag{4.38}$$

By using the probability of the hooked event occurring $p_{\mathrm{H}}(s)$, the average new coordinate $\langle s_{\mathrm{H}}^{(\mathrm{new})} \rangle$ of the slip-link having the coordinate s before the hooked event is found to be

$$\langle s_{\mathrm{H}}^{(\mathrm{new})} \rangle = \int_0^L p_{\mathrm{H}}(s') s_{\mathrm{H}}^{(\mathrm{new})} ds' = s - \Delta s_{\mathrm{H}} \left(\frac{1}{2} - \frac{s}{L} \right). \tag{4.39}$$

4.B.3 Just after the CR Event in the Quiescent State

When a CR event occurs at s' on a primitive path in the quiescent state, the coordinate s of a slip-link changes to $s - \Delta s_{\mathrm{CR}}$ if $s > s'$, but it does not change otherwise. Thus, the changed coordinate s_{CR} can be written as

$$s_{\mathrm{CR}} = s\Theta(s' - s) + (s - \Delta s_{\mathrm{CR}})\Theta(s - s'). \tag{4.40}$$

Here, the length of the primitive path becomes $L - \Delta s_{\mathrm{CR}}$. The length returns to the original length L only by the Rouse relaxation in Eq. (2.2) because there is no contribution from an affine deformation in the quiescent state. Therefore, after the change in the length, the new coordinate of the slip-link $s_{\mathrm{CR}}^{(\mathrm{new})}$ can be written as

$$s_{\mathrm{CR}}^{(\mathrm{new})} = s\Theta(s' - s) + (s - \Delta s_{\mathrm{CR}})\Theta(s - s') + \frac{\Delta s_{\mathrm{CR}}}{2}. \tag{4.41}$$

Using Eq. (4.41), the average new coordinate $\langle s_{\mathrm{CR}}^{(\mathrm{new})} \rangle$ can be obtained as

$$\langle s_{\mathrm{CR}}^{(\mathrm{new})} \rangle = \int_0^L p_{\mathrm{CR}}(s') s_{\mathrm{CR}}^{(\mathrm{new})} ds' = s + \Delta s_{\mathrm{CR}} \left(\frac{1}{2} - \frac{s}{L} \right). \tag{4.42}$$

4.B.4 Just after the CR Event under Flows

When a CR event occurs at s' on a primitive path under a flow, the coordinate s of a slip-link also changes to s_{CR} in Eq. (4.40). The length returns to the original length L mainly by a contribution of affine deformation in Eq. (2.2). Therefore, after the change in length, a new position $s_{\mathrm{CR}}^{(\mathrm{new})}$ can be written as follows:

$$s_{\mathrm{CR}}^{(\mathrm{new})} = \left[s\Theta(s'-s) + (s-\Delta s_{\mathrm{CR}})\Theta(s-s')\right]\epsilon_{\mathrm{affine}} \tag{4.43}$$

where $\epsilon_{\mathrm{affine}}$ is written as $\epsilon_{\mathrm{affine}} = L/(L-\Delta s_{\mathrm{CR}})$. Thus, we can obtain

$$\langle s_{\mathrm{CR}}^{(\mathrm{new})}\rangle = \int_0^L p_{\mathrm{CR}}(s')s_{\mathrm{CR}}^{(\mathrm{new})}ds' \simeq \left(s - \Delta s_{\mathrm{CR}}\frac{s}{L}\right)\left(1+\frac{\Delta s_{\mathrm{CR}}}{L}\right) \simeq s \tag{4.44}$$

where we neglect the higher-order contribution proportional to $(\Delta s_{\mathrm{CR}}/L)^2$ because Δs_{CR} is small compared with the length of the primitive path L ($\Delta s_{\mathrm{CR}} \ll L$).

4.B.5 Derivation of $D_{\mathrm{H/CR}}(s)$ and $v(s)$

We define the amounts of changes in coordinate δs_{H} and δs_{CR} as $\delta s_{\mathrm{H}} \equiv \langle s_{\mathrm{H}}^{(\mathrm{new})}\rangle - s$ and $\delta s_{\mathrm{CR}} \equiv \langle s_{\mathrm{CR}}^{(\mathrm{new})}\rangle - s$, respectively. When the hooked event occurs n times and the CR event occurs $(N-n)$ times, the total amount of movement $\delta S(n)$ is written as $\delta S(n) = n\delta s_{\mathrm{H}} + (N-n)\delta_{\mathrm{CR}}$. Moreover, the probability $P(n)$ can be written as $P(n) = {}_N C_n p^n q^{N-n}$, where p is the probability of occurrence of the hooked event and q $(= 1-p)$ is the probability of occurrence of the CR event. Therefore, an average amount of movement $\langle\delta S(n)\rangle$ and a variance of movement $\langle(\delta S(n) - \langle\delta S(n)\rangle)^2\rangle$ can be written as

$$\langle\delta S(n)\rangle = \sum_{n=0}^{N}\delta S(n)P(n) = N(p\delta s_{\mathrm{H}} + q\delta s_{\mathrm{CR}}) \tag{4.45}$$

and

$$\left\langle\big(\delta S(n) - \langle\delta S(n)\rangle\big)^2\right\rangle = \sum_{n=0}^{N}\big(\delta S(n) - \langle\delta S(n)\rangle\big)^2 P(n) = Npq(\delta s_{\mathrm{H}} - \delta s_{\mathrm{CR}})^2. \tag{4.46}$$

Here, the total number of hooked and CR events N can be written as $N = 2\dot{N}_{\mathrm{hooking}}(\dot{\gamma})\Delta t$ because both the hooked and CR events occur $\dot{N}_{\mathrm{hooking}}(\dot{\gamma})$ times per unit time. Furthermore, the probabilities of occurrence of the hooked event p and the CR event q are equal ($p = q = 1/2$). Thus, we can obtain $D_{\mathrm{H/CR}}(s)$ and $v(s)$ as

$$D_{\mathrm{H/CR}}(s) \equiv \frac{\left\langle \left(\delta S(n) - \langle \delta S(n) \rangle\right)^2 \right\rangle}{2\Delta t} = \frac{\dot{N}_{\mathrm{hooking}}(\dot{\gamma})}{4}(\delta s_{\mathrm{H}} - \delta s_{\mathrm{CR}})^2 \tag{4.47}$$

and

$$v(s) \equiv \frac{\langle \delta S(n) \rangle}{\Delta t} = \dot{N}_{\mathrm{hooking}}(\dot{\gamma})(\delta s_{\mathrm{H}} + \delta s_{\mathrm{CR}}). \tag{4.48}$$

By substituting Eq. (4.39) and Eq. (4.42) or (4.44) for Eqs. (4.47) and (4.48), we can obtain Eqs. (4.30) and (4.31). In the quiescent state, the variation of the internal coordinate by the hooked event Δs_{H} is the same as that by the CR event Δs_{CR} because there is no contribution from affine deformations. Therefore, the advection term $v_{\mathrm{eq}}(s)$ is equal to zero. However, under flows, we should take the effective advection term into account because $v(s)$ is not equal to zero but negative in $s < L/2$ due to $\Delta s_{\mathrm{H}} > \Delta s_{\mathrm{CR}}$ (From Eq. (4.44), we can regard Δs_{CR} as zero for convenience). Namely, the slip-link appears to be advected in the s-coordinate by hooked events.

Appendix 4.C Analytical Solution of $n(s)$ in a Steady State

We consider only the range $0 \leq s \leq L/2$ because the profile of $n(s)$ is symmetric with respect to $s = L/2$. From Eqs. (4.30) and (4.31), the spatial averages of the diffusion constant $\overline{D}_{\mathrm{H/CR}}$ and the advection velocity $\overline{v}$ can be written as

$$\overline{D}_{\mathrm{H/CR}} \equiv \frac{1}{L}\int_0^L D_{\mathrm{H/CR}}(s)ds = \frac{\dot{N}_{\mathrm{hooking}}(\dot{\gamma})}{48}(\Delta s_{\mathrm{H}} + \Delta s_{\mathrm{CR}})^2 \tag{4.49}$$

and

$$\overline{v} \equiv \frac{2}{L}\int_0^{L/2} v(s)ds = -\frac{\dot{N}_{\mathrm{hooking}}(\dot{\gamma})}{4}(\Delta s_{\mathrm{H}} - \Delta s_{\mathrm{CR}}). \tag{4.50}$$

By using Eqs. (4.49) and (4.50), Eq. (4.25) is reduced to

$$\overline{D}\frac{\mathrm{d}^2 n(s)}{\mathrm{d}s^2} - \overline{v}\frac{\mathrm{d}n(s)}{\mathrm{d}s} - \frac{\dot{N}_{\mathrm{hooking}}(\dot{\gamma})}{Z}n(s) = -E_i \quad (i = 1, 2) \tag{4.51}$$

with

$$E_1 = \frac{\dot{N}_{\mathrm{hooking}}(\dot{\gamma})}{L} + \frac{\dot{N}_{\mathrm{hooking}}(0)}{a} \; (0 \le s < s_1), \tag{4.52}$$

$$E_2 = \frac{\dot{N}_{\mathrm{hooking}}(\dot{\gamma})}{L} \qquad (s_1 \le s \le \frac{L}{2}), \tag{4.53}$$

where $\overline{D}$ is the average diffusion constant that can be written as $\overline{D} = D_{\mathrm{c}} + D_{\mathrm{CLF}} + \overline{D}_{\mathrm{H/CR}}$. The boundary conditions can be written as

$$-\overline{D}\left.\frac{\mathrm{d}n}{\mathrm{d}s}\right|_{s=0} + \overline{v}n(0) = -\frac{\dot{N}_{\mathrm{hooking}}(\dot{\gamma})}{2}, \tag{4.54}$$

$$\left.\frac{\mathrm{d}n}{\mathrm{d}s}\right|_{s=L/2} = 0, \tag{4.55}$$

$$n_1(s_1) = n_2(s_1) \tag{4.56}$$

and

$$\left.\frac{\mathrm{d}n_1}{\mathrm{d}s}\right|_{s=s_1} = \left.\frac{\mathrm{d}n_2}{\mathrm{d}s}\right|_{s=s_1} \tag{4.57}$$

where $n_1(s)$ and $n_2(s)$ are the average number densities in the ranges $0 \le s < s_1$ and $s_1 \le s \le L/2$, respectively. Using Eqs. (4.51)–(4.53) with B.C.'s (4.54)–(4.57), analytical solutions can be obtained as

$$n_i(s) = A_+^{(i)}\mathrm{e}^{\alpha_+ s} + A_-^{(i)}\mathrm{e}^{\alpha_- s} + F_i \quad (i = 1, 2) \tag{4.58}$$

with

$$F_1 = \frac{Z}{a}\left(\frac{\dot{N}_{\text{hooking}}(0)}{\dot{N}_{\text{hooking}}(\dot{\gamma})} + \frac{a}{L}\right), \quad F_2 = \frac{Z}{L} \tag{4.59}$$

and

$$\alpha_\pm = \frac{1}{2}\left(\frac{\overline{v}}{\overline{\overline{D}}} \pm \sqrt{\left(\frac{\overline{v}}{\overline{\overline{D}}}\right)^2 + \frac{4\dot{N}_{\text{hooking}}(\dot{\gamma})}{\overline{\overline{D}}Z}}\right). \tag{4.60}$$

The constants $A_+^{(i)}$, $A_-^{(i)}$ are determined as follows:

$$A_\pm^{(1)} = \frac{\pm 1}{H_\pm I}\left(G\frac{\mathrm{e}^{\alpha_\mp s_1}}{H_\mp}\left(\frac{K}{N}\alpha_\mp - 1\right) - F_{12}\right), \tag{4.61}$$

$$A_\pm^{(2)} = \frac{\mp 1}{NI\alpha_\pm \mathrm{e}^{\alpha_\pm L/2}}\left(G\cdot O + MF_{12}\right) \tag{4.62}$$

with

$$F_{12} = F_1 - F_2, \tag{4.63}$$

$$G = \frac{\dot{N}_{\text{hooking}}(\dot{\gamma})}{2\overline{\overline{D}}} + F_1\frac{\overline{v}}{\overline{\overline{D}}}, \tag{4.64}$$

$$H_\pm = \alpha_\pm - \frac{\overline{v}}{\overline{\overline{D}}}, \tag{4.65}$$

$$I = J - \frac{KM}{N}, \tag{4.66}$$

$$J = \frac{\mathrm{e}^{\alpha_+ s_1}}{H_+} - \frac{\mathrm{e}^{\alpha_- s_1}}{H_-}, \tag{4.67}$$

$$K = \frac{\mathrm{e}^{\alpha_+(s_1 - L/2)}}{\alpha_+} - \frac{\mathrm{e}^{\alpha_-(s_1 - L/2)}}{\alpha_-}, \tag{4.68}$$

$$M = \frac{\alpha_+\mathrm{e}^{\alpha_+ s_1}}{H_+} - \frac{\alpha_-\mathrm{e}^{\alpha_- s_1}}{H_-}, \tag{4.69}$$

$$N = \mathrm{e}^{\alpha_+(s_1 - L/2)} - \mathrm{e}^{\alpha_-(s_1 - L/2)}, \tag{4.70}$$

$$O = \frac{\mathrm{e}^{(\alpha_+ + \alpha_-)s_1}\left(\alpha_+ - \alpha_-\right)}{H_+ H_-}. \tag{4.71}$$

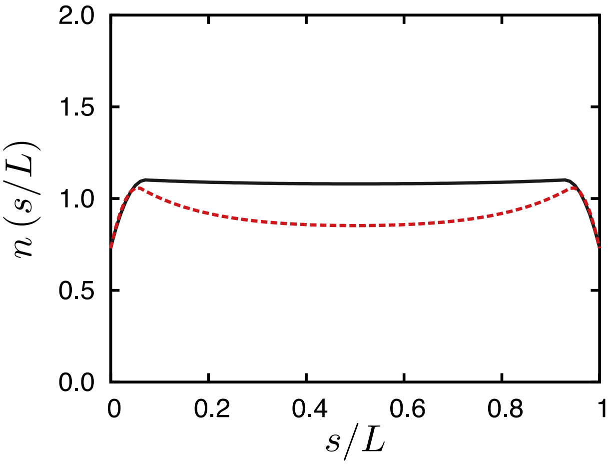

Fig. 4.21: The average number densities of entanglements in steady states obtained by Eq. (4.58) for two typical parameter sets: (L, Z, $\dot{N}_{\text{hooking}}(\dot{\gamma})$, $\overline{v}$, $\overline{D}$) = (a) (8.0, 8.0, 0.15, 0.0, 0.05) (black solid line) and (b) (8.5, 7.0, 0.16, 0.01, 0.05) (red dashed line).

Fig. 4.21 shows the average number density of entanglements along a polymer chain $n(s/L)$ in the steady state obtained by using Eq. (4.58) for two typical parameter sets: (L/a, Z, $\dot{N}_{\text{hooking}}(\dot{\gamma})/\tau_{\text{e}}^{-1}$, $\overline{v}/(a\tau_{\text{e}}^{-1})$, $\overline{D}/(a^2\tau_{\text{e}}^{-1})$) = (a) (7.0, 7.5, 0.15, 0.0, 0.05) (black solid line) and (b) (8.5, 7.0, 0.16, −0.01, 0.05) (red dashed line). These two cases correspond to steady states (a) in quiescent and (b) under a flow. We can observe that the profile of $n(s/L)$ is in qualitative agreement with that in Fig. 4.15.

Appendix 4.D Static Structure Factor

Experimentally, microscopic information of polymer chains under flows is measured using scattering experiments. For flows of monodisperse linear entangled polymer melts in the contraction-expansion channel, there are several experimental studies using a small angle neutron scattering (SANS) technique [106, 108, 110]. In these studies, molecular structure under nonlinear flows was investigated through SANS measurements for several monodisperse linear entangled polystyrene melts with different molecular weights. In the Refs. [108, 110], the scattering intensity along the centerline [108] and near the re-entrant corners [110] of the 4:1:4 contraction-expansion channel has been examined.

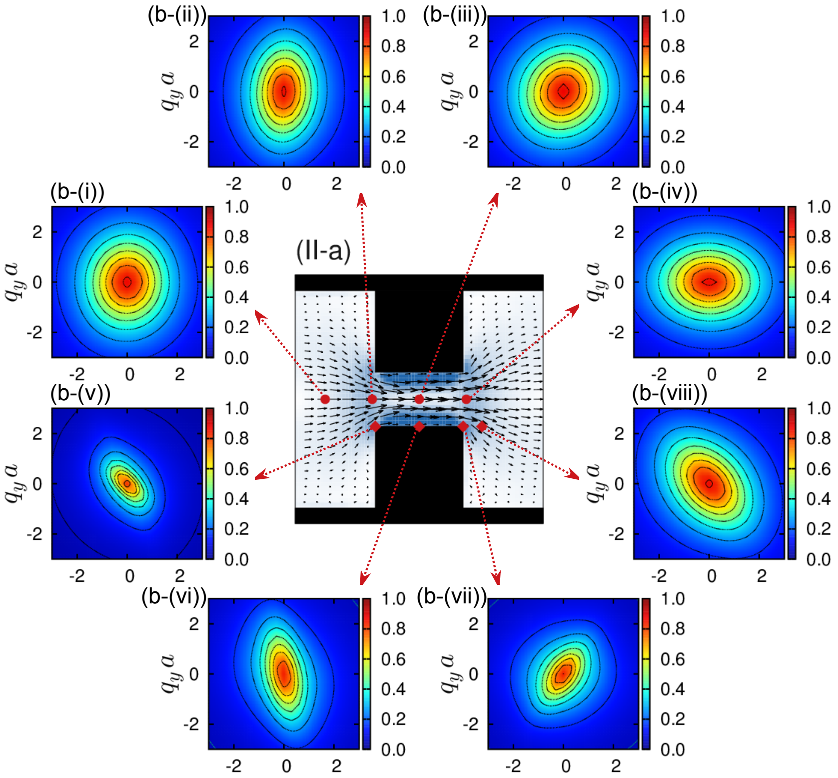

Fig. 4.22: (a) The effective strain rate $\dot{\gamma}\tau_{\mathrm{e}} \equiv \sqrt{\boldsymbol{D}:\boldsymbol{D}}$ and (b) static structure factor $S(\boldsymbol{k})$ for eight typical points: (i) $(x, y) = (-30b, 0)$, (ii) $(-15b, 0)$, (iii) $(0, 0)$, (iv) $(15b, 0)$, (v) $(-14b, -7b)$, (vi) $(0, -7b)$, (vii) $(14b, -7b)$ and (viii) $(20b, -7b)$ in condition II. In (a), the background color map shows the effective strain rate $\dot{\gamma}$, and the arrows show the velocity field. Here, the arrows are magnified by 125. In (b), the x-axis and y-axis are scaled by the equilibrium length between adjacent slip-links a, and each value of the static structure factor $S(\boldsymbol{k})$ is obtained by averaging over 20 data at different times.

From SANS experiments, the single-chain structure factor $S(\boldsymbol{k})$ can be obtained. In our MSSs, the single-chain structure factor can be calculated from the positions of the slip-links using Eq. (2.13) (for more detail, please see Appendix 2.C). Fig. 4.22 shows the single-chain structure factor obtained from our MSS simulations. These results are in qualitative agreement with previous studies [108, 110]. The SANS measurement is a powerful technique that can obtain information on microscopic molecular structure of polymer chains. Therefore, we can directly compare our results at the microscopic level with experimental results if we consider the same conditions (such as the molecular weight of the polymer melt, the flow rates, and the channel geometry) as those in experiments. Since these conditions must be carefully considered, we will make a quantitative comparison on the single-chain structure factor in our future work.

5 Concluding Remarks

5.1 Summary

In this dissertation, transport phenomena of entangled polymer melts were investigated from both macroscopic and microscopic viewpoints. The polymeric liquids in an entangled state is important for the polymer industry because the majority of polymeric liquids are used in the entangled state. As mentioned in **Chapter 1**, designing polymer products starting from the primary structure of polymer chains is still one of the grand challenges in the field of chemical engineering due to the various time and length scales involved. From a simulation perspective, the fluid dynamics approach with phenomenological viscoelastic constitutive equations is conventionally employed to solve transport problems of entangled polymeric liquids. Using this macroscopic approach, one can access time and length scales that are suitable for polymer processing. However, this "phenomenological" approach is too coarse grained to directly access molecular-level entangled polymer dynamics. One possible approach to this problem could be obtained with a Multi-Scale Simulation (MSS) approach, where a microscopic (or mesoscopic) model for describing entangled polymer dynamics is combined with a macroscopic fluid dynamics model for solving macroscopic balance equations. To develop a further sophisticated MSS technique that can be employed to predict polymer processing flows, studies from both macroscopic and microscopic aspects are still required. A summary of the results obtained in the chapters of this dissertation is as follows.

In **Chapter 2**, viscoelastic and statistical properties of the Doi-Takimoto slip-link model (DT model) [67] were extensively examined. We confirmed that the original DT model can give good rheological predictions for the linear viscoelasticity of monodisperse linear, and symmetric star polymer melt systems by comparing with experiments. Furthermore, nonlinear rheological properties for a moderate strain rate region, where polymer chains are oriented without significant stretching ($\dot{\gamma}, \dot{\epsilon} \lesssim \tau_{\mathrm{R}}^{-1}$), were in reasonable agreement with experimental rheological data. Here, $\dot{\gamma}$ and $\dot{\epsilon}$ are the shear and elongational strain rate, respectively, and τ_{R}

is the Rouse time. However, for the chain stretching region ($\dot{\gamma}, \dot{\epsilon} \gtrsim \tau_{\mathrm{R}}^{-1}$), we recognized that the original DT model does not well-describe nonlinear rheological behavior especially under elongational flows. Therefore, to develop a more sophisticated microscopic coarse-grained model, we incorporated the concept of the stretch/orientation-induced reduction of friction (SORF), which was originally proposed by Ianniruberto *et al.* [148], with the DT model. The DT model was improved using an empirical equation of SORF, which was obtained by analyzing experimental data of the stress relaxation after cessation of transient elongational flow. In the linear region, we confirmed that the rheological behavior obtained by the DT model with and without SORF are almost the same because the effect of SORF works only when polymer chains are highly oriented and stretched. In the nonlinear region, the effect of SORF is striking, particularly under uniaxial elongational flows. The steady-state elongational viscosities without SORF show thinning behavior for $\tau_{\mathrm{d}}^{-1} \lesssim \dot{\epsilon} \lesssim \tau_{\mathrm{R}}^{-1}$ and thickening behavior for $\dot{\epsilon} \gtrsim \tau_{\mathrm{R}}^{-1}$, which is typical for entangled polystyrene (PS) solutions. Here, τ_{d} is the reptation time. However, the steady-state elongational viscosities with SORF show almost monotonic thinning behavior, which is seen in experiments of entangled PS melts. Additionally, steady elongational viscosities for an entangled symmetric star PS melt and an entangled linear polyisoprene melt were investigated. For both cases, we confirmed that the DT model with SORF can give better agreement with experimental data.

For the statistical properties of microscopic structure obtained from the DT model, we examined several microscopic variables, such as the number of slip links per chain. As a result, we found that the normalized number of slip links per chain shows nonmonotonic behavior; that is, the normalized number of slip links first decreases with the strain rate for $\tau_{\mathrm{d}}^{-1} \lesssim \dot{\gamma}, \dot{\epsilon} \lesssim \tau_{\mathrm{R}}^{-1}$, which is consistent with the results obtained from other coarse grained models [64,80], and then increases for $\dot{\gamma}, \dot{\epsilon} \gtrsim \tau_{\mathrm{R}}^{-1}$, which is inconsistent with the results from other coarse grained models. Judging from the increasing behavior of the steady-state normalized number of slip links per chain under shear and elongational flows in the region $\mathrm{Wi}_{\mathrm{R}}^{(\mathrm{s/e})} \gtrsim 1$, we concluded that the microscopic structure obtained from the current DT model for $\mathrm{Wi}_{\mathrm{R}}^{(\mathrm{s/e})} \gtrsim 1$

is questionable. Further studies are needed to clarify the origin of this behavior.

In **Chapter 3**, well-entangled polymer melt spinning processes were investigated using the MSS method. In the MSS method for the polymer melt spinning process, the macroscopic balance equations were solved using the Eulerian picture. To take the effect of the deformation history into account, a Lagrangian fluid particle approach was combined with the Eulerian picture. As a response to the local velocity gradient tensors macroscopically obtained at the positions of the fluid particles, the polymeric stress coming from the entangled polymer melt was calculated using the DT model. By use of the developed MSS method, both macroscopic and microscopic information was examined. At the macroscopic level, velocity, cross-sectional area, and tension profiles along the spinning line were successfully obtained. At the microscopic level, we focused on polymer chain orientation and entanglements obtained from the DT model. For example, we confirmed that the number of entanglements per polymer chain decreases with flow because of the convective constraint release (CCR) effect. In the CCR picture, entangled polymer chains are transiently stretched under flows, and subsequent retraction of polymer chains induces the constraint release (CR). Additionally, we calculated the number density of entanglements along a polymer chain. As a result, we found that the number of entanglements mainly decreases in a middle region on a polymer chain, and is enhanced at both ends. This information would be useful for a molecular design optimized for producing a strong fiber.

In **Chapter 4**, flows of a well-entangled polymer melt in a contraction-expansion channel, which is one of the model flow channel geometries of polymer processing flows, were investigated using the MSS method. In the MSS method presented in **Chapter 4**, a Smoothed Particle Hydrodynamics (SPH) method was combined with the DT model. In SPH, a fluid is discretized into a number of fluid particles, and physical quantities at a fluid particle position are determined using an interpolation method. In the MSS technique, instead of employing a phenomenological constitutive equation for the polymeric stress, each fluid particle has a microscopic system represented by the DT model.

We investigated both macroscopic and microscopic information obtained from the MSS. MSS simulations were performed under two different conditions by changing the external body force: one was the small body force condition, and the other was the large body force condition. Reflecting the macroscopic flow field induced by the external body force, the states of polymer chains were different between two conditions. For a clear analysis, the shear-deformation-based Weissenberg number $\mathrm{Wi}_\mathrm{d}^{(\mathrm{s})}$ was introduced. The states of the polymer chains are altered mainly in the region corresponding to $\mathrm{Wi}_\mathrm{d}^{(\mathrm{s})} > 1$. In the small body force case, since the Weissenberg number $\mathrm{Wi}_\mathrm{d}^{(\mathrm{s})}$ is less than unity in almost the entire region, macroscopic flow properties are similar to those of the Newtonian fluid, and microscopic states of polymer chains are almost isotropic. In the large body force case, since the Weissenberg number $\mathrm{Wi}_\mathrm{d}^{(\mathrm{s})}$ is larger than unity especially in the narrow channel region, the polymer chains are strongly oriented, and the average number of entanglements per chain decreases. Moreover, in $\mathrm{Wi}_\mathrm{d}^{(\mathrm{s})} > 1$, we found that the number density distribution of entanglements along a polymer chain decreases in the center part on the primitive path and has peaks near the tails. To understand distribution of entanglements on a chain under flows in detail, we developed a model equation that can describe the time evolution of the number density of entanglements along a polymer chain of the DT model. The model equation can successfully reproduce the profile of the number density of entanglements along a polymer chain in steady states. We hope that these microscopic insights during processing flows will provide us with new perspectives for the molecular design of a polymer chain, as well as enrich understanding in the field of polymer physics. However, further researches from various directions are clearly required, and some of them are described in the next section.

5.2 Future Outlooks

MSS is a promising method to analyze flow problems in the polymer industry. In addition to fundamental studies of MSS methods, some studies on the flows in polymer processing using MSS methods have also been performed. However, there are many remaining problems that should be addressed before MSS methods can be applied to industrial processes. Here, we summarize some of the remaining problems.

- In industrial processes, the polymeric liquids undergo temperature changes, which can result in crystallization or solidification. Macroscopically, there are many simulation studies that have addressed flows of polymeric liquids with temperature changes [95–98, 112, 140]. In macroscopic approaches with crystallization, the crystallization kinetics is modeled in a phenomenological manner [95–98]. Microscopically, although MD simulations would be effective in tackling problems related to polymer crystallization or solidification (for more details, please see Ref. [179] and references therein), the correlation between the macroscopic properties and microscopic states of polymer chains has not been investigated. Therefore, studies that include the role of temperature changes should be performed at both macroscopic and microscopic scales.
- Industrially, polydisperse polymer melts are used to obtain desirable properties. Namely, sourced polymers have various primary structures, such as linear and branched polymers, and additionally, they are often mixed. While such polymeric liquids are difficult to handle with present constitutive equations, some mesoscale molecular models that can address linear and branched polymers and mixtures thereof have been developed [51, 61, 62, 77]. Using these molecular-based models, polydisperse polymer melts should be considered under processing conditions in the MSS method.
- Polymeric materials containing solid particles have been used in the polymer industry because the combination of polymers and solid particles can provide specific properties that cannot be obtained from a single polymer species. However, the interaction be-

tween polymeric liquids and solid particles is not fully understood. One of the reasons for this is that the flow near solid particles is complex because it is a mixture of shear and elongational flows. Characterizing this interaction is important to accurately predict the rheological properties of suspensions, such as shear thickening in viscoelastic suspending fluids. Numerically, suspensions in a viscoelastic fluid are examined using phenomenological constitutive equations, such as the Oldroyd-B model [180, 181]. Although rheological properties can be qualitatively captured by macroscopic approaches, microscopic insights are limited depending on the employed constitutive equations. MSS approaches might be one of the candidates for unraveling the physics behind the rheological properties of suspensions. In addition, if the size of the solid particles is comparable to the characteristic length of the polymer chain, then development of a new mesoscale model is required. However, studies on developing such models have not been performed.

- MSS methods might be useful for understanding the microscopic origin of macroscopic phenomena, such as shear banding. Shear banding is observed in various complex fluids, including polymer melts, polymer solutions, and wormlike micellar solutions, and has been extensively examined from experimental, theoretical, and simulation points of view [182, 183]. In addition to accurately predicting a constitutive relation between shear stress and shear rate, one of the important aspects to predict shear banding is to incorporate the effect of the spatial concentration differences. The effect of such concentration difference has not yet been addressed in current MSS approaches, and should be considered in the future. Regarding wormlike micellar solutions, constitutive models that can capture rheological properties are not yet fully developed. Therefore, studies from a microscopic viewpoint are required.
- Recently, informatics and data-driven approaches have been applied in many fields, including materials science and chemical engineering. Combining data and statistical algorithms can be useful for developing complex predictive models. However, in the field

of polymer science, the application of this information strategy is not as advanced as that in other fields. This is obviously because the characteristics of polymeric liquids are determined by complex combinations of properties at various time and length scales. Zhao and coworkers developed a data-driven MSS method using Gaussian processes (GP) [184, 185]. In their data-driven approach, a GP regression technique is used to “learn” the constitutive relation from a small number of microscopic simulations. However, the deformation history of the polymers and the memory effects, which are important for flow problems of polymeric liquids, have not been addressed.

After solving the abovementioned problems, MSS methods can be employed for engineering applications. In the field of chemical engineering, process design has been performed using only macroscopic parameters, such as the viscosity. In the future, it will be important to design industrial processes using microscopic molecular structures as process design parameters. Regarding this point, MSS methods can provide a new perspective on transport phenomena in chemical engineering.

References

[1] Rubinstein, M.; Colby, R. H. *Polymer Physics*; Oxford University Press, 2003.

[2] Bird, R. B.; Stewart, W. E.; Lightfoot, E. N. *Transport Phenomena*; John Wiley and Sons, Inc., 2006.

[3] Larson, R. G. *Constitutive Equations for Polymer Melts and Solutions*; Butterworths Series in Chemical Engineering, 1988.

[4] Ferry, J. D. *Viscoelastic Properties of Polymers*; John Wiley and Sons, Inc., 1980.

[5] Kremer, K.; Grest, G. S. Dynamics of entangled linear polymer melts: A molecular-dynamics simulation. *Journal of Chemical Physics* **1990**, *92*, 5057–5086.

[6] Likhtman, A. E.; Sukumaran, S. K.; Ramirez, J. Linear viscoelasticity from molecular dynamics simulation of entangled polymers. *Macromolecules* **2007**, *40*, 6748–6757.

[7] Ramírez, J.; Sukumaran, S. K.; Vorselaars, B.; Likhtman, A. E. Efficient on the fly calculation of time correlation functions in computer simulations. *Journal of Chemical Physics* **2010**, *133*, 154103.

[8] Kröger, M.; Hess, S. Rheological evidence for a dynamical crossover in polymer melts via nonequilibrium molecular dynamics. *Physical Review Letters* **2000**, *85*, 1128–1131.

[9] Cao, J.; Likhtman, A. E. Simulating Startup Shear of Entangled Polymer Melts. *ACS Macro Letters* **2015**, *4*, 1376–1381.

[10] Cao, J.; Likhtman, A. E. Shear banding in molecular dynamics of polymer melts. *Physical Review Letters* **2012**, *108*, 028302.

[11] Murashima, T.; Hagita, K.; Kawakatsu, T. Elongational viscosity of weakly entangled polymer melt via coarse-grained molecular dynamics simulation. *Nihon Reoroji Gakkaishi* **2018**, *46*, 207–220.

[12] O'Connor, T. C.; Alvarez, N. J.; Robbins, M. O. Relating Chain Conformations to Extensional Stress in Entangled Polymer Melts. *Physical Review Letters* **2018**, *121*, 47801.

[13] O'Connor, T. C.; Hopkins, A.; Robbins, M. O. Stress Relaxation in Highly Oriented Melts of Entangled Polymers. *Macromolecules* **2019**, *52*, 8540–8550.

[14] Lees, A. W.; Edwards, S. F. The computer study of transport processes under extreme conditions. *Journal of Physics C: Solid State Physics* **1972**, *5*, 1921–1928.

[15] Nicholson, D. A.; Rutledge, G. C. Molecular simulation of flow-enhanced nucleation in n-eicosane melts under steady shear and uniaxial extension. *Journal of Chemical Physics* **2016**, *145*, 244903.

[16] Everaers, R.; Sukumaran, S. K.; Grest, G. S.; Svaneborg, C.; Sivasubramanian, A.; Kremer, K. Rheology and Microscopic Topology of Entangled Polymeric Liquids. *Science* **2004**, *303*, 823–827.

[17] Foteinopoulou, K.; Karayiannis, N. C.; Mavrantzas, V. G.; Kröger, M. Primitive Path Identification and Entanglement Statistics in Polymer Melts: Results from Direct Topological Analysis on Atomistic Polyethylene Models. *Macromolecules* **2006**, *39*, 4207–4216.

[18] Tzoumanekas, C.; Theodorou, D. N. Topological analysis of linear polymer melts: A statistical approach. *Macromolecules* **2006**, *39*, 4592–4604.

[19] Hsu, H. P.; Kremer, K. Primitive Path Analysis and Stress Distribution in Highly Strained Macromolecules. *ACS Macro Letters* **2018**, *7*, 107–111.

[20] De Gennes, P. G. Reptation of a polymer chain in the presence of fixed obstacles. *Journal of Chemical Physics* **1971**, *55*, 572–579.

[21] Doi, M.; Edwards, S. F. *The Theory of Polymer Dynamics*; Oxford University Press, 1986.

[22] Doi, M. Explanation for the 3.4-Power Law for Viscosity of Polymeric Liquids on the Basis of the Tube Model. *Journal of Polymer Science: Polymer Letters Edition* **1981**, *19*, 265–273.

[23] Doi, M. Explanation for the 3.4-Power Law for Viscosity of Polymeric Liquids on the Basis of the Tube Model. *Journal of Polymer Science. Part A-2, Polymer Physics* **1983**, *21*, 667–684.

[24] Klein, J. The Onset of Entangled Behavior in Semidilute and Concentrated Polymer Solutions. *Macromolecules* **1978**, *11*, 852–858.

[25] Rubinstein, M.; Colby, R. H. Self-consistent theory of polydisperse entangled polymers: Linear viscoelasticity of binary blends. *Journal of Chemical Physics* **1988**, *89*, 5291–5306.

[26] Milner, S. T.; McLeish, T. C. Parameter-free theory for stress relaxation in star polymer melts. *Macromolecules* **1997**, *30*, 2159–2166.

[27] Likhtman, A. E.; McLeish, T. C. B. Quantitative theory for linear dynamics of linear entangled polymers. *Macromolecules* **2002**, *35*, 6332–6343.

[28] Van Ruymbeke, E.; Keunings, R.; Bailly, C. Prediction of linear viscoelastic properties for polydisperse mixtures of entangled star and linear polymers: Modified tube-based model and comparison with experimental results. *Journal of Non-Newtonian Fluid Mechanics* **2005**, *128*, 7–22.

[29] Larson, R. G. Combinatorial rheology of branched polymer melts. *Macromolecules* **2001**, *34*, 4556–4571.

[30] Das, C.; Inkson, N. J.; Read, D. J.; Kelmanson, M. A.; McLeish, T. C. B. Computational linear rheology of general branch-on-branch polymers. *Journal of Rheology* **2006**, *50*, 207–235.

[31] Shchetnikava, V.; Slot, J.; Van Ruymbeke, E. Comparative analysis of different tube models for linear rheology of monodisperse linear entangled polymers. *Polymers* **2019**, *11*.

[32] Shchetnikava, V.; Slot, J.; Van Ruymbeke, E. A comparison of tube model predictions of the linear viscoelastic behavior of symmetric star polymer melts. *Macromolecules* **2014**, *47*, 3350–3361.

[33] Wang, Z.; Chen, X.; Larson, R. Comparing tube models for predicting the linear rheology of branched polymer melts. *Journal of Rheology* **2010**, *54*, 223–260.

[34] Marrucci, G. Dynamics of entanglements: A nonlinear model consistent with the Cox-Merz rule. *Journal of Non-Newtonian Fluid Mechanics* **1996**, *62*, 279–289.

[35] Mead, D. W.; Leal, L. G. The reptation model with segmental stretch - I. Basic equations and general properties. *Rheologica Acta* **1995**, *34*, 339–359.

[36] Mead, D. W.; Yavich, D.; Leal, L. G. The reptation model with segmental stretch - II. Steady flow properties. *Rheologica Acta* **1995**, *34*, 360–383.

[37] Mead, D. W.; Larson, R. G. A Molecular Theory for Fast Flows of Entangled Polymers. *Macromolecules* **1998**, *31*, 7895–7914.

[38] Graham, R. S.; Likhtman, A. E.; McLeish, T. C. B.; Milner, S. T. Microscopic theory of linear, entangled polymer chains under rapid deformation including chain stretch and convective constraint release. *Journal of Rheology* **2003**, *47*, 1171.

[39] Likhtman, A. E.; Graham, R. S. Simple constitutive equation for linear polymer melts derived from molecular theory: Rolie-Poly equation. *Journal of Non-Newtonian Fluid Mechanics* **2003**, *114*, 1–12.

[40] Cloizeaux, J. D. Double Reptation vs. Simple Reptation in Polymer Melts. *Europhysics Letters* **1988**, *5*, 437–442.

[41] Boudara, V. A. H.; Peterson, J. D.; Leal, L. G.; Read, D. J. Nonlinear rheology of polydisperse blends of entangled linear polymers: Rolie-Double-Poly models. *Journal of Rheology* **2018**, *63*, 71–91.

[42] McLeish, T. C. B.; Larson, R. G. Molecular constitutive equations for a class of branched polymers: The pom-pom polymer. *Journal of Rheology* **1998**, *42*, 81–110.

[43] Inkson, N. J.; McLeish, T. C. B.; Harlen, O. G.; Groves, D. J. Predicting low density polyethylene melt rheology in elongational and shear flows with “pom-pom” constitutive equations. *Journal of Rheology* **1999**, *43*, 873–896.

[44] Verbeeten, W. M. H.; Peters, G. W. M.; Baaijens, F. P. T. Differential constitutive equations for polymer melts: The extended PomPom model. *Journal of Rheology* **2001**, *45*, 823–843.

[45] Sato, T.; Taniguchi, T. Rheology and Entanglement Structure of Well-Entangled Polymer Melts: A Slip-Link Simulation Study. *Macromolecules* **2019**, *52*, 3951–3964.

[46] Doi, M.; Edwards, S. F. Dynamics of concentrated polymer systems. Part 2. Molecular motion under flow. *Journal of the Chemical Society, Faraday Transactions 2: Molecular and Chemical Physics* **1978**, *74*, 1802–1807.

[47] Hua, C. C.; Schieber, J. D. Segment connectivity, chain-length breathing, segmental stretch, and constraint release in reptation models. I. Theory and single-step strain predictions. *Journal of Chemical Physics* **1998**, *109*, 10018–10027.

[48] Schieber, J. D.; Neergaard, J.; Gupta, S. A full-chain, temporary network model with sliplinks, chain-length fluctuations, chain connectivity and chain stretching. *Journal of Rheology* **2003**, *47*, 213–233.

[49] Schieber, J. D. Fluctuations in entanglements of polymer liquids. *Journal of Chemical Physics* **2003**, *118*, 5162.

[50] Katzarova, M.; Kashyap, T.; Schieber, J. D.; Venerus, D. C. Linear viscoelastic behavior of bidisperse polystyrene blends : experiments and slip-link predictions. *Rheologica Acta* **2018**, *57*, 327–338.

[51] Desai, P. S.; Kang, B. G.; Katzarova, M.; Hall, R.; Huang, Q.; Lee, S.; Shivokhin, M.; Chang, T.; Venerus, D. C.; Mays, J.; Schieber, J. D.; Larson, R. G. Challenging Tube and Slip-Link Models: Predicting the Linear Rheology of Blends of Well-Characterized Star and Linear 1,4-Polybutadienes. *Macromolecules* **2016**, *49*, 4964–4977.

[52] Andreev, M.; Khaliullin, R. N.; Steenbakkers, R. J. A.; Schieber, J. D. Approximations of the discrete slip-link model and their effect on nonlinear rheology predictions. *Journal of Rheology* **2013**, *57*, 535–557.

[53] Bach, A.; Almdal, K.; Rasmussen, H. K.; Hassager, O. Elongational Viscosity of Narrow Molar Mass Distribution Polystyrene Elongational Viscosity of Narrow Molar Mass Distribution Polystyrene. *Macromolecules* **2003**, *36*, 5174–5179.

[54] Schieber, J. D. GENERIC compliance of a temporary network model with sliplinks, chain-length fluctuations, segment-connectivity and constraint release. *Journal of Non-Equilibrium Thermodynamics* **2003**, *28*, 179–188.

[55] Grmela, M.; Öttinger, H. Dynamics and thermodynamics of complex fluids. I. Development of a general formalism. *Physical Review E* **1997**, *56*, 6620–6632.

[56] Öttinger, H. C.; Grmela, M. Dynamics and thermodynamics of complex fluids. II. Illustrations of a general formalism. *Physical Review E* **1997**, *56*, 6633–6655.

[57] Andreev, M.; Feng, H.; Yang, L.; Schieber, J. D. Universality and speedup in equilibrium and nonlinear rheology predictions of the fixed slip-link model. *Journal of Rheology* **2014**, *58*, 723–736.

[58] Masubuchi, Y.; Takimoto, J. I.; Koyama, K.; Ianniruberto, G.; Marrucci, G.; Greco, F. Brownian simulations of a network of reptating primitive chains. *Journal of Chemical Physics* **2001**, *115*, 4387–4394.

[59] Masubuchi, Y.; Ianniruberto, G.; Greco, F.; Marrucci, G. Quantitative comparison of primitive chain network simulations with literature data of linear viscoelasticity for polymer melts. *Journal Non-Newtonian Fluid Mechanics* **2008**, *149*, 87–92.

[60] Masubuchi, Y.; Watanabe, H.; Ianniruberto, G.; Greco, F.; Marrucci, G. Comparison among slip-link simulations of bidisperse linear polymer melts. *Macromolecules* **2008**, *41*, 8275–8280.

[61] Masubuchi, Y.; Ianniruberto, G.; Greco, F.; Marrucci, G. Primitive chain network simulations for branched polymers. *Rheologica Acta* **2006**, *46*, 297–303.

[62] Masubuchi, Y.; Matsumiya, Y.; Watanabe, H.; Marrucci, G.; Ianniruberto, G. Primitive chain network simulations for Pom-Pom polymers in uniaxial elongational flows. *Macromolecules* **2014**, *47*, 3511–3519.

[63] Yaoita, T.; Isaki, T.; Masubuchi, Y.; Watanabe, H.; Ianniruberto, G.; Marrucci, G. Primitive chain network simulation of elongational flows of entangled linear chains: Role of finite chain extensibility. *Macromolecules* **2011**, *44*, 9675–9682.

[64] Yaoita, T.; Isaki, T.; Masubuchi, Y.; Watanabe, H.; Ianniruberto, G.; Marrucci, G. Primitive chain network simulation of elongational flows of entangled linear chains: Stretch/orientation-induced reduction of monomeric friction. *Macromolecules* **2012**, *45*, 2773–2782.

[65] Uneyama, T.; Masubuchi, Y. Detailed balance condition and effective free energy in the primitive chain network model. *Journal of Chemical Physics* **2011**, *135*, 184904.

[66] Masubuchi, Y.; Uneyama, T.; Watanabe, H.; Ianniruberto, G.; Greco, F.; Marrucci, G. Structure of entangled polymer network from primitive chain network simulations. *Journal of Chemical Physics* **2010**, *132*, 134902.

[67] Doi, M.; Takimoto, J. Molecular modelling of entanglement. *Philosophical Transactions. Series A, Mathematical, Physical, and Engineering sciences* **2003**, *361*, 641–652.

[68] Shanbhag, S.; Larson, R. G.; Takimoto, J.; Doi, M. Deviations from dynamic dilution in the terminal relaxation of star polymers. *Physical Review Letters* **2001**, *87*, 195502.

[69] Shanbhag, S.; Larson, R. G. A Slip-Link Model of Branch-Point Motion in Entangled Polymers. *Macromolecules* **2004**, *37*, 8160–8166.

[70] Shanbhag, S. Fast Slip Link Model for Bidisperse Linear Polymer Melts. *Macromolecules* **2019**, *52*, 3092–3103.

[71] Likhtman, A. E. Single-chain slip-link model of entangled polymers: Simultaneous description of neutron spin-echo, rheology, and diffusion. *Macromolecules* **2005**, *38*, 6128–6139.

[72] Ramírez, J.; Sukumaran, S. K.; Likhtman, A. E. Significance of cross correlations in the stress relaxation of polymer melts. *Journal of Chemical Physics* **2007**, *126*, 244904.

[73] Uneyama, T. Single Chain Slip-Spring Model for Fast Rheology Simulations of Entangled Polymers on GPU. *Nihon Reoroji Gakkaishi* **2011**, *39*, 135–152.

[74] Del Biondo, D.; Masnada, E. M.; Merabia, S.; Couty, M.; Barrat, J. L. Numerical study of a slip-link model for polymer melts and nanocomposites. *Journal of Chemical Physics* **2013**, *138*, 194902.

[75] Uneyama, T.; Masubuchi, Y. Multi-chain slip-spring model for entangled polymer dynamics. *Journal of Chemical Physics* **2012**, *137*, 154902.

[76] Masubuchi, Y. Effects of degree of freedom below entanglement segment on relaxation of polymer configuration under fast shear in multi-chain slip-spring simulations. *Journal of Chemical Physics* **2015**, *143*, 224905.

[77] Masubuchi, Y. Multichain Slip-Spring Simulations for Branch Polymers. *Macromolecules* **2018**, *51*, 10184–10193.

[78] Masubuchi, Y.; Uneyama, T. Comparison among multi-chain models for entangled polymer dynamics. *Soft Matter* **2018**, *14*, 5986–5994.

[79] Vogiatzis, G. G.; Megariotis, G.; Theodorou, D. N. Equation of State Based Slip Spring Model for Entangled Polymer Dynamics. *Macromolecules* **2017**, *50*, 3004–3029.

[80] Sgouros, A. P.; Megariotis, G.; Theodorou, D. N. Slip-Spring Model for the Linear and Nonlinear Viscoelastic Properties of Molten Polyethylene Derived from Atomistic Simulations. *Macromolecules* **2017**, *50*, 4524–4541.

[81] Moghadam, S.; Saha Dalal, I.; Larson, R. G. Unraveling Dynamics of Entangled Polymers in Strong Extensional Flows. *Macromolecules* **2019**, *52*, 1296–1307.

[82] Moghadam, S.; Dalal, I. S.; Larson, R. G. Slip-spring and kink dynamics models for fast extensional flow of entangled polymeric fluids. *Polymers* **2019**, *11*, 465.

[83] Bird, R. B.; Armstrong, R. C.; Hassager, O. *Dynamics of Polymeric Liquids Volume 1 Fluid Mechanics*; John Wiley and Sons, Inc., 1987.

[84] Kaye, A. *Non-Newtonian Flow in Incompressible Fluids, Note No. 134.*; The College of Aeronautics Cranfield, 1962.

[85] Bernstein, B.; Kearsley, E. A.; Zapas, L. J. A study of stress relaxation with finite strain. *Transactions of the Society of Rheology* **1963**, *7*, 391–410.

[86] Larson, R. G. A Constitutive Equation for Polymer Melts Based on Partially Extending Strand Convection. *Journal of Rheology* **1984**, *28*, 545–571.

[87] Giesekus, H. A simple constitutive equation for polymer fluids based on the concept of deformation-dependent tensorial mobility. *Journal of Non-Newtonian Fluid Mechanics* **1982**, *11*, 69–109.

[88] Leonov, A. I. Nonequilibrium thermodynamics and rheology of viscoelastic polymer media. *Rheologica Acta* **1976**, *15*, 85–98.

[89] Green, M. S.; Tobolsky, A. V. A New Approach to the Theory of Relaxing Polymeric Media. *Journal of Chemical Physics* **1946**, *14*, 80–92.

[90] Thien, N. P.; Tanner, R. I. A new constitutive equation derived from network theory. *Journal of Non-Newtonian Fluid Mechanics* **1977**, *2*, 353–365.

[91] Kase, S.; Matsuo, T. Studies on melt spinning. I. Fundamental equations on the dynamics of melt spinning. *Journal of Polymer Science Part A: General Papers* **1965**, *3*, 2541–2554.

[92] Kase, S.; Matsuo, T. Transient Solutions of Fundamental Equations Compared with Experimental Results. *Journal of Applied Polymer Science* **1967**, *287*, 251–287.

[93] Fisher, R.; Denn, M. Mechanics of nonisothrmal polymer melt spinning. *AIChE Journal* **1977**, *23*, 23–28.

[94] Gagon, D. K.; Denn, M. M. Computer simulation of steady polymer melt spinning. *Polymer Engineering and Science* **1981**, *21*, 844–853.

[95] Doufas, A. K.; McHugh, A. J.; Miller, C. Simulation of melt spinning including flow-induced crystallization: Part I. Model development and predictions. *Journal of Non-Newtonian Fluid Mechanics* **2000**, *92*, 27–66.

[96] Joo, Y.; Sun, J.; Smith M.D. Two-dimensional numerical analysis of non-isothermal melt spinning with and without phase transition. *Journal of Non-Newtonian Fluid Mechanics* **2002**, *102*, 37–70.

[97] van Meerveld, J.; Hütter, M.; Peters, G. W. M. Continuum model for the simulation of fiber spinning, with quiescent and flow-induced crystallization. *Journal of Non-Newtonian Fluid Mechanics* **2008**, *150*, 177–195.

[98] Dietz, W. Polyester fiber spinning analyzed with multimode Phan Thien-Tanner model. *Journal of Non-Newtonian Fluid Mechanics* **2015**, *217*, 37–48.

[99] Tadmor, Z.; Gogos, C. G. *Principles of Polymer Processing*; Wiley, New York, 2006.

[100] Nakayama, Y.; Kajiwara, T.; Masaki, T. Strain mode of general flow: Characterization and implications for flow pattern structures. *AIChE Journal* **2016**, *62*, 2563–2569.

[101] Nakayama, Y.; Takemitsu, H.; Kajiwara, T.; Kimura, K.; Takeuchi, T.; Tomiyama, H. Improving mixing characteristics with a pitched tip in kneading elements in twin-screw extrusion. *AIChE Journal* **2018**, *64*, 1424–1434.

[102] Xue, S. C.; Phan-Thien, N.; Tanner, R. I. Three dimensional numerical simulations of viscoelastic flows through planar contractions. *Journal of Non-Newtonian Fluid Mechanics* **1998**, *74*, 195–245.

[103] Verbeeten, W. M. H.; Peters, G. W. M.; Baaijens, F. P. T. Numerical simulations of the planar contraction flow for a polyethylene melt using the XPP model. *Journal of Non-Newtonian Fluid Mechanics* **2004**, *117*, 73–84.

[104] Collis, M. W.; Mackley, M. R. The melt processing of monodisperse and polydisperse polystyrene melts within a slit entry and exit flow. *Journal of Non-Newtonian Fluid Mechanics* **2005**, *128*, 29–41.

[105] Hassell, D. G.; Auhl, D.; McLeish, T. C. B.; Mackley, M. R. The effect of viscoelasticity on stress fields within polyethylene melt flow for a cross-slot and contraction-expansion slit geometry. *Rheologica Acta* **2008**, *47*, 821–834.

[106] Bent, J.; Hutchings, L. R.; Richards, R. W.; Gough, T.; Spares, R.; Coates, P. D.; Grillo, I.; Harlen, O. G.; Read, D. J.; Graham, R. S.; Likhtman, A. E.; Groves, D. J.; Nicholson, T. M.; McLeish, T. C. B. Neutron-Mapping Polymer Flow: Scattering, Flow Visualization, and Molecular Theory. *Science* **2003**, *301*, 1691–1695.

[107] Collis, M. W.; Lele, A. K.; Mackley, M. R.; Graham, R. S.; Groves, D. J.; Likhtman, A. E.; Nicholson, T. M.; Harlen, O. G.; McLeish, T. C. B.; Hutchings, L. R.; Fernyhough, C. M.; Young, R. N. Constriction flows of monodisperse linear entangled polymers: Multiscale modeling and flow visualization. *Journal of Rheology* **2005**, *49*, 501.

[108] Graham, R. S.; Bent, J.; Hutchings, L. R.; Richards, R. W.; Groves, D. J.; Embery, J.; Nicholson, T. M.; McLeish, T. C. B.; Likhtman, A. E.; Harlen, O. G.; Read, D. J.; Gough, T.; Spares, R.; Coates, P. D.; Grillo, I. Measuring and predicting the dynamics of linear monodisperse entangled polymers in rapid flow through an abrupt contraction. A small angle neutron scattering study. *Macromolecules* **2006**, *39*, 2700–2709.

[109] Hassell, D. G.; MacKley, M. R.; Sahin, M.; Wilson, H. J.; Harlen, O. G.; McLeish, T. C. B. Molecular physics of a polymer engineering instability: Experiments and computation. *Physical Review E* **2008**, *77*, 050801(R).

[110] Clarke, N.; De Luca, E.; Buxton, G.; Hutchings, L. R.; Gough, T.; Grillo, I.; Graham, R. S.; Jagannathan, K.; Klein, D. H.; McLeish, T. C. B. Chain Deformation in Entangled Polymer Melts at Re-entrant Corners. *Macromolecules* **2010**, *43*, 1539–1542.

[111] Ren, J.; Ouyang, J.; Jiang, T.; Li, Q. Simulation of complex filling process based on the generalized Newtonian fluid model using a corrected SPH scheme. *Computational Mechanics* **2012**, *49*, 643–665.

[112] Ren, J.; Ouyang, J.; Jiang, T. An improved particle method for simulation of the non-isothermal viscoelastic fluid mold filling process. *International Journal of Heat and Mass Transfer* **2015**, *85*, 543–560.

[113] Sato, T.; Harada, K.; Taniguchi, T. Multiscale Simulations of Flows of a Well-Entangled Polymer Melt in a Contraction-Expansion Channel. *Macromolecules* **2019**, *52*, 547–567.

[114] Laso, M.; Öttinger, H. Calculation of viscoelastic flow using molecular models: the connffessit approach. *Journal of Non-Newtonian Fluid Mechanics* **1993**, *47*, 1–20.

[115] Feigl, K.; Laso, M.; Öttinger, H. C. CONNFFESSIT Approach for Solving a Two-Dimensional Viscoelastic Fluid Problem. *Macromolecules* **1995**, *28*, 3261–3274.

[116] Hua, C. C.; Schieber, J. D. Application of kinetic theory models in spatiotemporal flows for polymer solutions, liquid crystals and polymer melts using the connffessit approach. *Chemical Engineering Science* **1996**, *51*, 1473–1485.

[117] Laso, M.; Picasso, M.; Öttinger, H. 2-D Time-Dependent Viscoelastic Flow Calculations Using CONNFFESSIT. *AIChE Journal* **1997**, *43*, 877–892.

[118] Grande, E.; Laso, M.; Picasso, M. Calculation of variable-topology free surface flows using CONNFFESSIT. *Journal of Non-Newtonian Fluid Mechanics* **2003**, *113*, 127–145.

[119] E, W.; Engquist, B. The Heterognous Multiscale Methods. *Communications in Mathematical Sciences* **2003**, *1*, 87–132.

[120] Ren, W.; E, W. Heterogeneous multiscale method for the modeling of complex fluids and micro-fluidics. *Journal of Computational Physics* **2005**, *204*, 1–26.

[121] De, S.; Fish, J.; Shephard, M. S.; Keblinski, P.; Kumar, S. K. Multiscale modeling of polymer rheology. *Physical Review E* **2006**, *74*, 030801(R).

[122] De, S. Computational study of the propagation of the longitudinal velocity in a polymer melt contained within a cylinder using a scale-bridging method. *Physical Review E* **2013**, *88*, 052311.

[123] Yasuda, S.; Yamamoto, R. A model for hybrid simulations of molecular dynamics and computational fluid dynamics. *Physics of Fluids* **2008**, *20*, 113101.

[124] Yasuda, S.; Yamamoto, R. Rheological properties of polymer melt between rapidly oscillating plates: An application of multiscale modeling. *Europhysics Letters* **2009**, *86*, 18002.

[125] Yasuda, S.; Yamamoto, R. Multiscale modeling and simulation for polymer melt flows between parallel plates. *Physical Review E* **2010**, *81*, 036308.

[126] Yasuda, S.; Yamamoto, R. Dynamic rheology of a supercooled polymer melt in nonuniform oscillating flows between rapidly oscillating plates. *Physical Review E* **2011**, *84*, 031501.

[127] Yasuda, S.; Yamamoto, R. Synchronized molecular-dynamics simulation via macroscopic heat and momentum transfer: An application to polymer lubrication. *Physical Review X* **2014**, *4*, 041011.

[128] Yasuda, S.; Yamamoto, R. Synchronized molecular-dynamics simulation for the thermal lubrication of a polymeric liquid between parallel plates. *Computers & Fluids* **2016**, *124*, 185–189.

[129] Yasuda, S. Synchronized Molecular-Dynamics Simulation of the Thermal Lubrication of an Entangled Polymeric Liquid. *Polymers* **2019**, *11*, 131.

[130] Hulsen, M. A.; van Heel, A. P. G.; van den Brule, B. Simulation of viscoelastic flows using Brownian configuration fields. *Journal of Non-Newtonian Fluid Mechanics* **1997**, *70*, 79–101.

[131] Lu, Z.; Khoo, B. C.; Dou, H. S.; Phan-Thien, N.; Seng Yeo, K. Numerical simulation of fibre suspension flow through an axisymmetric contraction and expansion passages by Brownian configuration field method. *Chemical Engineering Science* **2006**, *61*, 4998–5009.

[132] Bajaj, M.; Bhat, P. P.; Ravi Prakash, J.; Pasquali, M. Multiscale simulation of viscoelastic free surface flows. *Journal of Non-Newtonian Fluid Mechanics* **2006**, *140*, 87–107.

[133] Griebel, M.; Rüttgers, A. Multiscale simulations of three-dimensional viscoelastic flows in a square-square contraction. *Journal of Non-Newtonian Fluid Mechanics* **2014**, *205*, 41–63.

[134] Xu, X. H.; Guo, X. W.; Cao, Y.; Ren, X. G.; Chen, J.; Yang, X. J. Multi-scale simulation of non-equilibrium phase transitions under shear flow in dilute polymer solutions. *RSC Advances* **2015**, *5*, 54649–54657.

[135] Halin, P.; Lielens, G.; Keunings, R.; Legat, V. The Lagrangian particle method for macroscopic and micro-macro viscoelastic flow computations. *Journal of Non-Newtonian Fluid Mechanics* **1998**, *79*, 387–403.

[136] Wapperom, P.; Keunings, R.; Legat, V. The backward-tracking Lagrangian particle method for transient viscoelastic flows. *Journal of Non-Newtonian Fluid Mechanics* **2000**, *91*, 273–295.

[137] Murashima, T.; Taniguchi, T. Multiscale Simulation of History Dependent Flow in Polymer Melt. *Europhysics Letters* **2011**, *96*, 18002.

[138] van Heel, A. P. G.; Hulsen, M. A.; van den Brule, B. H. A. A. Simulation of the DoiEdwards model in complex flow. *Journal of Rheology* **1999**, *43*, 1239–1260.

[139] Peters, E. A. J. F.; van Heel, A. P. G.; Hulsen, M. A.; van den Brule, B. H. A. A. Generalization of the deformation field method to simulate advanced reptation models in complex flow. *Journal of Rheology* **2000**, *44*, 811–829.

[140] Masubuchi, Y.; Uneyama, T.; Saito, K. A multiscale simulation of polymer processing using parameter-based bridging in melt rheology. *Journal of Applied Polymer Science* **2012**, *125*, 2740–2747.

[141] Monaghan, J. Smoothed Particle Hydrodynamics and Its Diverse Applications. *Annual Review of Fluid Mechanics* **2012**, *44*, 323–346.

[142] Murashima, T.; Taniguchi, T. Multiscale Lagrangian fluid dynamics simulation for polymeric fluid. *Journal of Polymer Science, Part B: Polymer Physics* **2010**, *48*, 886–893.

[143] Murashima, T.; Taniguchi, T. Flow-history-dependent behavior of entangled polymer melt flow analyzed by multiscale simulation. *Journal of the Physical Society of Japan* **2012**, *81*, SA013.

[144] Murashima, T.; Yasuda, S.; Taniguchi, T.; Yamamoto, R. Multiscale modeling for polymeric flow: Particle-fluid bridging scale methods. *Journal of the Physical Society of Japan* **2013**, *82*, 1–15.

[145] Sato, T.; Takase, K.; Taniguchi, T. Multiscale simulation of polymer melt spinning by using the dumbbell model. *Nihon Reoroji Gakkaishi* **2016**, *44*, 265–280.

[146] Sato, T.; Taniguchi, T. Multiscale simulations for entangled polymer melt spinning process. *Journal of Non-Newtonian Fluid Mechanics* **2017**, *241*, 34–42.

[147] Feng, H.; Andreev, M.; Pilyugina, E.; Schieber, J. D. Smoothed particle hydrodynamics simulation of viscoelastic flows with the slip-link model. *Molecular Systems Design and Engineering* **2016**, *1*, 99–108.

[148] Ianniruberto, G.; Brasiello, A.; Marrucci, G. FRICTION COEFFICIENT DOES NOT STAY CONSTANT IN NONLINEAR VISCOELASTICITY. *Proc. 7th Annu. Eur. Rheol. Conf.* **2011**, *61.*

[149] Desai, P. S.; Larson, R. G. Constitutive model that shows extension thickening for entangled solutions and extension thinning for melts. *Journal of Rheology* **2014**, *58*, 255–279.

[150] Yaoita, T.; Masubuchi, Y.; Watanabe, H. Concept of Stretch/Orientation-Induced Friction Reduction Tested with a Simple Molecular Constitutive Equation. *Nihon Reoroji Gakkaishi* **2014**, *42*, 207–213.

[151] Masubuchi, Y.; Matsumiya, Y.; Watanabe, H. Test of orientation/stretch-induced reduction of friction via primitive chain network simulations for polystyrene, polyisoprene, and poly(n -butyl acrylate). *Macromolecules* **2014**, *47*, 6768–6775.

[152] Matsumiya, Y.; Watanabe, H.; Masubuchi, Y.; Huang, Q.; Hassager, O. Nonlinear Elongational Rheology of Unentangled Polystyrene and Poly(p-tert-butylstyrene) Melts. *Macromolecules* **2018**, *51*, 9710–9729.

[153] Masubuchi, Y.; Pandey, A.; Amamoto, Y. Inter-Chain Cross-Correlation in Multi-Chain Slip-Link Simulations without Force Balance at Entanglements. *Nihon Reoroji Gakkaishi* **2017**, *45*, 175–180.

[154] Nielsen, J. K.; Rasmussen, H. K.; Hassager, O. Stress relaxation of narrow molar mass distribution polystyrene following uniaxial extension. *Journal of Rheology* **2008**, *52*, 885.

[155] Nielsen, J. K.; Rasmussen, H. K.; Hassager, O.; McKinley, G. H. Elongational viscosity of monodisperse and bidisperse polystyrene melts. *Journal of Rheology* **2006**, *50*, 453.

[156] Schweizer, T.; van Meerveld, J.; Öttinger, H. C. Nonlinear shear rheology of polystyrene melt with narrow molecular weight distribution–Experiment and theory. *Journal of Rheology* **2004**, *48*, 1345.

[157] Huang, Q.; Agostini, S.; Hengeller, L.; Shivokhin, M.; Alvarez, N. J.; Hutchings, L. R.; Hassager, O. Dynamics of Star Polymers in Fast Extensional Flow and Stress Relaxation. *Macromolecules* **2016**, *49*, 6694–6699.

[158] Sridhar, T.; Acharya, M.; Nguyen, D. A.; Bhattacharjee, P. K. On the extensional rheology of polymer melts and concentrated solutions. *Macromolecules* **2014**, *47*, 379–386.

[159] Bhattacharjee, P. K.; Oberhauser, J. P.; McKinley, G. H.; Leal, L. G.; Sridhar, T. Extensional Rheometry of Entangled Solutions. *Macromolecules* **2002**, *35*, 10131–10148.

[160] Kushwaha, A.; Shaqfeh, E. S. G. Slip-link simulations of entangled polymers in planar extensional flow: Disentanglement modified extensional thinning. *Journal of Rheology* **2011**, *55*, 463–483.

[161] Ziabicki, A.; Kawai, H. *High-Speed Fiber Spinning*; John Wiley and Sons, Inc., 1985.

[162] Edberg, R.; Morriss, G. P.; Evans, D. J. Rheology of n-alkanes by nonequilibrium molecular dynamics. *Journal of Chemical Physics* **1987**, *86*, 4555–4570.

[163] Gingold, R. A.; Monaghan, J. J. Smoothed Particle Hydrodynamics: theory and application to non-spherical stars. *Monthly Notices of the Royal Astronomical Society* **1977**, *181*, 375–389.

[164] Koshizuka, S.; Oka, Y. Moving-particle semi-implicit method for fragmentation of incompressible fluid. *Nuclear Science and Engineering* **1996**, *123*, 421–434.

[165] Cleary, P. W.; Monaghan, J. J. Conduction Modelling Using Smoothed Particle Hydrodynamics. *Journal of Computational Physics* **1999**, *148*, 227–264.

[166] Morris, J. P.; Fox, P. J.; Zhu, Y. Modeling Low Reynolds Number Incompressible Flows Using SPH. *Journal of Computational Physics* **1997**, *136*, 214–226.

[167] Cummins, S. J.; Rudman, M. An SPH Projection Method. *Journal of Computational Physics* **1999**, *152*, 584–607.

[168] Xu, R.; Stansby, P.; Laurence, D. Accuracy and stability in incompressible SPH (ISPH) based on the projection method and a new approach. *Journal of Computational Physics* **2009**, *228*, 6703–6725.

[169] Lind, S. J.; Xu, R.; Stansby, P. K.; Rogers, B. D. Incompressible smoothed particle hydrodynamics for free-surface flows: A generalised diffusion-based algorithm for stability and validations for impulsive flows and propagating waves. *Journal of Computational Physics* **2012**, *231*, 1499–1523.

[170] Adami, S.; Hu, X.; Adams, N. A generalized wall boundary condition for smoothed particle hydrodynamics. *Journal of Computational Physics* **2012**, *231*, 7057–7075.

[171] Monaghan, J. J.; Kajtar, J. B. SPH particle boundary forces for arbitrary boundaries. *Computer Physics Communications* **2009**, *180*, 1811–1820.

[172] Zhang, G. M.; Batra, R. C. Modified smoothed particle hydrodynamics method and its application to transient problems. *Computational Mechanics* **2004**, *34*, 137–146.

[173] Monaghan, J. J. On the problem of penetration in particle methods. *Journal of Computational Physics* **1989**, *82*, 1–15.

[174] Takahiro, M. Multiscale Simulation Performed on ISSP Super Computer : Analysis of Entangled Polymer Melt Flow. *Activity Report 2015/Supercomputer Center, Institute for Solid State Physics, The University of Tokyo* **2016**, 35–43.

[175] Minegishi, A.; Nishioka, A.; Takahashi, T.; Masubuchi, Y.; Takimoto, J.; Koyama, K. Uniaxial elongational viscosity of PS/a small amount of UHMW-PS blends. *Rheologica Acta* **2001**, *40*, 329–338.

[176] Ianniruberto, G.; Marrucci, G. Convective orientational renewal in entangled polymers. *Journal of Non-Newtonian Fluid Mechanics* **2000**, *95*, 363–374.

[177] Ianniruberto, G.; Marrucci, G. A simple constitutive equation for entangled polymers with chain stretch A simple constitutive equation for entangled polymers with chain stretch. *Journal of Rheology* **2001**, *45*, 1305–1318.

[178] Cao, J.; Wang, Z. Microscopic Picture of Constraint Release E ff ects in Entangled Star Polymer Melts. *Macromolecules* **2016**, *49*, 5677–5691.

[179] Yamamoto, T. Computer modeling of polymer crystallization - Toward computer-assisted materials' design. *Polymer* **2009**, *50*, 1975–1985.

[180] Shaqfeh, E. S. On the rheology of particle suspensions in viscoelastic fluids. *AIChE Journal* **2019**, *65*, 1–10.

[181] Matsuoka, Y.; Nakayama, Y.; Kajiwara, T. Effects of viscoelasticity on shear-thickening in dilute suspensions in a viscoelastic fluid. *Soft Matter* **2020**, *16*, 728–737.

[182] Olmsted, P. D. Perspectives on shear banding in complex fluids. *Rheologica Acta* **2008**, *47*, 283–300.

[183] Cates, M. E.; Fielding, S. M. Rheology of giant micelles. *Advances in Physics* **2006**, *55*, 799–879.

[184] Zhao, L.; Li, Z.; Caswell, B.; Ouyang, J.; Karniadakis, G. E. Active learning of constitutive relation from mesoscopic dynamics for macroscopic modeling of non-Newtonian flows. *Journal of Computational Physics* **2018**, *363*, 116–127.

[185] Rasmussen, C. E.; Williams, C. K. I. *Gaussian Process for Machine Learning*; The MIT Press, 2005.

Acknowledgement

I would like to show my greatest gratitude to my supervisor, Associate Professor Takashi Taniguchi in Transport Phenomena laboratory at Department of Chemical Engineering in Kyoto University, for his coaching and various support as long as six years from bachelor to Ph D. Words cannot express my gratitude for his broad knowledge about research, wonderful attitude toward research, and great patience to education.

I would like to express deepest to Professor Hiroshi Watanabe and Professor Minoru Miyahara. In spite of their tight schedules, they critically reviewed the dissertation and gave me helpful comments as the dissertation committee members.

I also acknowledge Professor Ryoichi Yamamoto for enlightening advice in lab. seminars. Moreover, he showed me how exciting the academic life is. I would like to thank Assistant Professor John J. Molina for helpful comments on research. I also want to thank Dr. Norihiro Oyama, Dr. Simon K. Schnyder, and Dr. Mitsusuke Tarama for their helpful discussion and guidance. Furthermore, I am grateful to Professor Jun-ichi Takimoto and Associate Professor Sathish K. Sukumaran in Yamagata University for their helpful comments and discussions.

I am indebted to the laboratory secretary, Ms. Aiko Sotani for her various supports. A very special thanks to all the members of the transport phenomena lab. including past members for providing a wonderful and exciting environment. Thanks to them, I could enjoy my research life in this group.

I am partially supported by the Research Fellowships of the Japan Society for the Promotion of Science for Young Scientists.

I am deeply grateful to lots of my friends. With their unwavering support and encouragement, I could keep going forward. Finally, I would like to express my deepest appreciation to my family for their support, encouragement and belief. Without you, I would not be who I am today.

Takeshi Sato
Transport Phenomena Laboratory, Department of Chemical Engineering,
Graduate School of Engineering, Kyoto University

List of Publications

1. Takeshi Sato, "A Review on Transport Phenomena of Entangled Polymeric Liquids", *Journal of the Society of Rheology, Japan*, **48**, 1 (2020). [**Chapter 1** & **Chapter 5**]

   These chapters are partially reprinted from this paper with permission. Copyright (2020) The Society of Rheology, Japan.

2. Takeshi Sato and Takashi Taniguchi, "Rheology and Entanglement Structure of Well-Entangled Polymer Melts: A Slip-link Simulation Study", *Macromolecules*, **52**, 3951 (2019). [**Chapter 2**]

   This chapter is partially reprinted from this paper with permission. All figures in this paper is reused in this dissertation with permission. Copyright (2019) American Chemical Society.

3. Takeshi Sato and Takashi Taniguchi, "Multiscale simulations for entangled polymer melt spinning process", *Journal of Non-Newtonian Fluid Mechanics*, **241**, 34 (2017). [**Chapter 3**]

   This chapter is partially adapted from this paper.

4. Takeshi Sato, Kazuhiro Takase and Takashi Taniguchi, "Multiscale simulation of polymer melt spinning by using the dumbbell model", *Journal of the Society of Rheology, Japan*, **44**, 265 (2016).

5. Takeshi Sato, Kohei Harada and Takashi Taniguchi, "Multiscale Simulations for Flows of a Well-Entangled Polymer Melt in a Contraction-Expansion Channel", *Macromolecules*, **52**, 547 (2019). [**Chapter 4**]

   This chapter is partially reprinted from this paper with permission. All figures in this paper is reused in this dissertation with permission. Copyright (2019) American Chemical Society.